

**EFFECTS OF ION BOMBARDMENT AND VUV
IRRADIATION ON NAFION[®] POLYMER
ELECTROLYTE MEMBRANE**

Yuttakarn Rattanachai

**A Thesis Submitted in Partial Fulfillment of the Requirements for the
Degree of Doctor of Philosophy in Physics
Suranaree University of Technology
Academic Year 2011**

ผลของการระดมยิงด้วยไอออนและการฉายรังสีวิทยุวีตอเยื่อพอลิเมอร์
อิเล็กทรอนิกส์แนฟฟิออน

นายยุทธการ รัตนชัย

วิทยานิพนธ์นี้เป็นส่วนหนึ่งของการศึกษาตามหลักสูตรปริญญาวิทยาศาสตรดุษฎีบัณฑิต
สาขาวิชาฟิสิกส์
มหาวิทยาลัยเทคโนโลยีสุรนารี
ปีการศึกษา 2554

**EFFECTS OF ION BOMBARDMENT AND VUV IRRADIATION
ON NAFION[®] POLYMER ELECTROLYTE MEMBRANE**

Suranaree University of Technology has approved this thesis submitted in partial fulfillment of the requirements for the Degree of Doctor of Philosophy.

Thesis Examining Committee

(Asst. Prof. Dr. Chinorat Kobdaj)

Chairperson

(Assoc. Prof. Dr. Prayoon Songsiriritthigul)

Member (Thesis Advisor)

(Dr. Min Medhisuwakul)

Member

(Asst. Prof. Dr. Supagorn Rugmai)

Member

(Dr. Yingyot Pooarporn)

Member

(Dr. Worawat Meevasana)

Member

(Prof. Dr. Sukit Limpijumnong)

Vice Rector for Academic Affairs

(Assoc. Prof. Dr. Prapun Manyum)

Dean of Institute of Science

ยุทธการ รัตนชัย : ผลของการระดมยิงด้วยไอออนและการฉายรังสีวีวียูวีต่อเยื่อพอลิเมอร์
อิเล็กโทรไลต์แนฟฟิออน (EFFECTS OF ION BOMBARDMENT AND VUV
IRRADIATION ON NAFION® POLYMER ELECTROLYTE MEMBRANE).
อาจารย์ที่ปรึกษา : รองศาสตราจารย์ ดร.ประยูร ส่งสิริฤทธิกุล, 175 หน้า.

วิทยานิพนธ์นี้มุ่งศึกษาเยื่อแนฟฟิออน (Nafion® membrane) ซึ่งเป็นเยื่อพอลิเมอร์
อิเล็กโทรไลต์ที่ใช้เป็นส่วนประกอบหลักของเซลล์เชื้อเพลิงแบบส่งผ่านโปรตรอน (PEMFC) โดย
ผิวของเยื่อแนฟฟิออนจะได้รับการปรับปรุงด้วยการฉายแสงซินโครตรอนอัลตราไวโอเลต
สุญญากาศ (VUV) ภายในห้องสุญญากาศระดับสูง โดยทั่วไปสมรรถนะของเซลล์เชื้อเพลิงจากเยื่อ
แนฟฟิออนที่ผ่านกระบวนการการเสื่อมสภาพเชิงแสง (Photo-degradation mechanism) จะ
ลดลงทั้งในแง่ของความทนทานและในแง่ของการนำโปรตรอนของเซลล์เชื้อเพลิงจนส่งผลให้ไม่
สามารถใช้งานเยื่อที่เสื่อมสภาพนี้ได้อีกต่อไป ในการปรับปรุงผิวด้วยฉายแสงอัลตราไวโอเลต
สุญญากาศนี้เยื่อที่เสื่อมสภาพจะถูกฉายด้วยพลังงานหนึ่งร้อยอิเล็กตรอนโวลต์ และใช้ปริมาณฟลู-
เอนซ์ (Fluence) ของรังสีซึ่งครอบคลุมค่าแรกเริ่มที่ได้มาจากแบบจำลองทางคณิตศาสตร์ของการ
กระเจิงรังสีเอกซ์และการกระเจิงนิวตรอนมุมแคบ (SAXS/SANS) จากนั้นเยื่อที่ได้รับการฉายรังสี
จะถูกประกอบเป็นชุดเมมเบรนอิเล็กโทรดแอสเซมบลี (MEA) ด้วยวิธีการอัดด้วยความร้อน เพื่อ
เข้าสู่การทดสอบสมรรถนะเซลล์เชื้อเพลิงเดี่ยว ซึ่งสมรรถนะของเซลล์เชื้อเพลิงนี้สามารถอธิบายได้
ด้วยแผนภูมิความสัมพันธ์ระหว่างค่าความหนาแน่นของกระแสไฟฟ้าและความต่างศักย์ระหว่างขั้ว
ของเซลล์เชื้อเพลิง ซึ่งงานวิจัยนี้ได้พบว่าสมรรถนะเซลล์เชื้อเพลิงจะเพิ่มมากขึ้นตามปริมาณฟลู-
เอนซ์ของรังสี ซึ่งบ่งชี้ได้ว่าเยื่อแนฟฟิออนได้รับการเพิ่มสมรรถนะภายหลังจากการฉายรังสี อนึ่ง
งานวิจัยยังได้ใช้การทดลองเพื่อเปรียบเทียบการเปลี่ยนแปลงโครงสร้างทางเคมีบริเวณผิวของเยื่อ
แนฟฟิออนด้วยวิธีการระดมยิงด้วยไอออนของอาร์กอน (Ar^+ sputtering) การฉายแสงซินโคร-
ตรอนหลายรังสี (Polychromatic synchrotron irradiations) เพื่อเปรียบเทียบกับการฉายด้วย
แสงซินโครตรอนอัลตราไวโอเลตเอกรงค์ (Monochromatic VUV synchrotron irradiations)
ภายใต้สภาพสุญญากาศ โดยการเปรียบเทียบนี้ได้ใช้วิธีแมสสเปกโตรเมตรี การกระเจิงรังสีเอ็กซ์มุม
น้อย และโฟโตมิชชันสเปกโทรสโกปี (PES) เป็นเครื่องมือวัด ซึ่งการปรับปรุงพื้นผิวภายหลังจาก
การฉายแสงจะถูกตรวจสอบ และพบว่ากระบวนการฉายรังสีจะทำให้เกิดการแยกออกของอะตอมของ
ธาตุฟลูออรีน ซึ่งเป็นองค์ประกอบหลักของเยื่อแนฟฟิออน และพบการหลุดออกของอะตอมธาตุ
ประกอบออกซิเจนซึ่งเป็นสิ่งเจือปนอันเนื่องมาจากกระบวนการการเสื่อมสภาพเชิงแสง ณ บริเวณ
พื้นผิวของเยื่อแนฟฟิออน อีกทั้งยังตรวจพบการเพิ่มความเปราะบางของผิวของเยื่อแนฟฟิออนภาย

หลังจากที่ได้รับการฉายแสง ผลลัพธ์จากการตรวจวัดที่ได้นั้นสอดคล้องเป็นอย่างดีกับผลลัพธ์จากการใช้การคำนวณเชิงคอมพิวเตอร์ด้วยทฤษฎีความหนาแน่นฟังก์ชัน (DFT) ซึ่งล้วนมีความสอดคล้องกับการเพิ่มสมรรถนะของเซลล์เชื้อเพลิง เทคนิคการฟื้นฟูพื้นผิวในงานวิจัยนี้สามารถนำไปประยุกต์ใช้ในการทำความสะอาดพื้นผิวของแนฟฟิออนเสื่อมสภาพ ที่ซึ่งการทำความสะอาดโดยทั่วไปด้วยสารเคมีเพียงวิธีเดียวนั้นอาจไม่เพียงพอ



สาขาวิชาฟิสิกส์
ปีการศึกษา 2554

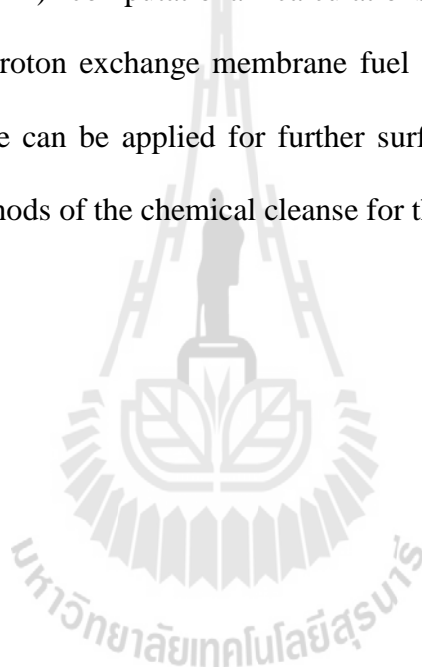
ลายมือชื่อนักศึกษา _____
ลายมือชื่ออาจารย์ที่ปรึกษา _____
ลายมือชื่ออาจารย์ที่ปรึกษาร่วม _____

YUTTAKARN RATTANACHAI : EFFECTS OF ION BOMBARDMENT
AND VUV IRRADIATION ON NAFION[®] POLYMER ELECTROLYTE
MEMBRANE. THESIS ADVISOR : ASSOC. PROF. PRAYOON
SONGSIRIRITTHIGUL, Ph.D. 175 PP.

NAFION[®]/PROTON EXCHANGE MEMBRANE FUEL CELL/SYNCHROTRON/
VACUUM ULTRAVIOLET RADIATION

Nafion[®], a polymer electrolyte membrane for proton exchange membrane fuel cells (PEMFCs), is modified by using vacuum ultraviolet (VUV) synchrotron radiation in an ultrahigh vacuum (UHV) chamber. From the photo-degradation of Nafion which is generated in different weather conditions, the performance of the PEMFC using the degraded Nafion exhibits worthless in either fuel cell durability or proton conductivity. In the VUV irradiations, the degraded membranes are exposed to the monochromatic photon beam of 100 eV from synchrotron radiation with various photon fluences covering the threshold fluence. The threshold fluence is determined by the mathematical model based on small angle X-ray and neutron scattering (SAXS/SANS). The irradiated membranes are then constructed technically by using hot-pressing processes subject to membrane electrode assembly (MEA) to measure the fuel cell performance in terms of current-voltage measurements. The relatively improvement of the fuel cell performance with the different VUV fluences indicates the modifications of the degraded membranes after irradiations. Moreover, several characterization techniques are applied to verify the structural evolution of Nafion upon the VUV irradiations, in comparison with the Ar⁺ sputtering and the

polychromatic synchrotron irradiations, such as mass spectrometry, small angle X-ray scattering and photoemission spectroscopy (PES). The surface modifications upon the VUV irradiations are identified. The major modifications are the removal of the fluorine and/or oxygen-containing functionalities from the photo-degradation mechanism, such as C-O, C=O or COOH, and the development of the surface metallicity of Nafion. Our characterization results agree very well with the density functional theory (DFT) computational calculations and directly relate to the improvement of the proton exchange membrane fuel cell performance. Our surface modification technique can be applied for further surface cleaning methods beyond ordinary cleaning methods of the chemical cleanse for the degraded Nafion.



School of Physics

Academic Year 2011

Student's Signature _____

Advisor's Signature _____

Co-advisor's Signature _____

ACKNOWLEDGEMENTS

There are many people, to whom I would like to express my sincere words of acknowledgments:

I thank Assoc. Prof. Dr. Prayoon Songsiriritthigul, my thesis advisor, for introducing me to the field of synchrotron technology. He supervised this work in all of its stages, from the very first experiments to the final proofreading of the manuscript. Not only his scientific expertise, but also his optimism and trust were a great help and motivation throughout my work.

I thank Dr. Min. Medhisuwakul, my thesis co-advisor, for giving me the opportunity to be a user of his fuel cell research group at Thailand Center of Excellence in Physics, Department of Physics and Materials Science, Chiang Mai University and for providing me an excellent research condition. I thank him not only for the professional support but also for the good time that he offered me during my stay in Chiang Mai.

I am grateful to Asst. Prof. Dr. Supagorn Rugmai for his interest in my work and for accepting to be a member of the examination committee. I thank him for his great contribution in bringing up new questions and ideas of small angle x-ray scattering technique.

I am grateful to Dr. Worawat Meewasana, Dr. Hideki Nakajima, Dr. Yingyot Pooarporn, Dr. Anusorn Tong-on, Dr. Ritthikrai Chai-nagm and Mr. Surachet Rattanasuporn who suggested a fascinating technique of photoemission spectroscopy, vacuum ultraviolet irradiations and vacuum set-up experiments for my Ph.D. research.

I am also grateful to Asst. Prof. Dr. Theeraporn Puntheeranurak from Department of Biology, Mahidol University and Ms. Jarin Osaklung for providing the atomic force microscopy measurements.

Special thanks Mr. Pee, Mr. Jiradate Kuhakan, Mr. Achanon Chaisuwan, Mr. Thanit Saisopa and Dr. Sarun Phibanchon for their kind assistance in the computational calculations and the fuel cell performance measurements.

I am grateful to Rajamangala University of Technology Isan, Synchrotron Light Research Institute (Public Organization) and Thailand Center of Excellence in Physics for financial support.

It is impossible to list all of my fellow graduate students that were a great support during my Ph.D. study, for all the great times we had together.

Finally, this thesis is dedicated to my parents: my father, Manus Rattanachai and my mother, Amphorn Rattanachai, for their unconditional love and trust that form the solid basis of my life.

Yuttakarn Rattanachai

CONTENTS

	Page
ABSTRACT IN THAI	I
ABSTRACT IN ENGLISH.	III
ACKNOWLEDGEMENTS.....	V
CONTENTS	VII
LIST OF TABLES.....	XII
LIST OF FIGURES	XIV
LIST OF ABBEVIATIONS	XXII
CHAPTER	
I INTRODUCTION	1
1.1 Introduction of Energy Sources	1
1.2 Introduction to Fuel Cell Technology.....	7
1.2.1 Polymer electrolyte membrane fuel cells.....	9
1.2.2 Fuel cell applications	10
1.3 Scope and Limitations of the Study.....	11
II PROTON EXCHANGE MEMBRANE FUEL CELL	13
2.1 Basic Principle of PEMFCs.....	13
2.2 Fuel Cell Components	15
2.2.1 Electrode	16
2.2.2 Membrane	17

CONTENTS (continued)

	Page
2.3 Fuel Cell Thermodynamics.....	19
2.3.1 Heat of reaction.....	19
2.3.3 Theoretical electrical work	20
2.3.4 Theoretical fuel cell potential	21
2.4 Fuel Cell Electrochemistry	22
2.4.1 Reaction rate	23
2.4.2 Reaction constants and transfer coefficient	24
2.4.3 Current potential relationship—Butler-Volmer equation	25
2.4.4 Voltage losses	27
2.4.4.1 Activation polarization	28
2.4.4.2 Internal currents and crossover losses	30
2.4.4.3 Ohmic (resistive) losses.....	31
2.4.4.4 Concentration polarization.....	31
2.4.5 Cell potential-polarization curve.....	33
2.4.6 Fuel cell efficiency.....	35
III NAFION[®] MEMBRANE: PROPERTIES AND APPLICATIONS.....	36
3.1 Introduction.....	36
3.2 Applications of Fluoropolymer Materials	38
3.3 Early Developments of Nafion	40
3.4 Nafion Morphology	42

CONTENTS (continued)

	Page
3.5 Degradation Mechanism of Nafion	45
IV RESEARCH METHODOLOGY	50
4.1 Sample Preparations	51
4.2 VUV Irradiations	52
4.3 Photoemission Spectroscopy	53
4.4 Computational Calculations.....	59
4.4.1 Density functional theory.....	60
4.4.1.1 Derivation and formalism.....	60
4.4.1.2 Exchange-correlation functional.....	66
4.4.2 Gaussian computational programs.....	68
4.5 Mass Spectrometry	68
4.5.1 Ionization methods.....	69
4.5.2 Quadrupole mass analyzers.....	70
4.6 Small Angle X-ray Scattering.....	71
4.6.1 Theoretical basis	73
4.6.1.1 Interaction between X-ray and matter	73
4.6.1.2 Scattering vector	75
4.6.1.3 Structural determination of Nafion by SAXS.....	77
4.6.2 Experimental technique	77
4.7 Fuel Cell Performance Test	80

CONTENTS (continued)

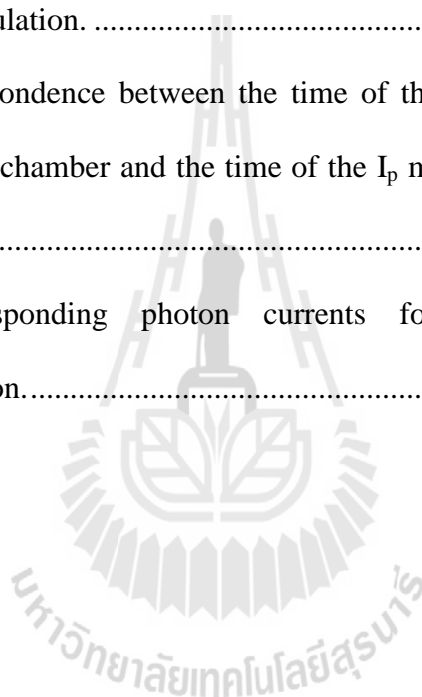
	Page
V RESULTS AND DISCUSSION	81
5.1 Structural Model of Nafion.....	82
5.1.1 Nafion structural parameters of the cylindrical water channel model.....	84
5.1.2 Threshold fluence.....	86
5.1.3 Photon fluences for the VUV irradiations	88
5.2 VUV Irradiations of the Degraded Nafion at the BL4	90
5.2.1 Slit factor	92
5.2.2 Photon flux density	93
5.2.3 Photon fluences.....	93
5.3 Other Surface Modification Techniques.....	94
5.3.1 Argon ions (Ar ⁺) sputtering	94
5.3.2 Photon bombardments	98
5.4 Small Angle X-ray Scattering.....	101
5.5 Fuel Cell Performance Test	105
5.6 Photoemission Measurements	108
5.6.1 The photon fluence calculation for the BL3.2a	109
5.6.2 Normalization of the PES intensity.....	111
5.6.3 PES spectra and binding energy adjustments	113
5.6.4 PES peak analysis	116
5.7 Theoretical Calculation of the Electronic Structure of Nafion.....	122

LIST OF TABLES

Table		Page
1.1	Classification of fuel cells	9
2.1	Enthalpies and entropies of formation for fuel cell reactants and products	21
4.1	Subareas of scattering as a function of the sample-detector distance R assuming an X-ray wavelength of $\lambda \sim 0.15$ nm.....	72
5.1	Morphological quantities of Nafion modeled by the cylindrical water channel model.....	85
5.2	Irradiation data for VUV irradiations and PES measurements.	88
5.3	The beam size for two experimental systems (PES measurement and VUV irradiation).	89
5.4	Electron currents (I_e) of the storage ring at the BL4, SLRI. The measurement of the I_e was taken during the PES measurement ($I_{e,PES}$) and during the photodiodes measurement ($I_{e, diodes}$).....	91
5.5	Relation between the electron currents and the normalized photon flux measured at $S = 10$ and $20 \mu\text{m}$. These quantities have been used for the slit factor calculations.	93
5.6	The corresponding photon fluences for the VUV irradiations at the BL4.....	94

LIST OF TABLES (Continued)

Table		Page
5.7	The improvement of the power density of the PEMFC as a function of the photon fluences (taken at the current density of 0.2 A/cm^2).....	106
5.8	The average photodiodes and gold mesh currents for number of photon calculation.	110
5.9	The correspondence between the time of the PES measurements at the ARPES chamber and the time of the I_p measurements at the XPS chamber.	112
5.10	The corresponding photon currents for the PES intensity normalization.....	113



LIST OF FIGURES

Figure		Page
1.1	World's Nuclear reactors (International Atomic Energy Agency, 2012)	3
1.2	Capital costs / megawatt in millions of dollars (Gold, 2011).....	4
1.3	Fukushima nuclear power plants explosion.	5
1.4	Worldwide energy consumption in 2010 (BP P.L.C, 2010).	5
1.5	The Air Transport Association (IATA) crude oil price reports. The price is now rising up to 110 \$ due to .the political problem and financial sanction in Iran and Libyan crisis (CAPA Center for Activation, 2011).....	6
1.6	First demonstration of a fuel cell by Grove in 1839.....	8
1.7	Summarized fuel cell applications.....	10
2.1	PEMFC components. (Ismail, Naim and Zubir, 2009).	14
2.2	Graphical representations of the reaction sites (Barbia, 2005).	17
2.3	Chemical structure of Nafion [®] (Mecadi.com, www).....	18
2.4	Fuel cell with a load: (a) load disconnected; (b) load connected.	28

LIST OF FIGURES (Continued)

Figure		Page
2.5	Voltage losses in the fuel cell.....	34
2.6	Voltage losses in fuel cell and resulting polarization curve.....	34
3.1	ETFE applications; Allianz arena stadium (a), Eden Project (b) and Water Cube (c).	39
3.2	Structural evolution of Nafion depending on water content (Yang, Sui, Peckham and Holdcroft, 2008).	43
3.3	Schematic illustration of the cluster-network model of Nafion, contributed by SAXS measurements.....	44
3.4	Free radicals formation in PTFE could either be fluorine removal (a) or chain scission (b).....	48
4.1	The degraded Nafion membrane before pretreatment (a) and the Nafion membrane after chemical pretreatment (b).	52
4.2	Schematic view of the photoemission (bottom) and inverse photoemission (top) processes (Grioni, 2006).	54
4.3	A modern PES experiment. The kinetic energy E_k of the photoelectrons can be analyzed by use of electrostatic analyzers. The whole setup is evacuated to UHV, typically $P \sim 10^{-10}$ mbar (Hüfner, 2003). 56	

LIST OF FIGURES (Continued)

Figure		Page
4.4	Energy level diagram for a metallic sample in electrical equilibrium with an electron analyzer. An analogous diagram also applies to semiconductor or insulating sample, with the only difference being that E_F lies somewhere between the filled valence bands and the empty conduction bands above (Fadley, 1978).....	58
4.5	A simple quadrupole mass spectrometer consisting of an ion source, focusing lenses, a quadrupole mass filter, and an ion detector (Montaudo and Lattimer, 2002).	69
4.6	Stability conditions, expressed in terms of U vs. V plots, for three ions with masses $m_1 < m_2 < m_3$	70
4.7	SAXS profile of a hydrated-fresh Nafion membrane extracted from the data processing program SAXSIT.....	73
4.8	Schematic diagram of X-ray scattering with an electron.	74
4.9	Scheme of the geometry for the calculation of the scattering at the detector in the direction of \vec{r}	76
4.10	Set up instrumental component of SAXS beamline for SAXS measurement of SLRI. The left hand side illustrates the sample holder. The right hand side illustrates the SAXS detector.	78
4.11	SAXS experimental setup	78

LIST OF FIGURES (Continued)

Figure		Page
4.12	Example of a polarization curve showing the losses associated with irreversibility in a fuel cell (Yamaki, 2010).....	79
5.1	Cluster-network model for the hydrated polymer presented by Gierke in 1981 and Kumar and Pineri in 1986.....	82
5.2	Parallel cylindrical water nanochannel model (Klaus et al., 2008).	83
5.3	Transverse and sagittal planes of Nafion membrane.....	85
5.4	Mass spectra of the Nafion membrane excited by the 2.0 keV of Ar ⁺ . The major fragments are CF, CF ₂ , CF ₃ and SO ₃ H.	95
5.5	Intensity (in terms of area under curve) of the Nafion molecular species (CF ₂ CF ₃ and SO ₃ H) is plotted as a function of ion energy. The percentage of elongated C-S bond in the simulation, which corresponds to the intensity of the molecular species in the sputtering measurements, is increased with increasing the energy of argon ions.....	96
5.6	AFM images of the Nafion with no sputtering (a), after 0.50 keV (b), 2.25 keV (c) and 3.00 keV Ar ⁺ sputtering (d), respectively. These pictures were taken with the field of view of 5000 nm and also converted to the 3-Dimensional of no sputtering (e) and 2.25 keV sputtering (f), respectively.....	97

LIST OF FIGURES (Continued)

Figure		Page
5.7	Mass spectra of Nafion membrane excited by 2.0 keV of Ar ⁺ sputtering, zero-order synchrotron light, 100 eV VUV radiation and without excitation.	99
5.8	SAXS images of the unirradiated membrane in the dried state (a) the VUV irradiated membrane in the dried state (b), the unirradiated membrane in the hydrated state (c), and the VUV irradiated membrane in the hydrated state (d).	102
5.9	SAXS profiles of the untreated and the treated membranes in dry and hydrated states integrated in the horizontal direction (a) and the untreated and the treated membranes in dry and hydrated states integrated in the vertical direction (b).	103
5.10	Schematic diagram of single PEMFC operation.	105
5.11	Polarization curves and the fuel cell power density of the single fuel cell using the irradiated Nafion membranes with one-side and two-side irradiations.	106
5.12	The improvement of the maximum power density of the PEMFC as a function of the photon fluences.	106
5.13	Current density at 0.6 V of the fuel cell using VUV irradiated membranes.	108

LIST OF FIGURES (Continued)

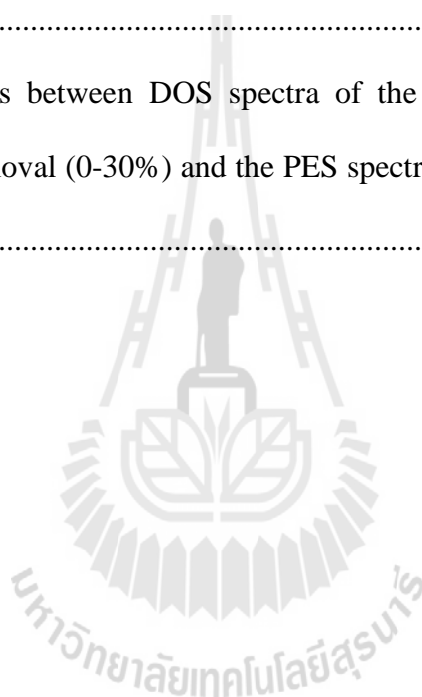
Figure		Page
5.14	Linear fit of I_p with the number of PES scans. Slope as well as vertical intercept has been used to calculate the corresponding I_p for the PES normalization.	112
5.15	PES spectra of the degraded Nafion of the different fluences of VUV irradiations, compared to the DOS result from the DFT calculations. Peak A is assigned to the F_{2s} state, peak B is the C-F band, peak C is the mixing band of the F_{2p} , C-O and C-H, peak D is the C-C band of the Nafion main chain and peak E is the conjugated C=C bond.....	115
5.16	Schematic Gaussian fit formula in OriginLab8.5.....	115
5.17	The 1 st measurement PES spectra of the degraded Nafion.	116
5.18	PES spectra of the degraded Nafion irradiated with the fluence of 2.4×10^{14} photons/cm ² . The new peak appears at the lowest occupied state (labeled "X").	117
5.19	The PES spectra of the degraded Nafion induced by VUV irradiations of 0.0, 6.2×10^{14} and 8.2×10^{15} photons/cm ² . The C=C bonds (peak X) exhibits move toward lower binding energy region with increasing the fluences.....	119

LIST OF FIGURES (Continued)

Figure	Page
5.20	Plot the PES peak positions of F_{2s} , C-F, F_{2p} and C=C bonds with the irradiation fluences. The C=C bonds moves toward lower binding energy, while other peaks move toward higher binding energy due to sample charging..... 120
5.21	Area under curves of the PES measurements of the degraded Nafion. The dramatic decrease in the fluorine peaks indicates the fluorine removal during VUV irradiations..... 121
5.22	Nafion chemical structure for $m = 5$ (left) and $m = 10$ (right) after optimization..... 123
5.23	The electron density of state (DOS) of the two different chemical structure ($m = 5$ and 10). 124
5.24	The chemical structure of Nafion ($m = 5$) provided by the DFT calculation with, (a) side-view and (b) front-view of Nafion before optimization, (c) side-view and (d) front-view of Nafion after optimization..... 125
5.25	The DOS spectra extracted from the DFT calculation of the Nafion membrane. The DOS result is similar to that result shown in Figure 5.23. 126
5.26	The DOS spectra of the Nafion membranes. The calculations are performed by removing the fluorine atoms from 0 to 40% of a single Nafion molecule. 127

LIST OF FIGURES (Continued)

Figure		Page
5.27	DOS spectra of Nafion near HOMO region and the integrated peak intensity near HOMO, which contained the C=C bands. The area under peak is linearly increased with the degree of the fluorine removal.....	127
5.28	Comparisons between DOS spectra of the different degree of the fluorine removal (0-30%) and the PES spectra of Nafion during VUV irradiations.....	128



LIST OF ABBEVIATIONS

°C	degree Celsius
A	Ampere
AFC	Alkaline fuel cells
AFM	Atomic force microscopy
AMBER	Assisted Model Building with Energy Refinement
Ar ⁺	Argon ion
ARPES	Angle resolved photoemission spectroscopy
B3LYP	Becke, Lee, Yang, and Parr hybrid functional
BL3.2a	Beamline 3.2a
BL4	Beamline 4
C=C	Carbon carbon double bond
C-C	Carbon carbon single bond
CF	Carbon-fluorine
CF ₂	Carbon difluoride
CF ₃	Carbon trifluoride
CHP	Combine heat and power
D	Photon density
DC	Direct current circuit
DFT	Density functional theory
DOS	Density of state

LIST OF ABBEVIATIONS (Continued)

E_B	Binding energy
eV	Electron volt
F	Fluence
FEP	Fluorinated ethylene propylene
GDE	Gas diffusion electrode
GDL	Gas diffusion layer
GGA	General gradient approximation
h	Plank's constant
i	Current density
I_e	Electron current
I_p	Photon current
LDA	Local density approximation
M2Cy	Cylindrical mirror
MCFC	Molten carbonate fuel cells
MEA	Membrane electrode assembly
NMR	Nuclear magnetic resonance
OCV	Open circuit voltage
PAFC	Phosphoric acid fuel cells
PEMFC	Proton exchange membrane fuel cell or polymer electrolyte membrane fuel cell
PES	Photoemission spectroscopy
PFI	Perfluorinated ionomer

LIST OF ABBEVIATIONS (Continued)

PFSA	Perfluorosulfonic acid polymer
Pt	Platinum
PTFE	Polytetrafluoroethylene PVDF
rf	Radio frequency
SANS	Small angle neutron scattering
SAXS	Small angle x-ray scattering
SLRI	Synchrotron Light Research Institute
SO ₃ H	Sulfonic acid
SOFC	Solid oxide fuel cells
UHV	Ultrahigh vacuum
UPS	Ultraviolet photoemission spectroscopy
UV	Ultraviolet
VUV	Vacuum ultraviolet
XPS	X-ray photoelectron spectroscopy
λ	Wavelength
Φ	Work function

CHAPTER I

INTRODUCTION

1.1 Introduction of Energy Sources

The world's energy consumption is rapidly growing, while the worldwide energy sources are limited. At the same time, inevitably increases in the energy demand related to per capita consumption in all nations leads to more environmental impacts, i.e., air pollution, global climate change, and emission of green house gases. In 2010, the green house gases are continuously increased not only in the developed countries but also in the developing countries. Surprisingly, the shared green house gases releasing from Thailand is ~ 1% or is the 23th most gas releasing country in the world (Rogers and Evans, 2011). Searching for alternative energy sources with an environment-friendly technology that will replace gasoline as the main product of crude oil is the most critical challenges in near future. We are entering to the new energy revolution based on the hydrogen fuel, namely "Energy Revolution". To this day, there are many available energy supplies for our demand such as wind, geothermal, water, sun, nuclear and fossil fuel. However, they have some drawback for applications due to the different in the topography and climate in each region. The wind power, for example, requests the different in the climate of each area. The steady change in the temperature is an essential requirement to make the energy. Therefore, it has been scantily used in Europe such as Germany, Spain, France, Portugal, UK, Italy and Denmark (World Wide Energy Association, 2011).

For the geothermal energy, which can be extracted from heat in the deep earth, the environmental impact must be taken into consideration. Using the geothermal has been limited in some developed countries because the poisoning ores, such as sulfur in the form of hydrogen sulfide, spread out on the ground and possibly dissolve in water to form an acid have an effect on the ecology and the agriculture products (Hancock and Skinner, 2000). For using the energy from water, widespread application is the hydropower plant. The application can be achieved by converting mechanical energy into electricity. Most countries include Thailand construct dams to generate the electric power, which requires the commodious area supply for management. This trouble has led to the global change in the forest and the severe affect to the animals and plants (Cave, 1998). Furthermore, with the combination of the global warming, the volume of water available for the hydropower plant may inadequate in the future when the consumable water and also the electric energy are simultaneously increased (World Wind Energy Association, 2011).

One of the alternative power sources is thus the biodiesel or biogases from wastrels because of its low operating cost for built up electricity. However, their manufacturing process involves the generation of the hydrocarbon species. This hydrocarbon is the main component that accelerates the global warming (Koven, et al., 2011). Moreover, the biodiesel productions use oil from the crops such as palm, chaff and bean. Using this energy source consequently suffers from an inadequate agriculture product for foods (Dong, 2007). Another drawback of the biodiesel and biogas is the energy consumption of the production. Because the biofuel processes consume much of energy (e.g., mass transportation). It requires further development in terms of output-per-input energy consumptions.

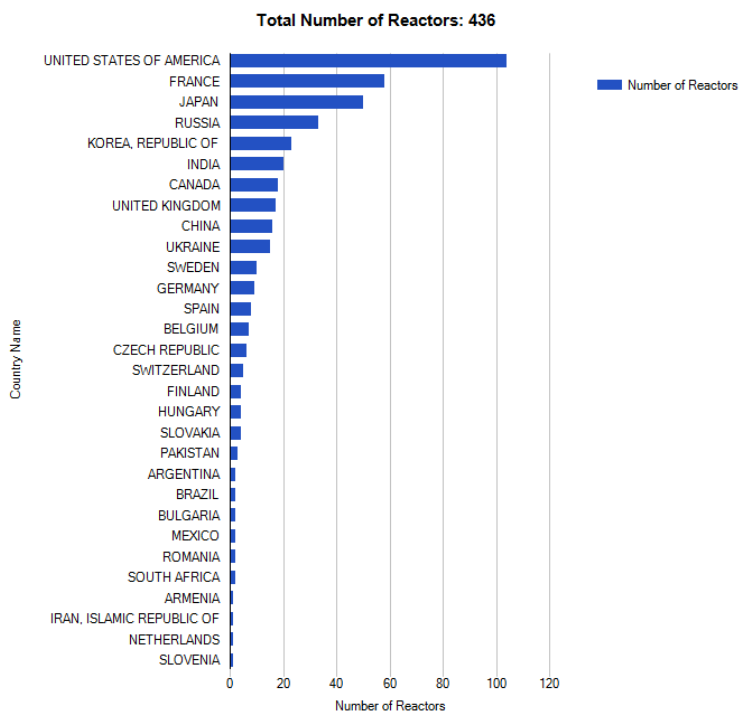


Figure 1.1 World's nuclear reactors (International Atomic Energy Agency, 2012).

One of the remarkable energy sources is the sun power. It provides the energy for all living things on Earth. However, the storage of the solar energy has some troubles. Solar energy is not available at night, making energy storage an important issue in order to provide the continuous availability of energy (Biello, 2009). Moreover, the solar cell researches and developments have not been accomplished. The solar cells have been used limitedly in some developed countries. The major disadvantage of this device is the high operating cost. Therefore, most of the regular energy source in the developing and undeveloped countries is tend to be the inexpensive energy sources without emphasizing the alternative environment-benign. In an alternative way, the powerful energy source for the power plant is known to be the electric energy generated by nuclear reaction. It has been reported that there are 436 currently nuclear reactors around the world as shown in Figure 1.1

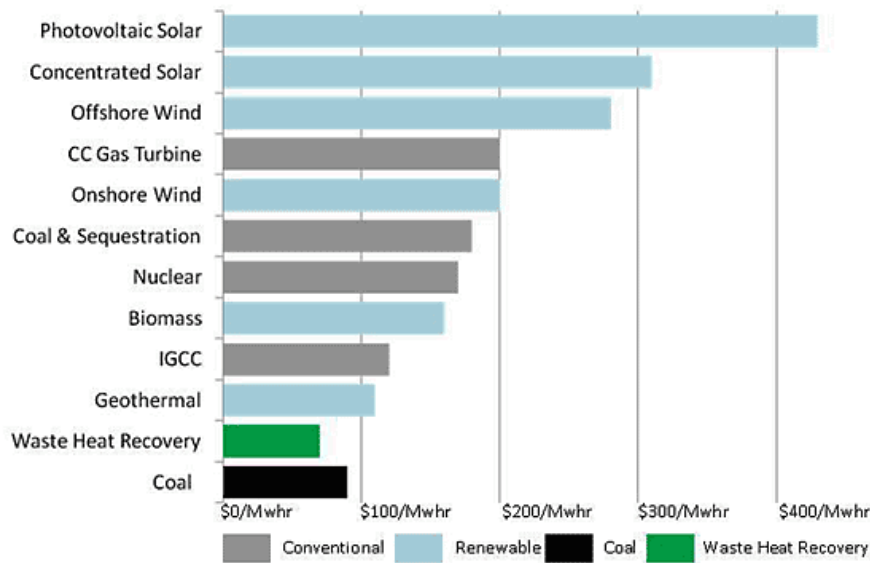


Figure 1.2 Capital costs / megawatt in millions of dollars (Gold, 2011).

Even though the nuclear power plants generate high energy density and lower the capital cost (shown in Figure 1.2) which is the essential requirement for many industrial sectors, the preparation of the nuclear fuel terribly affects the environments as expected. Because the ionizing particles liberated from the nuclear source are the harmful activity to the living organisms, extracting the electricity from the nuclear power as well as their by-product management have meticulously been considered. In fact, it is always difficult either to remove the leaked radioactive, or to purify the environment (U.S. Nuclear Regulatory Commission, 2011).

Presently, the high regularity Fukushima nuclear power plants in Japan suffer from an excessive earthquake (9.0 M_L) near the east of Honshu and followed by a massive Tsunami. Until now, the electric power is closed but the emphatic problem is to remove the nuclear radioactive (i.e., iodine 131) from the exploded plants (shown in Figure 1.3). At that time, many food products contaminated with radioactive materials have temporally been banded in China, South Korea and Taiwan.



Figure 1.3 Fukushima nuclear power plants explosion (Daily Kos, 2011).

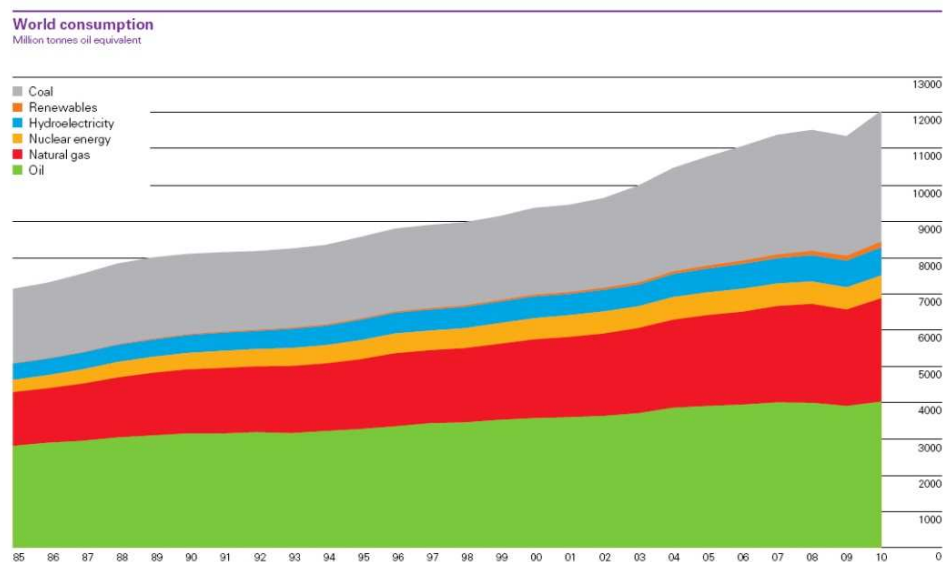


Figure 1.4 Worldwide energy consumption in 2010 (BP P.L.C, 2011).

From these serious problems, the requirement of energy source has been turned back to the global energy resource provided by the simple fossil fuels such as crude oil and natural gas.

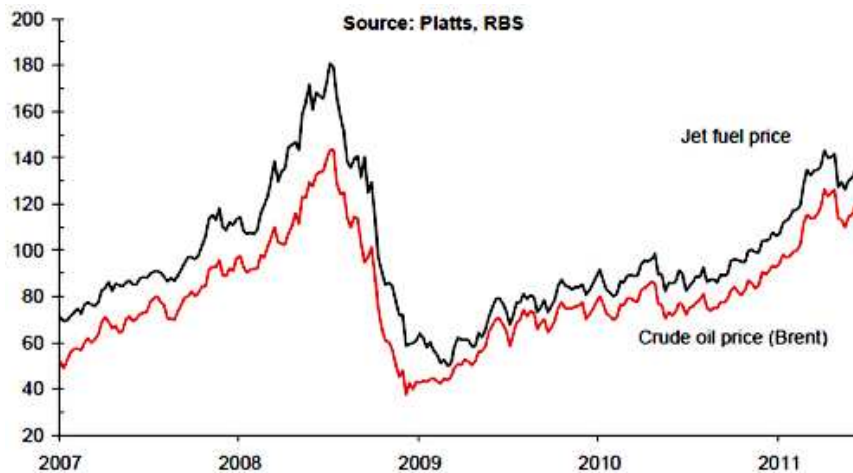


Figure 1.5 The Air Transport Association (IATA) crude oil price reports. The price is now rising up to 110 \$ due to .the political problem and financial sanction in Iran and Libyan crisis (CAPA Center for Activation, 2011).

The requirement of these fuels is increased while their price is continuously increased. Figure 1.4 depicts the worldwide energy consumption in 2010. As describe above, the major concerning in the fossil fuels application is the environmental impact. The by-products or residue of the fossil fuels regularly compose of the carbon-containing species which enhances the global warming.

Moreover, it is well known that these conventional fuels are not going to last more than 93.9 years in the face of accelerated increasing demand in the developed and developing countries (BP P.L.C, 2010). With the political confliction problem in the Middle East, the International Air Transport Association (IATA) revealed that the average oil price for 2011 is now \$110 per barrel, a 15% increase over the previous forecast (shown in Figure 1.5). Moody's investors services also reported that the persistent oil prices around \$100 a barrel will weaken the global economic recovery and hit hardest the auto, airline, gaming and agricultural sectors.

This energy crisis is one of the most concerning problems and directly affects our life style in near future. For instance, this unexpectedly price encourages the scientific researches to develop alternative energy sources. The number of the researches and developments in this purpose has been potentially increased.

Among the energy sources researches this day, electricity extracted from the electrochemical reaction of the fuel cell is expected to be a superior energy source because of its high energy conversion, efficiency and low pollution. It is well known that the energy density of fuel cell is higher than the energy density generated by the combustion engines because fuel cells produce electricity directly from chemical energy. Fuel cells are also known to be the hydrogen technology that uses hydrogen as a fuel. In addition, hydrogen is the modern technology used for the energy revolution in near future. But the chronicle of hydrogen begins with the Big Bang theory of universe creation 15 billion years ago, when hydrogen atoms were first formed. Up to date, the hydrogen content in our life is increased especially in the fuel cells applications. And also the fuel cell application needs hydrogen.

1.2 Introduction to Fuel Cell Technology

Fuel cell is an electrochemical device that converts chemical energy from a fuel into electric energy. Without any harmful emissions, fuel cell is therefore an extremely environmentally friendly device. Unlike batteries operation, fuel cells use an external fuel such as hydrogen and external oxidant such as oxygen or air to support the operation. This advantage allows the continuous operation as long as the fuel and oxidant are supplied. Presently, there are many fuel cell researches and development for transportation, power plant and portable electronic devices.

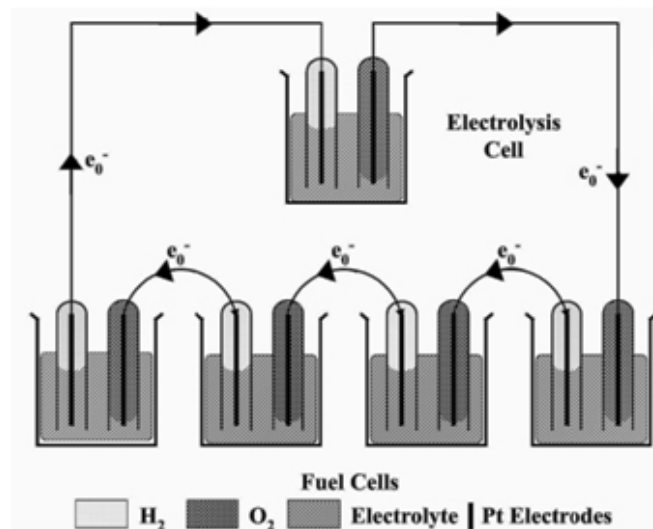


Figure 1.6 First demonstration of a fuel cell by Grove in 1839 (Barbir, 2005).

The first fuel cell was established by an English scientist named Sir William Robert Grove in 1839. Grove's simple fuel cell consists of two rods of platinum electrode placed within the hydrogen and oxygen gas tubes submerging in a bath of dilute sulfuric acid electrolyte solution and connected with the external load as shown in Figure 1.6. This reverse water electrolysis reaction generates voltage of about 1V. Up to date, fuel cells have been continuously developed.

Fuel cell is classified into five types based on the type of electrolyte they use,

1. Polymer electrolyte membrane fuel cells (PEMFC)
2. Alkaline fuel cells (AFC)
3. Phosphoric acid fuel cells (PAFC)
4. Molten carbonate fuel cells (MCFC)
5. Solid oxide fuel cells (SOFC).

In general, the fuel cells can be classified in terms of their operating temperature. The first three types are low temperature and the last two types are high temperature fuel cells. The description of fuel cell types are shown in Table 1.1.

Table 1.1 Classification of fuel cells.

Fuel cell types	Operating temperature (°C)	Efficiency (%)	Suitable applications			
			Domestic power	Small scale power	Large scale cogeneration	Trans-port
AFC	50-90	50-70	√	√	X	√
PEMFC	50-120	40-50	√	√	X	√
PAFC	175-220	40-45	X	√	X	X
MCFC	600-650	50-60	X	√	√	X
SOFC	800-1000	50-60	√	√	√	X

1.2.1 Polymer electrolyte membrane fuel cells

Polymer electrolyte membrane (or proton exchange membrane) fuel cells (PEMFCs) have initially been established by General electric for the Gemini space mission during the mid 1960s. The electrolyte membranes are based on polystyrene sulfonic acid (PSSA). At that time, the PEMFCs suffered from the high operating cost due to the essentials of more platinum catalyst and membranes. The fuel cells were then noticeably developed until now. The platinum catalyst has been reduced from 28 mg/cm² to 0.2 mg/cm² while maintaining current densities. Nevertheless, the breakthrough of the fuel cells technology is in virtue of the discovery of the perfluoropolymer namely Nafion by DuPontTM. The details of this polymer will be discussed in Chapter III.

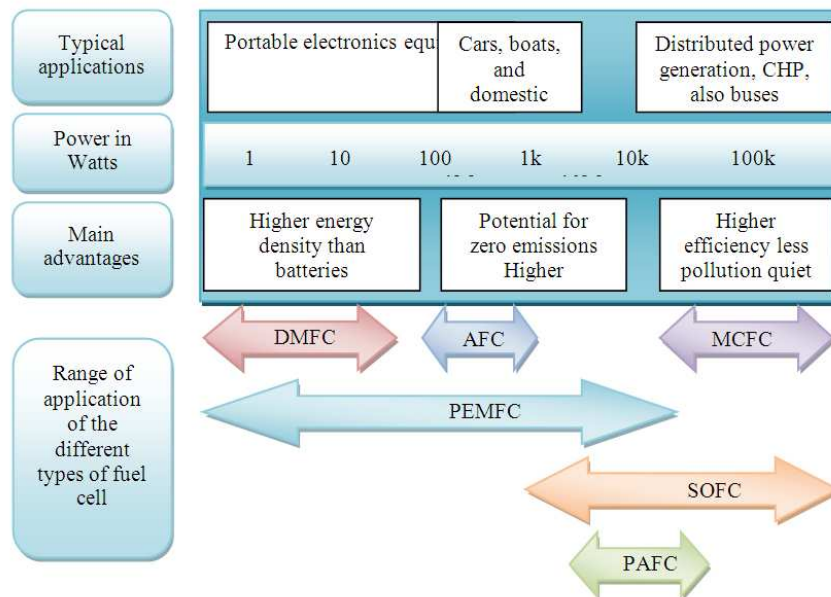


Figure 1.7 Summarized fuel cell applications.

The PEMFCs have been widely used as the electric power source for the vehicle and the small combined heat and power (CHP) systems because of the low operating temperature.

1.2.2 Fuel cell applications

As fossil fuels are running out, hydrogen is being the superlative world's fuel. Due to its high efficiency and low emission, fuel cell is the future energy generator. The advantages of fuel cells impact particularly strongly on combined heat and power (CHP) and on mobile power systems, especially for vehicles and electronic equipments such as portable computers, mobile telephones. The portable and automobile applications are the major scientific fields in which fuel cells are used. Figure 1.7 summarizes the fuel cell applications.

1.3 Scope and Limitations of the Study

This thesis focuses on the surface modification of the Nafion membrane, which is used in the PEMFCs, from the photo-degradation mechanism. It has been generally accepted that most of polymers can undergo photo-degradation in different weather conditions. Exposure the membrane to direct sun light in the surrounding of air for a long period of time inevitably results in the acceleration of the degradation.

Using the degraded membrane leads to the lowering in the PEMFC performance and also the fuel cell failure. The membrane deterioration is one of major fuel cell problems, either in terms of performance or in terms of durability. Due to the high cost of new membrane, the modification of the degraded membrane is therefore an alternative way to solve this problem. Based on the assumption of that if light causes the membrane degradation, the membrane should also be modified by the same type of light. More specifically, the light used for the membrane modification is the high intensity of the vacuum ultraviolet (VUV) radiations from the synchrotron radiation. Various photon doses irradiate on the surface of the degraded membrane, which contain the existence of some contaminations or residuals, in an ultrahigh vacuum (UHV) system. It is expected that the surface structure of the irradiated membranes would be modified upon the VUV irradiation doses.

The performance of the PEMFC using these irradiated membranes has subsequently been verified by the PEMFC performance tests in term of the polarization curves. These structural changes have also been investigated by photoemission spectroscopy (PES), atomic force microscopy (AFM), mass spectrometry and small angle X-ray scattering (SAXS).

Due to the low performance of the PEMFC using the degraded membrane compared with the fresh membrane, the performance of the VUV recovered membrane is suppose to be inferior to that of the fresh Nafion membrane. However, the relative improvement of their performance and also the dynamical changes at their surface has been succeeded. These investigations suggest an avenue for direct experimental test of the degraded Nafion membrane after VUV irradiations.



CHAPTER II

PROTON EXCHANGE MEMBRANE FUEL CELLS

2.1 Basic Principle of PEMFCs

Among the various types of fuel cells, the proton exchange membrane fuel cell is the most preferable choice as the electric power source for transportations and small electric devices because of their essential simplicity, quick start-up and ambient temperature operations. The PEMFCs also exhibit high-operational efficiencies unlike internal combustion engines, in which the efficiency is limited by the Carnot's law.

The electrolyte of PEMFCs is a solid polymer that allows transportation of protons and resists the electrons to pass through. Using a solid and immobile electrolyte makes the fuel cell simple and offers the advantage of low weight and volume, compared to other type of fuel cells. PEMFCs operate at a temperature of 80°C and only require hydrogen, oxygen and water to function.

A schematic diagram of a PEMFC is shown in Figure 2.1. A significant component of this type of fuel cell is the membrane electrode assembly (MEA) that composed of a thin (typically 50-200 μm) cation (proton) exchange membrane (usually hydrated to promote proton transport) with precious metal catalyst (typically platinum) electrodes pressed directly onto the opposing membrane surface.

Adjacent to the electrodes are carbon fiber paper or carbon cloth gas diffusion layers (GDLs), which assist in distributing gas to the catalyst and removing products from the electrodes (e.g., water from the air cathode).

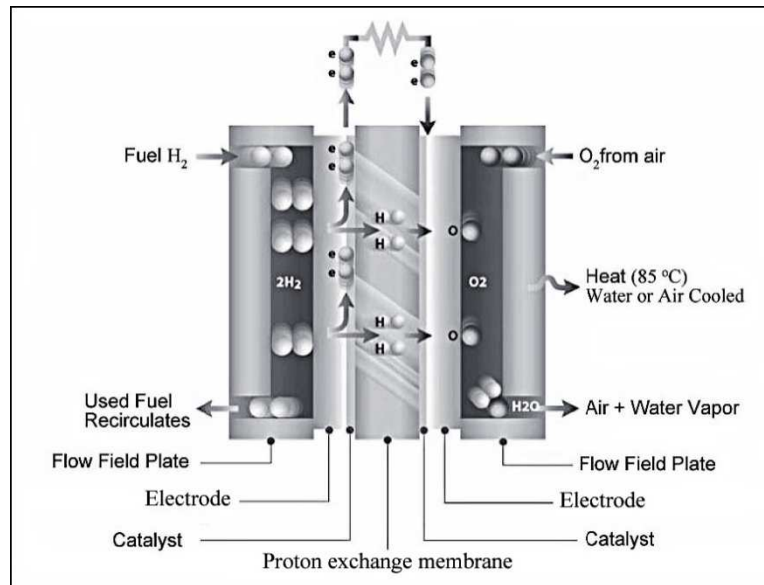
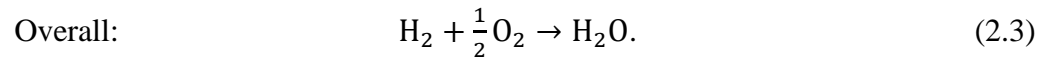
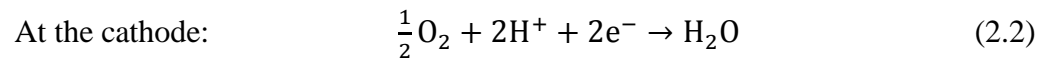
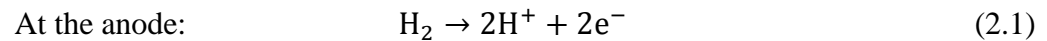


Figure 2.1 PEMFC components. (Ismail, Naim and Zubir, 2009).

Additionally, the combination of the carbon cloth gas diffusion layer and the active catalyst layer is called the gas diffusion electrodes (GDEs) (Francisco, Cabot and Brillas, 2007). By sandwiching the polymer electrolyte membrane with the GDEs, the MEA is fabricated. The MEA is then connected with two graphite flow-field plates and two collector plates. This complete single PEMFC is connected with the gas-flow systems and external electronic loader. At the interface between anode and the electrolyte, the fuel is converted into proton (H^+) and electron (e^-), a process which is made possible by a catalyst that is typically Pt-based.

Polymer electrolyte membrane allows protons to flow through, but prevents electrons from passing through. Electrons travel to the cathode via an external circuit producing electrical current and H^+ -ions (proton) pass through the membrane from anode to cathode, where they combine with oxygen molecules and electrons to form water. The basic fuel cell reactions taking place in a PEMFC are



2.2 Fuel Cell Components

Fuel cells generate electricity from hydrogen and oxygen without any harmful emissions and therefore in an extremely environmentally friendly way. As described earlier, the heart of a fuel cell is a polymer, proton-conductive membrane. The surface of the membrane is connected electrically with porous electrodes. The reactant gases are fed from the back and must reach the interface between the porous electrodes and the membrane, where the electrochemical reactions take place at the catalyst layers, or more precisely, on the catalyst surface. A proton exchange membrane is placed at the center of the PEMFC. Hydrogen fed to the anode side ionizes into protons and electrons at the catalyst. The protons pass the catalyst layer, while the electrons remaining behind give a negative charge to the hydrogen-side electrode. During the proton migration, a voltage difference builds up between the electrodes. When they are connected, the potential difference produces a direct current that can drive an engine.

Finally, the protons recombine with the electrons and oxygen into water at the cathode. Besides the produced electric energy, the only by-product is water. Additionally, heat is produced by the electrochemical reactions and the contact resistances in the fuel cell, which can be used for space or service water heating.

2.2.1 Electrode

A fuel cell electrode is a thin catalyst layer pressed between the ionomer membrane and porous, electrically conductive substrate. It is the layer where the electrochemical reactions take place.

More precisely, the electrochemical reactions take place on the catalyst surface. There are three kinds of species that participate in the electrochemical reactions, namely gases, electrons and protons. Thus, the reactions occur on a portion of the catalyst surface where all three species have access. Electrons travel through electrically conductive solids, including the catalyst itself, but it is important that the catalyst particles are electrically connected to the substrate. Protons travel through membrane; therefore the catalyst must be contact with the membrane. And finally, the reactant gases travel only through voids; therefore the electrode must be porous to allow gases to travel to the reaction sites. At the same time, product water must be removed; otherwise the electrode would be flooded and prevent oxygen access.

As shown graphically in Figure 2.2a, the reactions take place at the three-phase boundary, which compose of ionomer, solid, and void phases. However, this boundary has an infinitesimally small area (essentially it is a line not an area) that would result in infinitely large current densities. Practically, due to the gas permeation through the polymer, the reaction zone is larger than a single three-phase boundary line. The reaction zone can be enhanced either by "roughening" the membrane surface, or by incorporating ionomer in the catalyst layer (as shown in Figure 2.2b). In an extreme case, the entire catalyst surface may be covered by a thin ionomer layer (Figure 2.2c), except for some allowance for electrical contacts.

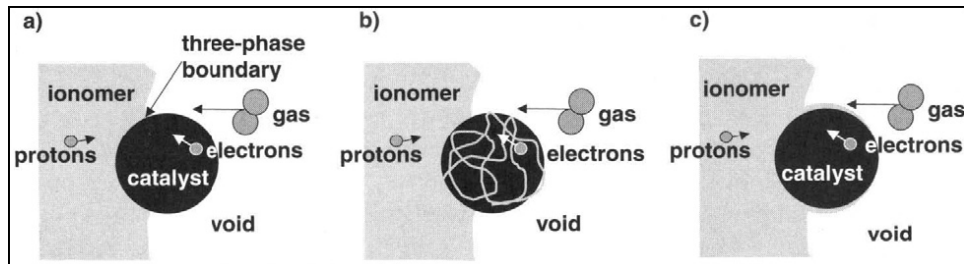


Figure 2.2 Graphical representations of the reaction sites (Barbir, 2005).

Obviously, the ratios between the catalyst area which covered by ionomer to catalyst area opened to void to catalyst area contacting other catalyst particles or electrically conductive support must be optimized. The most common catalyst in PEM fuel cells for both oxygen reduction and hydrogen oxidation reactions is platinum. In the early days of PEMFC development, large amounts of Pt catalyst were used (up to $28\text{mg}/\text{cm}^2$). In the late 1990s, with the use of supported catalyst structure, the catalyst was reduced to $0.3\text{-}0.4\text{ mg}/\text{cm}^2$. It is the catalyst surface area that matters, not the weight, so it is important to have small platinum particles (4 nm or smaller) with large surface area finely dispersed on the surface of catalyst support.

2.2.2 Membrane

The membrane has two functions. Firstly, it acts as an electrolyte that provides ionic conduction between the anode and the cathode but is an electronic insulator. Secondly, it serves as a separator for the two-reactant gases. Solid polymer membranes used in PEMFC are simpler, more reliable and easier to maintain than other membrane types (Ismail, Naim and Zubir, 2009). The fuel cell must operate under conditions in which the by-product water does not evaporate faster than it is produced, because the membrane must be hydrated.

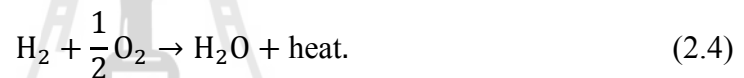
2.3 Fuel Cell Thermodynamics

Because a fuel cell is an energy convertor, the thermodynamics of the fuel cell, such as energy transfer, effect of temperature and efficiency, play an important role as well as the fuel cell electrochemistry.

The following subsections provide basic principle of the fuel cells thermodynamics, which gives the potential for reaction.

2.3.1 Heat of reaction

The overall reaction described in Equation (2.3) is similar to the hydrogen combustion reaction. Combustion is an exothermic process, which means that there is energy released in the process. The reaction can be expressed as



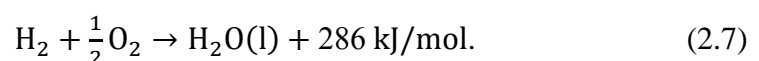
The heat (or enthalpy) of a chemical reaction is the difference between the heats of formation of products and reactants.

$$\Delta H = (h_f)_{\text{H}_2\text{O}} - (h_f)_{\text{H}_2} - \frac{1}{2}(h_f)_{\text{O}_2}. \quad (2.5)$$

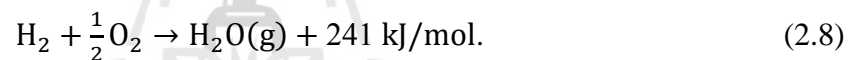
Note that (h_f) is the heat of formation. In liquid water (at 25°C), $(h_f)_{\text{H}_2\text{O}}$ is -286 kJ/mol. And heat of formation of elements is by definition equal to zero. Therefore, at 25°C and atmospheric pressure, the enthalpy is

$$\Delta H = -286 \text{ kJ/mol.} \quad (2.6)$$

Note that the negative sign for enthalpy of a chemical reaction, by convention, means that heat is being released in the reaction, this is an exothermic reaction. Equation (2.4) may now be rewritten as



A positive sign is used because the enthalpy is placed on the right side of the reaction, clearly meaning a product of the reaction. This equation is valid at 25°C only, meaning that both the reactant gases and the product water are at 25°C, where the water in the atmospheric pressure is in liquid form. The enthalpy of hydrogen combustion reaction in Equation (2.6) is also called the hydrogen's heating value, which is the amount of heat that may be generated by a complete combustion of 1 mol of hydrogen. However, if hydrogen is combusted with sufficient excess of oxygen (or air) and allowed to cool down to 25°C, the product water will be in the form of vapor mixed with unburned oxygen and/or nitrogen in case that air was used. The measurement should show that less heat was released, exactly 241 kJ. This is known as hydrogen's lower heating value (Barbia, 2005)



2.3.3 Theoretical electrical work

Hydrogen heating value is used as a measure of energy input in a fuel cell. This is the maximum amount of (thermal) energy that may be extracted from hydrogen. However, in every chemical reaction some entropy is produced, not all of the hydrogen's higher heating value can be converted into useful work-electricity. A portion of the reaction enthalpy (or hydrogen's higher heating value) that can be converted to electricity in a fuel cell corresponds to Gibbs free energy and is given by the following equation:

$$\Delta G = \Delta H - T\Delta S. \quad (2.9)$$

Note that ΔS is the difference between entropies of products and reactants:

$$\Delta S = (s_f)_{\text{H}_2\text{O}} - (s_f)_{\text{H}_2} - \frac{1}{2}(s_f)_{\text{O}_2}. \quad (2.10)$$

Table 2.1 Enthalpies and entropies of formation for fuel cell reactants and products.

	h_f (kJ/mol)	s_f (kJ/mol·K)
Hydrogen, H ₂	0	0.13066
Oxygen, O ₂	0	0.20517
Water (liquid), H ₂ O (l)	-286.02	0.06996
Water (vapor), H ₂ O (g)	-241.98	0.18884

The values of h_f and s_f for reaction reactants and products at atmospheric pressure and 25°C are shown in Table 2.1. Therefore, at 25°C, out of 286.02 kJ/mol of available energy, 237.34 kJ/mol can be converted into electrical energy and the remaining 48.68 kJ/mol is converted into heat.

2.3.4 Theoretical fuel cell potential

According to the definition of electrical work:

$$W_{el} = qE, \quad (2.11)$$

where

W_{el} = electrical work (J/mol)

q = charge (Coulomb/mol)

E = electric potential (Volt).

The total charge transferred in a fuel cell reaction per mol of H₂ consumption is equal to:

$$q = nN_A q_{el} \quad (2.12)$$

where

n = number of electrons per molecule of H_2 = 2 electrons per molecule

N_A = number of molecule per mol (Avogadro's number = 6.022×10^{23} molecules/mol)

q_{el} = charge of 1 electron (= 1.6×10^{-19} Coulombs/electron)

The product of Avogadro's number and charge of 1 electron is known as Faraday's constant:

$$F = 96,485 \text{ Coulombs/electron} \cdot \text{mol}. \quad (2.13)$$

Electrical work is therefore:

$$W_{el} = nFE. \quad (2.14)$$

The maximum amount of electrical energy generated in a fuel cell corresponds to Gibbs free energy, ΔG :

$$W_{el} = -\Delta G. \quad (2.15)$$

The theoretical potential of fuel cell is then:

$$E = \frac{\Delta G}{\Delta H} = \frac{237340 \text{ J/mol}}{2 \times 96,485 \text{ A s/mol}} = 1.23 \text{ V}. \quad (2.16)$$

Consequently, at 25°C , the theoretical PEMFC potential is equal to 1.23 V, which is the maximum potential of the fuel cell.

2.4 Fuel Cell Electrochemistry

The heart of the fuel cell operation is the fuel cell electrochemistry that has generated on the anode and the cathode. More precisely, the electrochemical reactions occur on an interface between the ionically conductive electrolyte and electrically conductive electrode.

2.4.1 Reaction rate

Electrochemical reactions involve both a transfer of electrical charge and a change in Gibbs energy. The rate of an electrochemical reaction is determined by an activation energy barrier that the charge must overcome in moving from electrolyte to a solid electrode or vice versa. The speed at which an electrochemical reaction proceeds on the electrode surface is the rate at which the electrons are released or consumed, which is the electrical current. Current density is the current (of electrons or ions) per unit area of the surface. From Faraday's law, it follows that current density is proportional to the charge transferred and the consumption of reactant per unit area:

$$i = nFj \quad (2.17)$$

where nF is the charge transferred (Coulombs/mol) and j is the flux of reactant per unit area (mol/s cm^2).

The reaction rate can easily be measured by a current-measuring device placed external to the cell. However, the measured current or current density is actually the net current, that is, the difference between forward and reverse current on the electrode. In general, an electrochemical reaction involves either oxidation or reduction of the species:



On an electrode at equilibrium conditions, when no external current is being generated, both processes, oxidation and reduction, occur at equal rates:



The consumption of the reactant species is proportional to their surface concentration. For the forward reaction of Equation (2.20), the flux is defined as

$$j_f = k_f C_{Ox} \quad (2.21)$$

where

k_f is forward reaction (reduction) rate coefficient, and

C_{Ox} is surface concentration of the reacting species

Equivalently, for the backward reaction of Equation (2.20), the flux is:

$$j_b = k_b C_{Rd} \quad (2.22)$$

where

k_b = backward reaction (reduction) rate coefficient, and

C_{Rd} = surface concentration of reacting species.

These reactions either releases or consumes electrons. The net current generation is the difference between the electrons released and consumed:

$$i = nF(k_f C_{Ox} - k_b C_{Rd}). \quad (2.23)$$

At equilibrium, the net current is equal to zero, although the reaction proceeds in both directions simultaneously. The rate at which these reactions proceed at equilibrium is called the "exchange current density".

2.4.2 Reaction constants and transfer coefficient

From the transition state theory (Atkins, 1998), the reaction rate coefficient for an electrochemical reaction can be expressed as a function of the Gibbs free energy:

$$k = \frac{k_B T}{h} \exp\left(\frac{-\Delta G}{RT}\right), \quad (2.24)$$

where k_B = Boltzmann's constant and h = Planck's constant.

Generally, the Gibbs free energy for electrochemical reactions consists of both chemical and electrical terms. In that case, for a reduction reaction:

$$\Delta G = \Delta G_{\text{ch}} + \alpha_{\text{Rd}}FE, \quad (2.25)$$

and for oxidation reaction:

$$\Delta G = \Delta G_{\text{ch}} - \alpha_{\text{Ox}}FE. \quad (2.26)$$

The subscript "ch" denotes the chemical component of the Gibbs free energy, α is a transfer coefficient, F is the Faraday's constant, and E is the potential. The forward (reduction) and backward (oxidation) reaction rate coefficients in Equation (2.23) can be expressed, respectively:

$$k_f = k_{0,f} \exp \left[\frac{-\alpha_{\text{Rd}}FE}{RT} \right] \quad (2.27)$$

$$k_b = k_{0,b} \exp \left[\frac{\alpha_{\text{Ox}}FE}{RT} \right]. \quad (2.28)$$

2.4.3 Current potential relationship—Butler-Volmer equation

By introducing into Equation (2.23) the net current, density is obtained:

$$i = nF \left\{ k_{0,f} C_{\text{Ox}} \exp \left[\frac{-\alpha_{\text{Rd}}FE}{RT} \right] - k_{0,b} C_{\text{Rd}} \exp \left[\frac{\alpha_{\text{Ox}}FE}{RT} \right] \right\}. \quad (2.29)$$

At equilibrium, the potential is referred to E_r , and the net current is equal to zero, although the reaction proceeds in both directions simultaneously. The exchange current density is then

$$i_0 = nF k_{0,f} C_{\text{Ox}} \exp \left[\frac{-\alpha_{\text{Rd}}FE_r}{RT} \right] = nF k_{0,b} C_{\text{Rd}} \exp \left[\frac{\alpha_{\text{Ox}}FE_r}{RT} \right]. \quad (2.30)$$

By combining the Equations (2.29) and (2.30), a relation between the current density and potential is obtained

$$i = i_0 \left\{ \exp \left[\frac{-\alpha_{\text{Rd}}F(E - E_r)}{RT} \right] - \exp \left[\frac{\alpha_{\text{Ox}}F(E - E_r)}{RT} \right] \right\}. \quad (2.31)$$

This is known as the Butler-Volmer equation, where E_r is equilibrium (or reversible) potential. Note that the equilibrium potential at the fuel cell anode is 0 V by definition (Bockris and Srinivasan, 1969), and the equilibrium potential at the fuel cell cathode is 1.229 V and it does vary with temperature and pressure. The difference between the electrode potential and the equilibrium potential is called "overpotential". It is also the potential difference required to generate current.

Generally, the Butler-Volmer Equation is valid for both anode and cathode reaction in a fuel cell:

$$i_a = i_{0,a} \left\{ \exp \left[\frac{-\alpha_{Rd,a} F (E_a - E_{r,a})}{RT} \right] - \exp \left[\frac{\alpha_{Ox,a} F (E_a - E_{r,a})}{RT} \right] \right\} \quad (2.32)$$

and

$$i_c = i_{0,c} \left\{ \exp \left[\frac{-\alpha_{Rd,c} F (E_c - E_{r,c})}{RT} \right] - \exp \left[\frac{\alpha_{Ox,c} F (E_c - E_{r,c})}{RT} \right] \right\}. \quad (2.33)$$

The overpotential on the anode is positive ($E_a > E_{r,a}$) which makes the first term of the Equation (2.32) negligible in comparison with the second term, that is, the oxidation current is predominant and the equation may be reduced to:

$$i_a = -i_{0,a} \exp \left[\frac{\alpha_{Ox,a} F (E_a - E_{r,a})}{RT} \right]. \quad (2.34)$$

Note that the resulting current has a negative sign, which denotes that the electrons are leaving the electrode (net oxidation reaction).

Similarly, the overpotential on the cathode is negative ($E_c < E_{r,c}$), which makes the first term of the Equation (2.33) much larger than the second term. Therefore, the reduction current is predominant and the equation may be reduced to:

$$i_c = i_{0,c} \exp \left[\frac{-\alpha_{Rd,c} F (E_c - E_{r,c})}{RT} \right]. \quad (2.35)$$

2.4.4 Voltage losses

If a fuel cell is supplied with reactant gases, but the electrical circuit is not closed (shown in Figure 2.4a), it will not generate any current, and one would expect the cell potential to be at, or at least close to, the theoretical cell potential for given conditions (temperature, pressure, and concentration of reactants). However, in practice this potential, called the open circuit potential or open circuit voltage (OCV), is significantly lower than the theoretical potential. This suggests that there are some losses in the fuel cell even when no external current is generated. When the electrical circuit is closed with a load (such as a resistor) in it, as shown in Figure 2.4b, the potential is expected to drop even further as a function of current being generated, due to unavoidable losses. Thus, there are different kinds of voltage losses in a fuel cell which are offered by the following factors, for example

1. kinetics of the electrochemical reactions
2. internal electrical and ionic resistance
3. difficulties in getting the reactants to reaction sites
4. internal currents
5. crossover of reactants

Note that, although mechanical and electrical engineers prefer to use voltage losses, electrochemical researchers use terms such as polarization or over potential. They all have the same physical meaning—difference between the electrode potential and the equilibrium potential. From the electrochemistry point of view, this difference is the driver for the reaction, and from a mechanical or electrical engineer's point of view, this represents the loss of voltage and power.

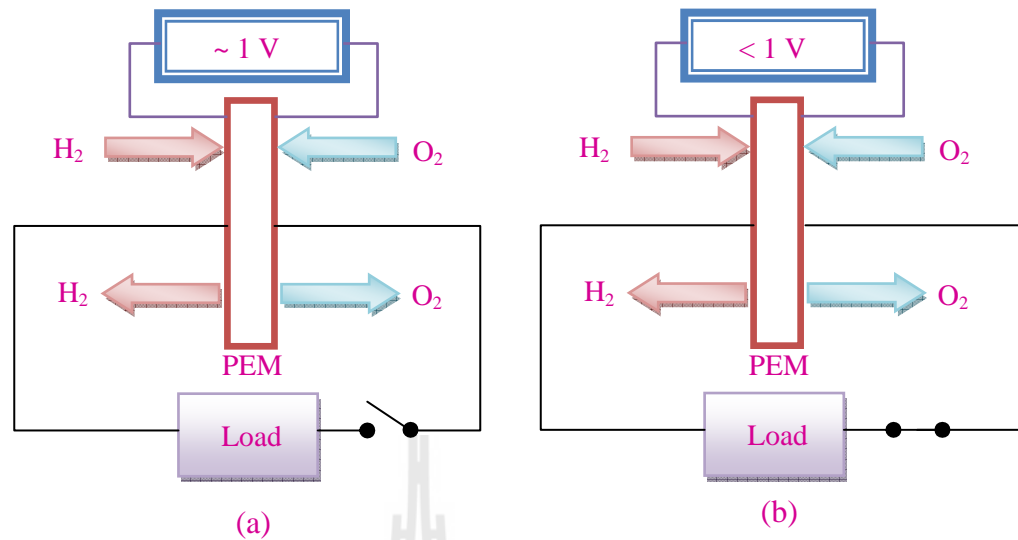


Figure 2.4 Fuel cell with a load: (a) load disconnected; (b) load connected.

2.4.4.1 Activation polarization

Some voltage difference from equilibrium is needed to get the electrochemical reaction going, as shown previously in Equation (2.31). This is called activation polarization, and it is associated with sluggish electrode kinetics. The higher the exchange current density results in the lower the activation polarization losses. These losses happen at both anode and cathode, however, oxygen reduction requires much higher over potentials, and it is a much slower reaction than hydrogen oxidation.

At relatively high negative over potentials (i.e., potentials lower than the equilibrium potential), such as those at the fuel cell cathode, the first term in the Butler-Volmer equation becomes predominant, which allows for expression of potential as a function of current density.

$$\Delta V_{\text{act,c}} = E_{\text{r,c}} - E_{\text{c}} = \frac{RT}{\alpha_{\text{c}}F} \ln \left(\frac{i}{i_{0,\text{c}}} \right). \quad (2.36)$$

Similarly, at the anode at positive over potentials (i.e., higher than the equilibrium potential) the second term in the Butler-Volmer equation becomes predominant:

$$\Delta V_{\text{act,a}} = E_a - E_{r,a} = \frac{RT}{\alpha_a F} \ln \left(\frac{i}{i_{0,a}} \right). \quad (2.37)$$

In electrochemistry, the reversible potential of the hydrogen oxidation reaction is zero at all temperatures (Bard and Faulkner, 1980). The standard hydrogen electrode is then used as a reference electrode. Therefore, for hydrogen anodes $E_{r,a} = 0$ V. Activation polarization of the hydrogen oxidation reaction is much smaller than activation polarization of the oxygen reduction reaction.

A simplified way to show the activation losses is to use the so-called "Tafel equation" expressed as

$$\Delta V_{\text{act}} = a + b \log(i), \quad (2.38)$$

where

$$a = -2.3 \frac{RT}{\alpha F} \log(i_0), \text{ and } b = 2.3 \frac{RT}{\alpha F}.$$

Term b is called the Tafel slope. Note that at any given temperature the Tafel slope depends solely on transfer coefficient, α . If these activation polarizations were the only losses in a fuel cell, the cell potential would be:

$$E_{\text{cell}} = E_c - E_a = E_r - \Delta V_{\text{act,c}} - \Delta V_{\text{act,a}} \quad (2.39)$$

$$E_{\text{cell}} = E_r - \frac{RT}{\alpha_c F} \ln \left(\frac{i}{i_{0,c}} \right) - \frac{RT}{\alpha_a F} \ln \left(\frac{i}{i_{0,a}} \right). \quad (2.40)$$

If anode polarization is neglected, the previous equation becomes:

$$E_{\text{cell}} = E_r - \frac{RT}{\alpha F} \ln \left(\frac{i}{i_0} \right), \quad (2.41)$$

which is the same form as the Tafel Equation (2.38).

2.4.4.2 Internal currents and crossover losses

Although the electrolyte is not electrically conductive and is practically impermeable to reactant gases, some small amount of hydrogen will diffuse from anode to cathode, and some electrons may also find a "shortcut" through the membranes. Because each hydrogen molecule contains two electrons, this fuel crossover and the so-called internal currents are essentially equivalent. Each hydrogen molecule that diffuses through the polymer electrolyte membrane and reacts with oxygen on the cathode side of the fuel cell results in two fewer electrons in the generated current of electrons that travels through an external circuit.

These losses may appear insignificant in fuel cell operation, because the rate of hydrogen permeation or electron crossover is several orders of magnitude lower than hydrogen consumption rate or total electrical current generated. However, when the fuel cell is at open circuit potential or when it operates at very low current densities, these losses may have a dramatic effect on cell potential. The total electrical current is the sum of external current and current losses due to fuel crossover and internal currents. The total current can be expressed in term of current density (i , current/unit area):

$$i = i_{\text{ext}} + i_{\text{loss}} \quad (2.42)$$

If this total current density is used in the equation that approximates the cell potential (Equation (2.42)), the following equation results:

$$E_{\text{cell}} = E_r - \frac{RT}{\alpha F} \ln \left(\frac{i_{\text{ext}} + i_{\text{loss}}}{i_0} \right). \quad (2.43)$$

Therefore, even if the external current is equal to zero, such as at open circuit, the cell voltage may be significantly lower than the reversible cell potential for given conditions. Indeed, open circuit potential of PEMFCs is typically below 1 V (depending on operating pressure).

$$E_{\text{cell,OCV}} = E_r - \frac{RT}{\alpha F} \ln \left(\frac{i_{\text{loss}}}{i_0} \right). \quad (2.44)$$

2.4.4.3 Ohmic (resistive) losses

Ohmic losses occur due to the resistance of the ions in the electrolyte and resistance of electrons through the electrically conductive fuel cell components. These losses can be expressed by Ohm's law:

$$\Delta V_{\text{ohm}} = iR_i \quad (2.45)$$

Where i = current density and R_i = total cell internal resistance (which includes ionic, electronic, and contact resistance, $\Omega \cdot \text{cm}^2$)

$$R_i = R_{i,e} + R_{i,c} \quad (2.46)$$

Electronic resistance is almost negligible, even when graphite or graphite/polymer composites are used as current collectors. Ionic and contact resistances are approximately of the same order of magnitude (Barbir, Braun and Neutzler, 1999). Typical values for R_i are 0.1-0.2 $\Omega \cdot \text{cm}^2$.

2.4.4.4 Concentration polarization

Concentration polarization occurs when a reactant is rapidly consumed at the electrode by the electrochemical reaction so that concentration gradients are established. Accordingly, the electrochemical reaction potential changes with partial pressure of the reactants, and this relationship is given by the Nernst equation:

$$\Delta V = \frac{RT}{nF} \ln \left(\frac{C_B}{C_S} \right), \quad (2.47)$$

where

C_B = bulk concentration of reactant, mol/cm³

C_S = concentration at the surface of the catalyst, mol/cm³

According to Fick's Law, the flux of reactant is proportional to concentration gradient:

$$N = \frac{D \cdot (C_B - C_S)}{\delta} A. \quad (2.48)$$

where

N = flux of reactants, mol/s

D = diffusion coefficient of the reacting species, cm²/s

A = electrode active area, cm²

δ = diffusion distance, cm

In steady state, the rate at which the reactant species is consumed in the electrochemical reaction is equal to the diffusion flux (Equation (2.17)):

$$N = \frac{i}{nF}. \quad (2.49)$$

By combining Equations (2.48) and (2.49), the following relationship is obtained:

$$i = \frac{nF \cdot D \cdot (C_B - C_S)}{\delta}. \quad (2.50)$$

The reactant concentration at the catalyst surface thus depends on current density-the higher the current density, the lower the surface concentration. The surface concentration reaches zero when the rate of consumption exceeds the diffusion rate-the reactant is consumed faster than it can reach the surface. Current density at which this happens is called the limiting current density.

A fuel cell cannot produce more than the limiting current because there are no reactants at the catalyst surface. Therefore, for $C_s = 0$, $i = i_L$ and the limiting current density is then:

$$i_L = \frac{nFDC_B}{\delta}. \quad (2.51)$$

By combining Equations (2.47), (2.50), and (2.51), a relationship for voltage loss due to concentration polarization is obtained:

$$\Delta V_{\text{conc}} = \frac{RT}{nF} \ln \left(\frac{i_L}{i_L - i} \right). \quad (2.52)$$

Additionally, an empirical equation better describes the polarization loss was expressed as (Kim, Srinivasan and Chamberlain, 1995):

$$\Delta V_{\text{cons}} = c \cdot \exp \left(\frac{i}{d} \right) \quad (2.53)$$

where c and d are empirical coefficients (values of $c = 3 \times 10^{-5}$ V and $d = 0.125$ A/cm² have been suggested (Larminie and Dicks, 2003).

2.4.5 Cell potential-polarization curve

Figure 2.5 summarizes the proportions between the three types of losses in the fuel cell. Activation losses are by far the largest losses at any current density. Activation and concentration polarization can occur at both anode and cathode. The cell voltage is therefore:

$$V_{\text{cell}} = E_r - (\Delta V_{\text{act}} - \Delta V_{\text{conc}})_a - (\Delta V_{\text{act}} - \Delta V_{\text{conc}})_c - \Delta V_{\text{ohm}}. \quad (2.54)$$

Figure 2.6 shows how the cell polarization characteristic is formed, by subtracting the activation polarization losses, ohmic losses, and concentration polarization losses from the equilibrium potential.

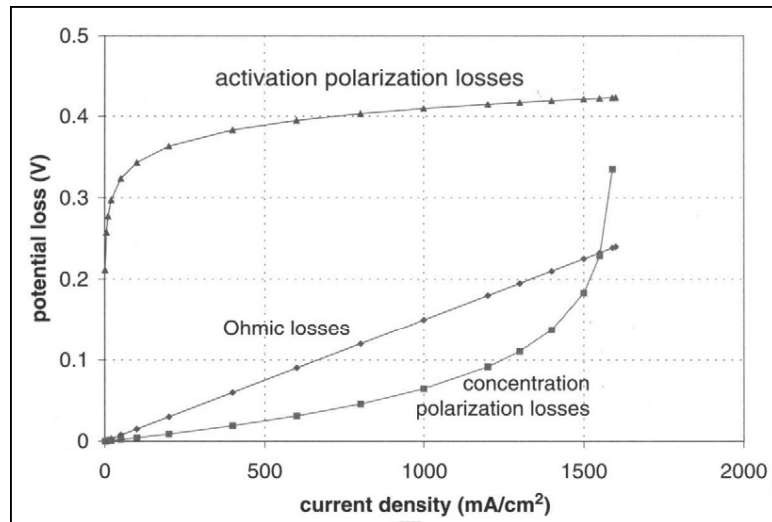


Figure 2.5 Voltage losses in the fuel cell.

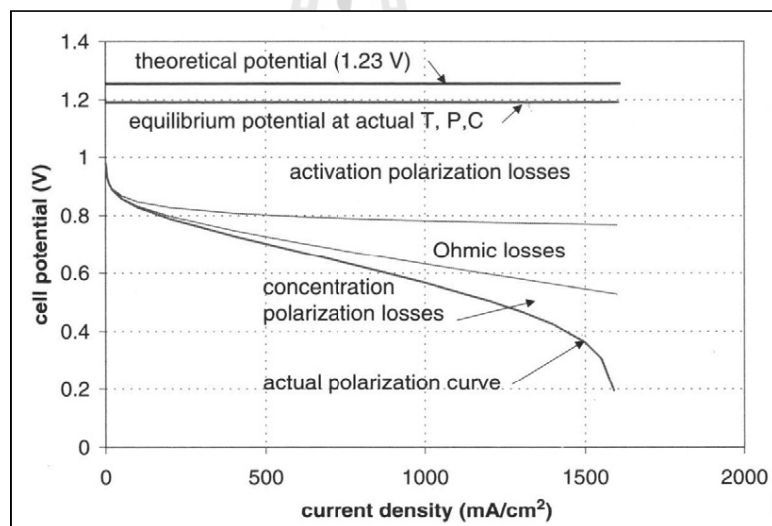


Figure 2.6 Voltage losses in fuel cell and resulting polarization curve.

The equation for the fuel cell polarization curve is the relationship between the fuel cell potential and current density, as illustrated in Figure 2.6, and can be written as

$$E_{\text{cell}} = E_r - \frac{RT}{\alpha F} \ln \left(\frac{i + i_{\text{loss}}}{i_0} \right) - \frac{RT}{nF} \ln \left(\frac{i_L}{i_L - i} \right) - iR_i \quad (2.55)$$

2.4.6 Fuel cell efficiency

The fuel cell efficiency is defined as a ratio between the electricity produced and hydrogen consumed.

$$\eta = \frac{W_{el}}{W_{H_2}} \quad (2.56)$$

Electricity produced is simply a product between voltage and current.

$$W_{el} = I \cdot V \quad (2.57)$$

where I is the current in Amperes and V is the cell potential in Volts. Hydrogen consumed is (Faraday's Law) directly proportional to current:

$$N_{H_2} = \frac{I}{nF} \quad (2.58)$$

where N_{H_2} is in mol/s and

$$W_{H_2} = \Delta H \frac{I}{nF} \quad (2.59)$$

where

W_{H_2} = energy value of hydrogen consumed in Joules per second (Watts),

ΔH = hydrogen's higher heating value (286 kJ/mol).

It should be noted that $\Delta H/nF$ has dimension of Volts, and for $\Delta H = 286$ kJ/mol it has a value of 1.482 V, which is the so-called thermoneutral potential. By combining Equations (2.56) through (2.59), the fuel cell efficiency is

$$\eta = \frac{V}{1.482} \quad (2.60)$$

Explicitly, the PEMFC efficiency is simply directly proportional to cell potential. Once the polarization curve of the fuel cell has been recorded, the fuel cell efficiency has also been obtained by using Equation (2.60).

CHAPTER III

NAFION[®] MEMBRANES:

PROPERTIES AND APPLICATIONS

3.1 Introduction

Nafion[®] is a sulfonated tetrafluoroethylene based fluoropolymer-copolymer invented by Dupont de Nemours & Co. This membrane is the first of a class of synthetic polymers with ionic properties named "ionomer". In fuel cell application, the Nafion membrane is a vital component serving as a separator to prevent mixing of fuel and air, and being an electrolyte to transport protons from the anode to the cathode. The unique properties of the Nafion membrane result from perfluorovinyl ether groups terminated with sulfonate groups onto a tetrafluoroethylene (Teflon[®]) backbone (Mauritz and Moore, 2004). Hence, the Nafion membrane exhibits the physical and chemical properties of its Teflon base material with ionic characteristics.

The excellent properties may be summarized in the followings:

1. **Chemical stability:** Nafion is extremely resistant to chemical attack, like Teflon. Only metallic alkali metals (sodium in particular) can attack Nafion directly under normal conditions of temperature and pressure.

2. Thermal resistance: Nafion has relatively high working temperature compared to many polymers. It is used in some applications at temperature up to 190°C.
3. High proton conductivity: Unlike Teflon, Nafion is highly ion-conductive and exhibits zero electronic conductivity. It functions as a cation exchange polymer due to its sulfonate groups at the polymer side chain in a swollen form.
4. Super-acid catalyst: The sulfonic acid groups attached to the Teflon backbone within Nafion function as an extremely strong proton donor due to the stabilizing effect of the large polymer matrix attached to the sulfonic acid.
5. Nafion is very selective and highly permeable to water. The sulfonic acid groups in Nafion have very high water-of-hydration, so they very efficiently absorb water. Interconnections between the sulfonic acid groups lead to very rapid transfer of water through the Nafion.

From these excellent properties, Nafion has received a considerable amount of attention as a proton conductor for the PEMFCs. In contrast, these remarkable properties are due to the strongest single bond in organic chemistry of carbon and fluorine in the polymer backbone, C-F bonds can have a bond dissociation energy up to 130 kcal/mol (O'Hagan, 2008), which higher than other carbon-halogen and even carbon-hydrogen bonds.

3.2 Applications of Fluoropolymer Materials

The existence of tetrafluoroethylene at the polymer main chains results in the mechanical and chemical strength of the membrane for many applications. The ethylene-tetrafluoroethylene (ETFE), for example, one of seven fluoropolymers generated from the invention of PTFE or the plastic more commonly known as Teflon, is very stable material, non-deformable, durable and especially fireproof. Modern establishment projects such as the Allianz arena stadium (Munich, Germany), Eden Project (Cornwall, UK) and the Water Cube (PTW Architects, Beijing, China) have contributed significantly to the dissemination of knowledge as a building material ETFE. More specifically, the ETFE is used as the material for the roof and walls of these modern projects as depicted in Figure 3.1. In many laboratories, Nafion has essentially been used as a polymer support for inorganic photocatalysts due to the mechanical strength and chemical stability.

For Nafion, alternative to the PEMFC application, this membrane has also an unrivalled memory for contortions. Such a special property has been used to design the special suit that can change its size at the different temperature. Scientist in General Motors (GM) found that this "yoga polymer" will revert to each shape at the appropriate temperature (Xie, 2010).

In this article, Nafion becomes softer as it is heated. At 140°C, it was stretched into a particular shape, which was locked in the polymer's "memory" as it cooled to 107°C and stiffened. Stretching and cooling it twice more allowed two other shapes to be memorized, so that when heated to the appropriate temperature the Nafion formed the corresponding shape.



Figure 3.1 ETFE applications; Allianz arena stadium (a), Eden Project (b) and Water cube (c).

Furthermore, Nafion's superior properties allowed for broad application. Nafion has found use in chlor-alkali production, metal-ion recovery, water electrolysis, plating, surface treatment of metals, batteries, sensors, drug release, gas drying or humidification, and super-acid catalysis for the production of fine chemicals. However various applications of Nafion are considered as well, the major boom is to use it as the proton conductor in the PEMFCs. Until now, from the late 1960s, among the various kinds of new polymer electrolyte membranes, Nafion is still being used as the benchmark membrane for PEMFC applications due to its unique and excellent properties such as high proton conductivity, chemical resistance and mechanical stability.

3.3 Early Developments of Nafion

The idea of using organic cation exchange membranes as solid electrolytes was first described by William Thomas Grubb and Lee Niedrach in 1959. NASA's interest in fuel cells as power sources for space applications gave great impetus to polymer fuel cell development with the testing of phenolic membranes (Kordesch and Simader 1996). The membranes generated power densities of 0.05 - 0.1 kW/m² and lifetimes of 300 - 1,000 h, as well as low mechanical strength. General Electric (GE) improved the power density by developing partially sulfonated poly(styrene sulfonic acid) membranes, which improved power densities to 0.4 - 0.6 kW/m².

The first PEMFC application was reported by GE as a primary power source for the GEMINI series of spacecraft during the mid-1960s (Rikukawa and Sanui, 2000). At that time, the electrolytes were based on poly(styrene sulfonic acid). Although, the fuel cell was a 1-kW power plant, extremely expensive materials were used and the fuel cells required very pure hydrogen and oxygen. Moreover, the membranes exhibited brittleness in dry state. Therefore they were later replaced with crosslinked polystyrene-divinyl benzene sulfonic acid membranes. But the membranes lacked stability and underwent degradation and suffered other problems. Consequently, the proton conductivity of this membrane was insufficient for high power density fuel cell applications (< 100 mW/cm²).

In 1966, the poly(styrene sulfonic acid) membranes were replaced by the perfluorinated ionomer (PFI) material namely Nafion. This was a real breakthrough in membrane developments for PEM fuel cells. At this early stage of development the most improved membranes showed lifetimes of up to 3,000 h at low current densities and temperatures of 50°C (Steck, 1995).

In fact, the Nafion membrane was discovered in the late 1960s by Walther Grot (DuPontTM) (Arico, Srinivasan and Antonucci, 2001). Unlike the Teflon structure, the sulfonic acid functional groups are attached. The acid molecules are fixed to the polymer and cannot leak out, but the protons of these acid groups are free to migrate through the membrane. The chemical structure of Nafion is shown in Section 2.2.2 (Figure 2.3). Nafion possessed inherent chemical, thermal, and oxidative stability and it displaced the unstable polystyrene sulfonic acid membranes. The advent of Nafion in the late 1960s gave an impetus to the PEM industry. For example, the second GE PEMFC unit using Nafion, powered the Biosatellite spacecraft in 1969.

With the commercial Nafion120, a lifetime of over 50,000h was achieved (Savadogo, 1998). Nafion120 has an equivalent repeat unit molecular weight of 1200 ($x = 6-10$ and $y = z = 1$) and a dry state thickness of 260 μm , whereas Nafion117 and Nafion115 have equivalent repeat unit molecular weights of 1100 and thicknesses in the dry state of 175 and 125 μm , respectively. The Nafion family of membranes extended the lifetime by four orders of magnitude, and soon became standard for PEMFC to this today. The Dow and Asahi Chemical companies also synthesized advanced perfluorosulfonic acid membranes with shorter side chains. These polymer membranes have higher conductivity than Nafion but there is no large-scale industrial electrochemical system using them.

3.4 Nafion Morphology

Even though the chemical structures, mechanical and chemical properties of Nafion have already been investigated, the exact study on the proton transport in the hydrated form of Nafion that directly related to the morphological changes has not been accomplished.

However, there are many different structural models available for describing the morphological change of the hydrated state of Nafion such as the polymer-bundle model (Rubatat, Rollet, Gebel and Diat, 2002) and the cylindrical water-channel model (Klaus and Chen, 2008). But the most common structural model is the cluster-network model or the Gierke's model (Gierke, Munn and Wilson, 1981). Based on the Gierke's model, the ionic clusters formed in the Nafion matrix, and suggested the formation of inverted micelles with SO_3H groups forming hydrated clusters embedded in the fluorocarbon phase with diameters of 40-50 Å. More recently, Gebel et al. proposed a conceptual description for structural evolution that depends on the water content of Nafion as depicted in Figure 3.2.

For dry Nafion, isolated spherical ionic clusters were calculated to have a 15 Å diameter and an intercluster spacing of 27 Å. This diameter is significantly smaller than the intercluster distance, which explains the low ionic conductivity observed at low water content. Absorption of water induces the formation of isolated spherical pools of water having a diameter of 20 Å with the ionic groups located at the polymer/water interface. The interaggregate distance is ~ 30 Å indicating that the spherical water pools are still isolated as evidenced by the low ionic conductivity of the membrane.

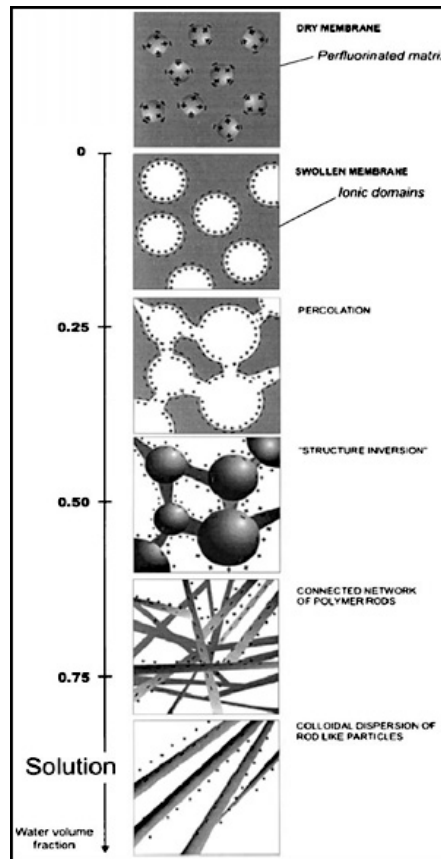


Figure 3.2 Structural evolution of Nafion depending on water content (Yang, Sui, Peckham and Holdcroft, 2008).

As the water content increases, the diameter of the cluster increases up to 40 Å while the inter-cluster distance increases only marginally. For a water volume fraction X_v larger than 0.2, a large increase in ionic conductivity is observed indicating a percolation threshold of ionic aggregates has been reached.

Between $X_v = 0.3$ and 0.5, the structure is believed to be formed of spherical ionic domains connected with cylinders of water dispersed in the polymer matrix. The ionic domain diameter increases from 40 to 50 Å, and the increase of ionic conductivity as water content increases suggest that both the connectivity and the diameter increase.

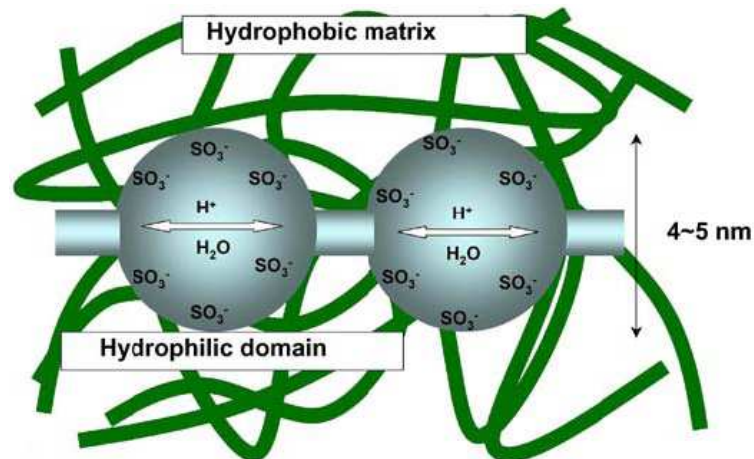


Figure 3.3 Schematic illustration of the cluster-network model of Nafion, contributed by SAXS measurements.

At X_v values larger than 0.5, an inversion of the morphology occurs and the membranes correspond to a connected network of rod-like polymer aggregates surrounded by water. Despite the fact that a spherical shape would be energetically favorable for the polymeric domains, apparently it is not possible to obtain such morphology at X_v values larger than 0.5 because the polymer volume associated with each ionic group is too large compared to the average distance between ionic groups along the polymer chain. Between $X_v = 0.5$ and 0.9, this connected rod-like network swells. The conductivity measurements indicate that the structure of the highly swollen membrane is close to the one observed for perfluorosulfonate ionomer (PFSI) solutions.

According to the membrane researches on a small angle X-ray scattering (SAXS) (Page, Landis, Phillips and Moore, 2006), the morphological model of Nafion had been performed. The scattering profiles show that there are two complex separated domains within the Nafion membrane in dry and hydrated forms: crystalline and ionic domains.

The crystalline domain composed of relatively long runs hydrophobic of PTFE segments between side chains, while the ionic domain, indicated by the ionomer peak, is the ionic aggregation from the hydrophilic sulfonic acid groups as shown in Figure 3.3. Note that the intensively details of the SAXS results, correspond to the vacuum ultraviolet (VUV) irradiations, have been discussed in Chapter V.

3.5 Degradation Mechanism of Nafion

In general, the Nafion membrane can undergo polymer degradation with and without fuel cell operation. During PEM fuel cell operation, the Nafion membrane degradation occurs regularly by the generation of a trace radical species (such as $H\bullet$ and $OH\bullet$) especially in the present of H_2 , O_2 and Pt (Yu, Sha, Liu, Merinov and Shirvanian, Article in press). The radical attack against the polymer electrolyte membrane is one of the severe problems in the PEMFC applications. And they are involved in the chemical degradation of Nafion.

In polymer science, on the other hand, the polymers can also undergo photo-degradation in normal conditions without the fuel cell operation. Such a condition that accelerates the degradation is the weather condition when expose the polymer to direct sun light for a long period of time in the surrounding air (i.e., the deformation of rubber and tire). For the Nafion membrane, the photo-degradation may be activated by UV radiation (Danilczuk, Perkowski and Schlick, 2010). Although the membrane is the one of the most chemical-resistant polymer, storing the membrane in different weather conditions may encounter the membrane degradation. Subsequently, a similar to most natural and synthetic material, the membrane reacts with some reactive species in air and being the organic contaminants on the membrane.

A good representative photo-degradation mechanism is, for example, the deterioration of fluorinated ethylene propylene (FEP) in the terrestrial orbit. This polymer is used as the thermal blankets to provide protection from direct solar heat in space projects. Spacecraft in low orbit, however, are usually subjected to significant levels of high energy radiation, including UV radiation.

In low earth orbit region, the incident UV wavelength extends below 290 nm to the VUV region, where the Lyman- α emissions of atomic hydrogen occur at 121 nm. It was reported that exposure of FEP to UV radiations resulted in the formation of three radical species (Rasoul, Hill, George and O'Donnell, 1998). When these species were exposed to oxygen in surrounding air, peroxy free radicals ($\text{POO} \cdot$) were formed.

Because polymer is the large organic molecules, which is composed of long molecular chains in the polymer matrix, no wonder if these macromolecules are sensitive against excessive energy transfer. Thus the extremely long molecular chains can be broken easily receiving a quantum of energy above a certain level. The minimum energy to open the covalent bond of the main carbon chain is in the range of 5-10 eV (Czvikovszky, 2004), which is also in the UV region. Furthermore, gamma ray or electron beams representing a high risk of degradation to all kind of polymers.

In general, polymers may undergo photo-oxidation and subsequently photo-degradation. These processes consist of several steps of: chain initiation, chain propagation, chain branching and chain termination. The initial step is the light absorption which leads to the polymer alkyl radical ($\text{P} \cdot$) initiation,



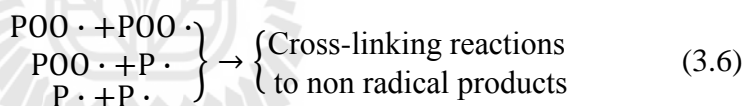
where Δ = incoming photons during irradiation, and P represents the polymers.

The next step is the chain propagation. The free radical reacts with oxygen to produce polymer peroxy radical ($\text{POO}\cdot$), followed by the formation of polymer oxy radical ($\text{PO}\cdot$) and hydroxyl radical ($\text{HO}\cdot$) by photolysis in the photo blanching process:



where POOH = polymer hydroperoxide

The polymer could either reach the final step of the chain termination in Equation (3.6) or continually undergo the polymer chain scission as described in Equations (3.4) and (3.5).



It is important to note that the hydroxyl radicals can react with other chains in the polymer. This chain reaction is known to be the reactive radicals attack in polymers, resulting in chemical changes and also induces the polymer degradation.

For perfluorosulfonic acid polymer (PFSA) such as Nafion and (FEP), the photo-degradation takes place in both the polymer backbone (main chain) and side chain. Consequently, the mechanical strength and the ionic conductivity of Nafion have been decreased with radiation doses. In fact, the PTFE main chains of Nafion can undergo degradation when subjected to radiation. The possible primary event in the radiation damage of the main chains of Nafion could either be fluorine removal or chain scission as shown in Figure 3.4 (Wheeler and Pepper, 1982).

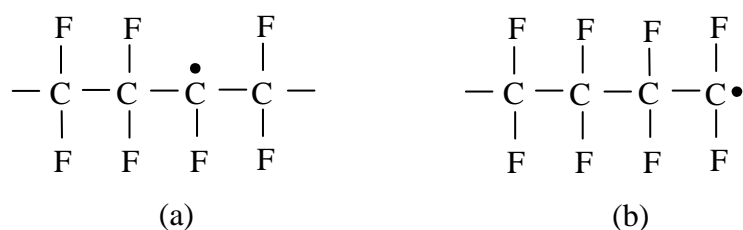


Figure 3.4 Free radicals formation in PTFE could either be fluorine removal (a) or chain scission (b).

These free radicals are sensitive to surrounding active elements in air such as oxygen and hydrogen to form an acid fluoride ($-\text{CF}_2\text{C}(\text{O})\text{F}$) and transform to ($-\text{CF}_2\text{COOH}$) in the higher degree of humidity, as described in the chain propagation process in Equation (3.3).

However, the carbon double bond formation can sometime occurred in the final form of the polymer, instead of the incorporation of the surrounding contaminants. Nevertheless, these free radicals formations cause the chemical change and degrade the polymer properties.

For the vinyl group at the side chain, the polymer side chain shows additional decomposition effects: the concentrations of sulfur and oxygen decrease. The decreases in oxygen and sulfur concentrations are faster than the decomposition of the main chain polymer (Schulze, Lorenz, Wagner and Gülzow, 1999). The degraded Nafion membrane exhibits low proton conductivity and has more brittleness due to the decrease in the mechanical strength. Since the ability of the proton conduction of Nafion depends directly on the surface state, changing in the surface state resulting in the changes in its proton conductivity and also the performance of the PEMFCs.

Obviously, the surface characterization techniques play a crucial role in solving the membrane problems and also the development of the membranes for PEMFCs. The studies of the surface structural changes of the Nafion membranes can be performed by using various characterization techniques. The basic concepts of these characterizations have been described in the next chapter.



CHAPTER IV

RESEARCH METHODOLOGY

Since the proton conductivity of the Nafion membrane directly depends on the surface state (i.e., surface roughness, catalyst distribution on the membrane-electrodes interface and surface active areas for the PEMFC electrochemical reaction), changing in the surface state inevitably affects the proton conductivity of the membrane, mechanical strength, chemical stability and also the PEMFCs performance. Obviously, the surface characterization techniques with the combination of the fuel cell performance tests play a crucial role for the studies of the membrane conductivity and durability and fuel cell performance.

In this thesis, for the primary process, the membrane must be cleaned by chemicals in order to reduce the surface impurity of some precursor species which are assigned to be the contaminants on the polymer film. After preparations, the membranes have been treated by the VUV synchrotron radiations in order to modify the surface of the membranes and eliminate the remaining contaminants. Since the VUV modification causes the modification to a depth of typically 5-10 nm, the irradiated membranes have consequently been examined by using powerful surface characterization techniques of photoemission spectroscopy (PES), atomic force microscopy (AFM), mass spectrometry and small angle X-ray scattering (SAXS). The performance of the PEMFCs, using the irradiated membranes, has also been investigated by the PEM fuel cell performance tests.

4.1 Sample Preparations

The pretreatment of the Nafion membranes was done by the chemical cleaning method. Due to the sturdy chemical structure of Nafion, this polymer has a strong acid resistance and withstand to these chemicals. The most effective cleaning method is therefore to boil the membrane in strong acid. More specifically, sulfuric acid (H_2SO_4) has been used for this propose. This process is sometime called "sulfonation". The sulfonated Nafion has an increasing in the acid groups and able to conduct more protons.

After the membrane pretreatment, the sulfur concentration on the surface of Nafion has been increased and the organic and metallic impurities have been eliminated. It should be noted that there are at least four steps of the typical chemical cleaning processes as shown in the following steps:

1. Boiled in 5% of hydrogenperoxide solution (H_2O_2) at 80°C for 60 minutes to clean the membrane surface from organic contaminations.
2. Boiled in deionized (DI) water at 80°C for 60 minutes to remove H_2O_2 .
3. Membrane sulfonation by boiling Nafion in 10% of H_2SO_4 at 80°C for 60 minutes to remove metallic impurities and increase the sulfur concentration on the membrane surface.
4. Boiled in deionized water again at 80°C for 60 minutes to remove acid.

The membranes before and after pretreatment are shown in Figure 4.1. As described earlier, the membranes had been stored in normal condition (exposure Nafion to the UV radiation in the surrounding air for a long period of time (~2 years) in different weather conditions) before chemically pretreated.



Figure 4.1 The degraded Nafion membrane before pretreatment (a) and the Nafion membrane after chemical pretreatment (b).

According to the membrane degradation in Section 3.4, the Nafion membranes have undergone photo-degradation. Over time, the organic impurities were built up on the Nafion membrane causing the original color to gradually change from translucent to yellow, brown, then even black. This mechanism is typically called the yellowish discoloration of polymers. After chemical pretreatment, the brownish color is vanished and the membranes became nearly transparent. The pretreated membranes have then been cut into three sizes of square shape ($3 \times 3 \text{ cm}^2$ for the fuel cell performance test and $0.8 \times 0.8 \text{ cm}^2$ for the PES, mass spectrometry and Ar^+ sputtering and $1 \times 2 \text{ cm}^2$ for SAXS measurements). Before VUV irradiations, these membranes are dried in vacuum with the base pressure of $\sim 10^{-3}$ mbar for 24 hour.

4.2 VUV Irradiations

It has been generally accepted that that VUV radiations can be introduced for the structural modification of polymers and even semiconductors. Using VUV as an excitation source is an essential method for photolithography.

The development of 157 nm (7.9 eV) lithography has offered significant challenges with the materials involved in the technology (Lee et al., 2005).

Because the chemical bonds in polymers can probably be broken by UV radiation, these chemical changes depend on the irradiation doses on the polymers, or the "fluence" of the UV irradiation. The UV radiation fluence is defined by the multiplication of the number of photons impacting to the unit area of the sample and the irradiation time.

$$F = DT \quad (4.1)$$

where F = radiation fluence (photons/cm²), D = photon current density = number of incident photons per area in 1 second (cm⁻²) and T = irradiation time (s).

In addition to examine the chemical changes during VUV irradiation without any oxygen reactions, the experiment has been performed in an ultra high vacuum (UHV) chamber. This method is accomplished by connecting the pumping and sample load-lock systems to the irradiation chamber.

4.3 Photoemission Spectroscopy

The most straightforward method to investigate electronic properties is to remove the electrons from the solid, and to measure them far from the interacting system. This is the general idea of a photoemission spectroscopy (PES). In general, there are many applications implicated with the PES spectra in various fields such as semiconductors engineering, surface chemistry and physics. Although the photoemission phenomenon was discovered by Hertz since 1887, the PES technique is still be largely used.

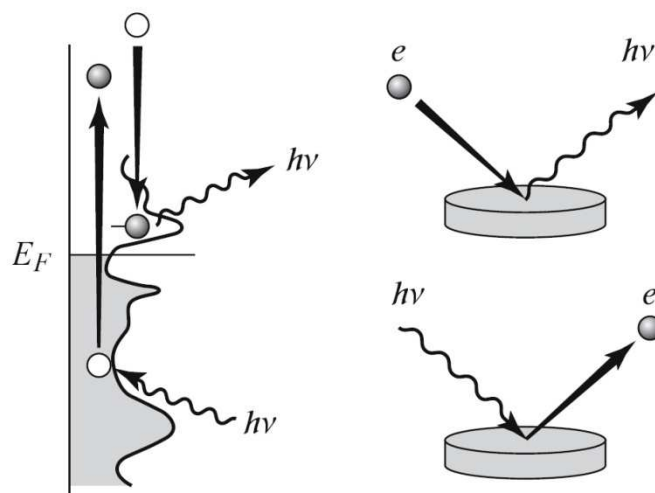


Figure 4.2 Schematic view of the photoemission (bottom) and inverse photoemission (top) processes (Grioni, 2006).

The versatile method of angle resolved photoemission spectroscopy (ARPES), for example, with the contribution of modern synchrotron technology and a new generation of electron analyzers reveals a two-dimensional "ARPES intensity map" of the measured intensity. This representation is quite appealing because it is directly comparable with the calculated band structure (Meevasana et al., 2011). In this perspective, only a very brief account of traditional aspects of PES for the Nafion polymer membranes is considered thereby probing the structural changes on their surface. In contrast, the PES is a photon in-electron out experiment.

In Figure 4.2, the interaction of a monochromatic beam of UV or soft X-ray with a sample generates photoelectrons with a broad distribution of emission angles and kinetic energies. The target may be indifferently a solid, a liquid or a gas, but in the following the more common case of a solid is considered. The emitted electrons are then collected over a broad (PES) or a narrow (ARPES) acceptance angle.

The subsequent measurement of the distribution of kinetic energies, typically performed by an electrostatic analyzer, yields a spectrum or energy distribution curve (EDC). The EDC represents the number of photoelectrons measured as a function of kinetic energy. It is important to note that there are two available photon sources to perform energetic photons for the PES measurements (a laboratory source and a synchrotron radiation source). For the investigation of core-level states, called X-ray photoemission spectroscopy (XPS), the typical laboratory sources are X-ray source from anode materials of aluminium (Al- $K_{\alpha 1,2}$: 1486.6 eV) and magnesium (Mg- $K_{\alpha 1,2}$: 1253.6 eV). For the investigation of valence band states, called ultraviolet photoemission spectroscopy (UPS), the typical laboratory VUV sources are rare gases like helium (He I $_{\alpha}$: 21.23 eV and He II $_{\alpha}$:40.82 eV).

Presently, the use of synchrotron radiation for the PES has become increasingly important because it allows measurements that cannot be performed by usual VUV or X-ray sources in the laboratory. Many dedicated synchrotron facilities have been installed worldwide, e.g. BESSY in Germany (Berlin), Maxlab in Sweden (Lund), the Advanced Light Source in the USA (Berkeley), Australian Synchrotron in Melbourne, Spring-8 in Japan (Osaka) and Siam Photon Light Research Institute (SLRI) in Thailand, among many others appropriate for PES experiments.

The main difference of the synchrotron compared to laboratory sources is that the photon energy can be selected by use of a monochromator from a continuous spectrum over a wide energy range. This advantage offers new technique of the dynamic photoemission spectroscopy. For example, the Nafion surface can simultaneously be characterized with the synchronized adjustable photon fluence of the VUV treatments.

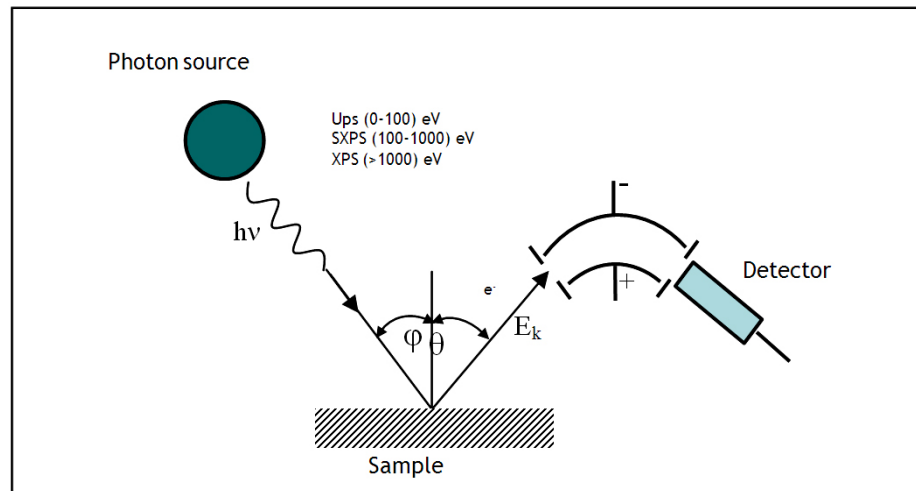


Figure 4.3 A modern PES experiment. The kinetic energy E_k of the photoelectrons can be analyzed by use of electrostatic analyzers. The whole setup is evacuated to UHV, typically $P \sim 10^{-10}$ mbar (Hüfner, 2003).

The PES is thus a powerful tool for surface characterization in different scientific researches. With the concept of photon introduced by Einstein in 1905, the basic principle of the PES is based on one of his four famous publications, so called "the photoelectric effect". The principle of a modern PES is illustrated in Figure 4.3.

When a photon is absorbed, its energy is transferred to an electron, which jumps from its initial state at energy E_i to an excited state. If the photon is sufficiently energetic, the final state lies above the vacuum level and the photoelectron can escape from the solid. Energy conservation then determines the photoelectron kinetic energy at the surface of the sample E'_k

$$E'_k = h\nu - \phi_s + E_i, \quad (4.2)$$

where $h\nu$ is the photon energy and ϕ_s is the work function of the sample.

Because of this energy conservation, structures in the energy distribution of the photoelectrons reproduce the structures in the occupied density of states (DOS). In fact, PES spectra are being invisible in the unoccupied states region, which can be measured by an absorption technique such as X-ray absorption (XAS) or by inverse photoemission (IPES) (Hüfner, 2003). For PES measurement, it is important to employ the binding energy (E_B) of an energy level, which is generally referred to the Fermi level rather than the initial-state energy E_i . The energy conservation of PES is then expressed in term of this binding energy

$$E'_k = h\nu - \phi_s - |E_B|. \quad (4.3)$$

For the case of a metallic sample in a metallic spectrometer, the energy levels and kinetic energies are shown in Figure 4.4. Thermodynamic equilibrium between sample and analyzer requires that their electron chemical potentials or Fermi levels be equal as shown. In a metal at absolute zero, the Fermi level being the highest occupied level. And the work function ϕ_s is the energy separation between the vacuum level and the Fermi level. When the sample is connected to the analyzer, the respective vacuum levels for sample and analyzer need not be equal. Thus, electrons that travel from the surface of the sample to the analyzer feel an accelerating or retarding force with the potential equal to $\phi_s - \phi$, where ϕ is the analyzer work function. For this reason, an initial kinetic energy E'_k at the surface of the sample can be expressed in term of the electron kinetic energy E_k in the analyzer,

$$E'_k = E_k + \phi - \phi_s. \quad (4.4)$$

Consequently, the binding energies in a metallic solid can be expressed in term of the work function of analyzer

$$|E_B| = h\nu - E_k - \phi \quad (4.5)$$

4.4 Computational Calculations

Because the quantum n-body problem cannot be solved analytically, the interpretation of atomic and molecular properties is obtainable by means of computer approximations. This application is called the computational chemistry. For example, whenever the PES provides the experimental probes of the valence spectra of molecules, polymers and solids, theoretical electronic structure calculations are often compared to the PES spectra in both to understand the features observed and to test the calculations.

Computational chemistry is in fact a branch of chemistry that uses principles of computer science to facilitate the calculations. Many powerful computational programs available this day are included; GAMESS (General Atomic and Molecular Electronic Structure), CADPAC (Cambridge Analytical Derivatives Package), AMBER (Assisted Model Building with Energy Refinement) and GAUSSIAN. They have been conducted for these objectives. For more information, recent quantum chemistry programs in both academic and commercial available have been proposed with many different algorithms. (Young, 2001). Most of the computer programs include the Hartree-Fock (HF), post-Hartree-Fock, density functional theory (DFT), molecular mechanics and semi-empirical quantum modeling methods. Recently, the GAUSSIAN is the one of the most significant commercial software available in the computational chemistry. The program containing the wide variety codes of *ab initio*, density functional theory (DFT), semiempirical and molecular mechanic (MM) simulations for chemists, chemical engineers, biochemists, physicists and other scientists worldwide. (Atkins and Friedman, 2005).

In this thesis, the GAUSSIAN software has been used to calculate the electronic structure of Nafion via the density functional theory (DFT) calculations, in order to testify the calculations with their photoemission spectra from the PES experiments. The details of the Gaussian calculations and comparisons will be discussed in Chapter V.

4.4.1 Density functional theory

Density functional theory (DFT) is a quantum mechanical modeling method used in physics and chemistry to calculate the electronic structure (principally the ground state) of many-body systems, in particular atoms, molecules and the condensed phases. It has been very popular for calculation in solid state physics since the 1970s. However, the DFT was not considered accurate enough for calculations in quantum chemistry until the 1990s, when the approximations used in the theory were greatly refined to be a better model with the contributions of the exchange and correlation interactions.

4.4.1.1 Derivation and formalism

The popularity of the DFT calculation arose from the difficulties to solve the Schrodinger equation for many-body systems, where the electron-electron interaction energy $U(\vec{r}_i, \vec{r}_j)$ must be added, as shown in Equation (4.6).

$$\left[-\frac{\hbar^2}{2m} \sum_{i=1}^N \nabla_i^2 + \sum_{i=1}^N V(\vec{r}_i) + \sum_{i=1}^N \sum_{j<i}^N U(\vec{r}_i, \vec{r}_j) \right] \psi = E\psi, \quad (4.6)$$

where m is the electron mass. The three terms in the brackets define, in order, the kinetic energy of each electron, the interaction energy between each electron and the collection of atomic nuclei, and the interaction energy between different electrons.

The Hamiltonian ψ is set to be the electronic wave function, which is a function of each of the spatial coordinates for each of the N electrons, $\psi = \psi(\vec{r}_1, \dots, \vec{r}_N)$, and E is the ground-state energy of the electrons. The ground-state energy is independent of time. This is the time-independent Schrödinger equation.

Although the electron wave function is a function of each of the coordinates of all N electrons, it is possible to approximate ψ as a product of individual electron wave functions, $\psi = \psi(\vec{r}_1)\psi(\vec{r}_2), \dots, \psi(\vec{r}_N)$. In the case of a single molecule of CO_2 , for example, the requirement of the full wave function is a 66-dimensional function (3 dimensions for each of the 22 electrons). On the other hand, a nanocluster of 100 Pt atoms, the full wave function requires more the 23,000 dimensions! These numbers should begin to present an idea about why solving the Schrodinger equation for practical materials has occupied many brilliant minds for a good fraction of a century.

In more complex systems, the wave function for any particular set of coordinates cannot directly be obtained. The quantity that can, in principle, be measured is the probability that the N electrons are at a particular set of coordinates, $\vec{r}_1, \dots, \vec{r}_N$. This probability is equal to $\psi^*(\vec{r}_1, \dots, \vec{r}_N)\psi(\vec{r}_1, \dots, \vec{r}_N)$. A further point to notice is that the electron labeling in the material, i.e., electron #1, electron #2, ..., is not necessary.

Moreover, even if the labels have been considered, it is not easy to assign these labels. This means that the quantity of physical interest is really the probability of a set of N electrons in any order with coordinates $\vec{r}_1, \dots, \vec{r}_N$. A closely related quantity is the density of electrons at a particular position in space, $n(\vec{r})$. This can be written in terms of the individual electron wave functions as

$$n(\vec{r}) = 2 \sum_i \psi_i^*(\vec{r})\psi_i(\vec{r}) . \quad (4.7)$$

The term inside the summation is the probability that an electron in individual wave function $\psi_i(\vec{r})$ is located at position \vec{r} . The factor of 2 appears because electrons have spin and the Pauli exclusion principle states that each individual electron wave function can be occupied by two separate electrons with the different spins. The point of this discussion is that the electron density, $n(\vec{r})$, which is a function of only three coordinates, contains a great amount of the information that is actually physically observable from the full wave function solution to the Schrodinger equation, which is a function of $3N$ coordinates.

The concepts of the reduction of $3N$ coordinates to only 3 coordinates by means of the electron density based on two fundamental mathematical theorems proved by Kohn and Hohenberg and the derivation of a set of equations by Kohn and Sham in the mid 1960s. The first theorem demonstrates that "the ground state energy from Schrodinger equation is a unique functional of the electron density". In particular, there exists a one-to-one mapping between the ground state wave function and the ground state electron density. Thus, the ground state energy E can be expressed in term of the function of electron density

$$E = E[n(\vec{r})] . \quad (4.8)$$

The Schrodinger equation can be solved, for the ground state energy, by finding a function of three spatial variables of the electron density rather than a function of $3N$ variables of the wave function. Therefore, for one unit of molecule of Nafion that contains C, F, O, S and H (> 65 atoms), the theorem reduces the problem from 1500 dimensions to a problem with just 3 dimensions.

Unfortunately, although the first Hohenberg-Kohn theorem rigorously proves a functional of the electron density that can be used to solve the Schrodinger equation, the theorem states nothing about what the functional actually is. The second Hohenberg-Kohn theorem defines an important property of the functional states that "the electron density that minimizes the energy of the overall functional is the true electron density corresponding to the full solution of the Schrodinger equation". If the "true" functional form are obtained, the electron density can be varied until the energy from the functional is minimized, giving a prescription for finding the relevant electron density. This variational principle is used in practice with approximate forms of the functional.

A useful way to describe the Hohenberg-Kohn theorem is to consider the functional in terms of the single-electron wave functions, $\psi_i(\vec{r})$. Because the wave functions collectively define the electron density, $n(\vec{r})$, as shown in Equation (4.7). Thus, the energy functional can be written as

$$E[\{\psi_i\}] = E_{\text{known}}[\{\psi_i\}] + E_{\text{XC}}[\{\psi_i\}], \quad (4.9)$$

where the $E_{\text{known}}[\{\psi_i\}]$ terms include four contributions:

$$E_{\text{known}}[\{\psi_i\}] = -\frac{\hbar^2}{m} \sum_i \int \psi_i^* \nabla^2 \psi_i d^3r + \int V(\vec{r})n(\vec{r})d^3r + \frac{e^2}{2} \iint n(\vec{r})n(\vec{r}')d^3rd^3r' + E_{\text{ion}} \quad (4.10)$$

The terms on the right are, in order, the electron kinetic energies, the Coulomb interactions between the electrons and the nuclei, the Coulomb interactions between pairs of electrons, and the Coulomb interactions between pairs of nuclei.

The term in the complete energy functional, $E_{XC}[\{\psi_i\}]$, is the exchange-correlation functional, and it is defined to include all the quantum mechanical effects that are not included in the "known" terms.

To solve the minimum energy from this equation, the task of finding the corrected electron density has been expressed in terms of a set of equations that involves only a single electron. The Kohn-Sham equations have the form

$$\left[-\frac{\hbar^2}{2m} \nabla^2 + V(\vec{r}) + V_H(\vec{r}) + V_{XC}(\vec{r}) \right] \psi_i(\vec{r}) = \varepsilon_i \psi_i(\vec{r}) \quad (4.11)$$

By comparing with Equation (4.6), the Kohn-Sham equations are missing the summations because the solutions of the Kohn-Sham equations are single-electron wave functions that depend on only three spatial variables, $\psi_i(\vec{r})$. On the left-hand side of the Kohn-Sham equations there are three potentials, V , V_H and V_{XC} . The first of these also appeared in the full Schrodinger equation and in the "known" part of the total energy functional given in Equation (4.10). This potential defines the interaction between an electron and the collection of atomic nuclei. The second is called the Hartree potential and is defined by

$$V_H(\vec{r}) = \frac{e^2}{2} \int \frac{n(\vec{r}')}{|\vec{r} - \vec{r}'|} d^3\vec{r}' . \quad (4.12)$$

This potential describes the Coulomb repulsion between the electron being considered in one of the Kohn-Sham equations and the total electron density defined by all electrons in the problem.

The last potential in the Kohn-Sham equation, V_{XC} , defines exchange and correlation contributions to the single electron equations. This exchange-correlation potential can formally be defined as a "functional derivative" of the exchange-correlation energy and includes all the many-particle interactions:

$$V_{XC}(\vec{r}) = \frac{\delta E_{XC}(\vec{r})}{\delta n(\vec{r})} \quad (4.13)$$

Because V_H , and V_{XC} depend on $n(\vec{r})$, which depend on $\psi_i(\vec{r})$, which in turn depend on $V(\vec{r}), V_H(\vec{r}), V_{XC}(\vec{r})$, To solve the Kohn-Sham equations, the Hartree potential must be defined, and to define the Hartree potential we need to know the electron density. But to find the electron density, we must know the single-electron wave functions, and to know these wave functions we must solve the Kohn-Sham equations. To break this circle, the problem is usually treated in an iterative way as outlined in the following algorithm:

1. Define an initial, trial electron density, $n(\vec{r})$.
2. Solve the Kohn-Sham equations defined using the trial electron density to find the single-particle wave functions, $\psi_i(\vec{r})$.
3. Calculate the electron density defined by the Kohn-Sham single particle wave functions from step 2, $n_{KS}(\vec{r}) = 2 \sum_i \psi_i^*(\vec{r})\psi_i(\vec{r})$
4. Compare the calculated electron density, $n_{KS}(\vec{r})$, with the electron density used in solving the Kohn-Sham equations, $n(\vec{r})$. If the two densities are similar, then this is the ground-state electron density, and it can be used to compute the total energy. If the two densities are different, then the trial electron density must be updated in some way. Once this is done, the process begins again from step 2. This self-consistent process will be iterated and calculated by using the computational software. However, the most important part of this process is to define the sufficient exchange-correlation term that is very difficult and also known to be the challenging procedure in the DFT calculations where the exact functional for exchange and correlation are not known except for the free electron gas.

4.4.1.2 Exchange-correlation functional

To solve the Kohn-Sham equations, the exchange-correlation functional must be satisfied. Although this model has to be of limited value in any real material, the uniform electron gas provides a practical way to use the Kohn-Sham equations. The exchange-correlation potential at each position is set to be the known exchange-correlation potential from the uniform electron gas at the electron density observed at that position. This approximation uses only the local density to define the approximate exchange-correlation functional and it is so called the local density approximation (LDA). In the LDA, the local exchange-correlation potential is defined as the exchange potential for the spatially uniform electron gas with the same density as the local electron density:

$$V_{XC}^{LDA}(\vec{r}) = V_{XC}^{\text{electron gas}}[n(\vec{r})] \quad (4.14)$$

The LDA results do not exactly solve the true Schrodinger equation because the electron density functional from the uniform electron gas model is not the true exchange-correlation functional. Explicitly, the development of functionals that more faithfully represent nature remains one of the most important areas of active research in the quantum chemistry community.

Further approximation is a general gradient approximation (GGA), which is the one of the important known classes of functional beyond the LDA. The GGA functional uses information of the local electron density and the local gradient in the electron density. The functional is expressed in terms of the local electron density and the gradient in the electron density:

$$V_{XC}^{GGA}(\vec{r}) = V_{XC}^{\text{electron gas}}[n(\vec{r}), \nabla n(\vec{r})] \quad (4.15)$$

In addition, it is possible to treat the exchange part in the DFT calculations by using spatially localized basis functions called "hybrid" functionals. The functionals combine the exact results for the exchange part of the functional and the approximations for the correlation part. Thus, the exact exchange energy, which can be expressed in terms of the Kohn-Sham orbitals, is expressed as

$$E^{\text{exchange}}(\vec{r}) = \frac{1}{2n(\vec{r})} \int d^3\vec{r}' \frac{|\sum_{\text{occupied state}} \varphi^*(\vec{r}')\varphi(\vec{r})|}{|\vec{r} - \vec{r}'|}. \quad (4.16)$$

One of the most common hybrid functionals in the DFT calculation is the B3LYP functional. The character "B" stands for Becke, who worked on the exchange part of the problem, while the "LYP" stands for Lee, Yang, and Parr, who developed the correlation part of the functional, and the digit 3 describes the particular way that the results are interweave together. The B3LYP exchange-correlation functional can be expressed as:

$$V_{\text{XC}}^{\text{B3LYP}} = V_{\text{XC}}^{\text{LDA}} + a_1(E^{\text{exchange}} - V_{\text{X}}^{\text{LDA}}) + a_2(V_{\text{X}}^{\text{GGA}} - V_{\text{X}}^{\text{LDA}}) + a_3(V_{\text{C}}^{\text{GGA}} - V_{\text{C}}^{\text{LDA}}), \quad (4.17)$$

where $a_1 = 0.20$, $a_2 = 0.72$, $a_3 = 0.81$ are the empirical parameters determined by fitting the predicted values to be a set of atomization energies, ionization potentials, proton affinities and total atomic energies; (Becke, 1993). $V_{\text{X}}^{\text{GGA}}$ is the generalized gradient approximation: the Becke 88 exchange functional (Becke, 1998), and $V_{\text{C}}^{\text{GGA}}$ is the correlation functional of Lee, Yang and Parr (Lee, Yang, and Parr, 1988).

4.4.2 Gaussian computational programs

Since the derivation of the DFT calculations described above can be solved by iterations, the computer software named Gaussian03W are employed in this thesis. Generally, this program includes various algorithms to calculate the physical and chemical phenomena such as the electron ground state energy, structures and molecular orbitals. The DFT is also included in this software. Moreover, there is additional software to simplify the computer codes named GaussView. And the data collecting program to summarize the ground state energy in terms of the density of state named GaussSum. The DFT calculations will be discussed in Chapter V.

4.5 Mass Spectrometry

Mass spectrometry methods have experienced a steadily increasing use in polymer analyses due to their high sensitivity ($<10^{-15}$ mol suffice for analysis), selectivity (minor components can be analyzed within a mixture), specificity (exact mass and fragmentation patterns serve as particularly specific compositional characteristics), and speed (data acquisition possible within seconds).

Mass spectral analyses involve the formation of gaseous ions from an analyte (M) and subsequent measurement of the mass-to-charge ratio (m/z) of these ions. Depending on the ionization method used, the sample is converted to molecular or quasi-molecular ions and their fragments. The mass spectrometer separates the ions generated upon ionization according to the mass-to-charge ratio (or a related property) to give a graph of ion abundance of m/z . The exact m/z value of the molecular or quasi-molecular ion reveals the ion's elemental composition and allows for the compositional analysis of the sample under study.

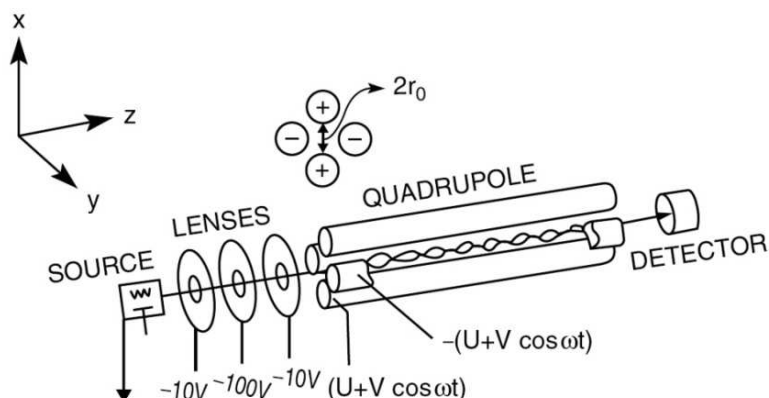


Figure 4.5 A simple quadrupole mass spectrometer consisting of an ion source, focusing lenses, a quadrupole mass filter, and an ion detector (Montaudo, and Lattimer, 2002).

4.5.1 Ionization methods

In general, there are three major preparation methods of gaseous ions. (i) Volatile materials are generally ionized by interaction of their vapors with electrons, ions, or strong electric fields. (ii) Strong electric fields can also ionize nonvolatile materials. In addition, ions from nonvolatile and thermally labile compounds can be desorbed into the gas phase via bombardment of the appropriately prepared sample with fast atoms, ions, or laser photons and via rapid heating. (iii) Alternatively, liquid solutions of the analyte may directly be converted to gas phase ions via spray techniques. Method (i) can be applied only to monomers and low-mass oligomers or in conjunction with degradation methods (principally pyrolysis). Methods (ii) and (iii), on the other hand, are amenable to intact polymers. For the Nafion polymer case, the sufficient ionization method is to use an energetic ion of an argon gas and an even intense synchrotron light. This technique was applied to the surface modification of Nafion (Ramdutt et al., 2007).

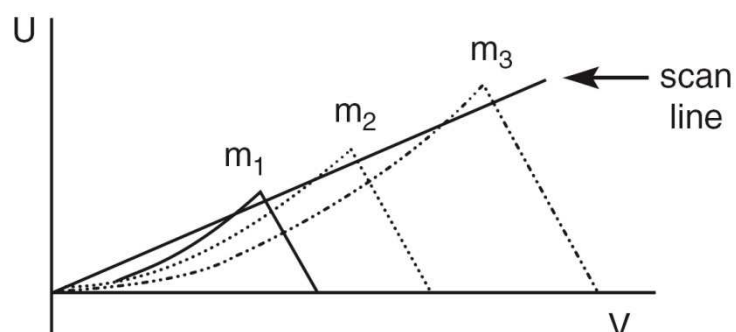


Figure 4.6 Stability conditions, expressed in terms of U vs. V plots, for three ions with masses $m_1 < m_2 < m_3$.

4.5.2 Quadrupole mass analyzers

Quadrupole mass analyzers in the mass spectrometry consist of four parallel circular or hyperbolic rods, shown in Figure 4.5. Each pairs of opposite rods are electrically connected and supplied voltages of the same magnitude but different polarity. The voltage applied to each pair consists of a direct current (DC), U , and a radiofrequency (rf) component, $V\cos\omega t$. Typical values are several hundred volts for U , several thousand volts for V , and megahertz for ω . Since the total potential of each rod is $+(U + V\cos\omega t)$ or $-(U + V\cos\omega t)$, the rf field periodically alternates the rods' polarity.

Ions (e.g., Ar^+) are accelerated along the z -axis before entering the space between the quadrupole rods where they experience the combined field resulting from the rod potentials. A cation is drawn toward the negative pole and vice versa; if the rod potential changes sign before the ion discharges, the ion changes direction, thus oscillating through the rods.

Whether an ion succeeds passing through the rods or discharges on them is controlled by the DC and rf voltages, as shown in Figure 4.6 for ions of three different masses ($m_1 < m_2 < m_3$). The values of U and V leading to stable trajectories through the quadrupole lie within the area defined by the V axis and the solid lines (m_1), dotted lines (m_2), or bullet lines (m_3). The quadrupole is scanned along the scan line, i.e., with the ratio U/V kept constant; the slope of this line determines the resolution. Gradually increasing U and V successively brings ions m_1 , m_2 , and m_3 through stable trajectories. If $U = 0$, the scan line overlaps with the V axis; the resolution is zero, and all ions pass the quadrupole. The ion of mass m_2 has a stable trajectory (i.e., it can be transmitted through the quadrupole) at the U and V values lying within the dotted curve. Any other U and V values lead to unstable trajectories (i.e., to discharge at the rods).

At the end of the mass analyzer, ion detector has been connected. The detector converts ions of a given m/z value into a measurable electrical signal whose intensity is proportional to the corresponding ion current. And the mass spectra of analyzed materials can be collected and performed in the computer software.

4.6 Small Angle X-ray Scattering

Small angle X-ray scattering (SAXS) belongs to a family of X-ray scattering techniques; wide angle X-ray scattering (WAXS), middle angle X-ray scattering (MAXS), small angle X-ray scattering (SAXS), and ultra small angle X-ray scattering (USAXS), as shown in Table 4.1. This technique has extensively been used to study the structural features such as size and volume fraction and covering studies from biochemistry, biophysics and material sciences to applied and industrial research.

Table 4.1 Subareas of scattering as a function of the sample-detector distance R assuming an X-ray wavelength of $\lambda \sim 0.15\text{nm}$

Subarea	R[m]	Focus
WAXS	0.05-0.2	arrangement of chain segments
MAXS	0.2-1	liquid-crystalline structure
SAXS	1-3	nanostructure 3 nm - 50 nm
USAXS	6-15	nanostructure 15 nm - 2 μm

It is well known that the application of X-ray scattering for the study of materials, including soft matters such as polymers, plastics, foods, and pharmaceuticals, has a long tradition. Presently, the development of both powerful detectors and brilliant X-ray sources from synchrotron radiation suggest an avenue for the SAXS experiment.

A basic experimental set-up of SAXS is similar to the X-ray diffraction experiment, where the intensity of the scattered X-ray from a sample has been measured with the scattered angle. The structure of the sample can be characterized by the scattering pattern, i.e., a graph of the scattered intensity (I) and the scattering vector (q) as shown in Figure 4.7. Although the SAXS experiment is simple, the interpretation of the SAXS scattering pattern is the complicated procedure and requires mathematical simulation model.

In this thesis, however, the SAXS experiment has been conducted to examine only the structural change between the pristine membrane and the irradiated membrane. This structural change gives rough results that are sufficient for comparison.

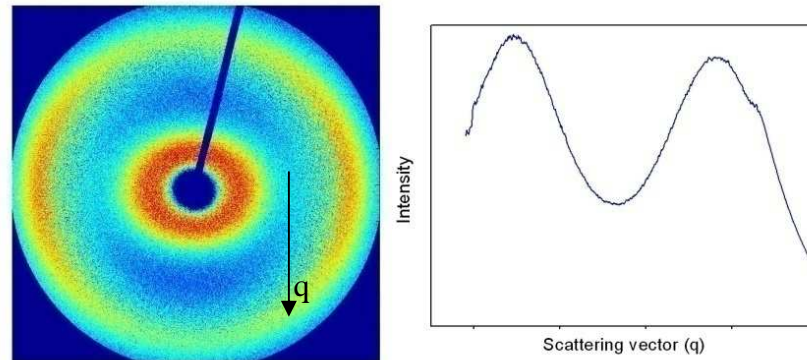


Figure 4.7 SAXS profile of a hydrated-fresh Nafion membrane extracted from the data processing program SAXSIT.

4.6.1 Theoretical basis

The theoretical basis of the SAXS experiments based on the scattering theory as described in the following subsection. It should be noted that the SAXS in this thesis is performed in order to examine the structural change in the Nafion membranes by using basic concept of the X-ray scattering without concerning further theoretical modeling and intensive morphological analysis.

4.6.1.1 Interaction between X-ray and matter

The interaction between X-ray and matter can be described using electromagnetic theory. Consider the simple case, from a classical point, of the elastic interaction of X-ray with an electron in Figure 4.8.

The electron has its own angular frequency $\omega_0 = \sqrt{k/m}$ and an X-ray beam propagates along the z direction with non-zero electric component E_x oscillating in XY plane. This electric component can be written as

$$E_x = E_0 e^{i(k_0 z - \omega t)} \quad (4.18)$$

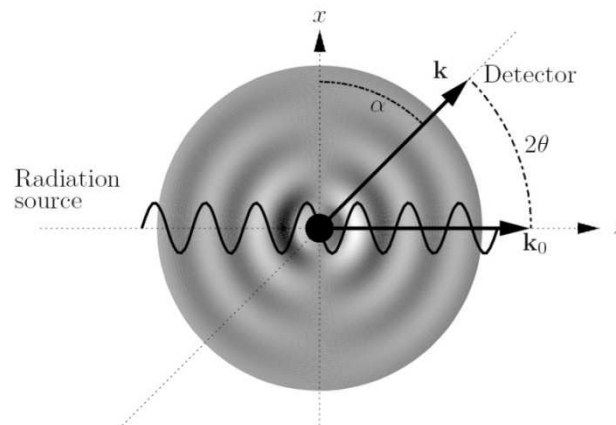


Figure 4.8 Schematic diagram of X-ray scattering with an electron.

The electric field interacting on the electron at origin is $E_x = E_0 e^{-i\omega t}$ and the corresponding electric force is $F_x = -eE_x = -eE_0 e^{-i\omega t}$. Newton equation of motion will contain the electric force and the elastic force,

$$m \frac{d^2 x}{dt^2} = -eE_0 e^{-i\omega t} - m\omega_0^2 x. \quad (4.19)$$

The general solutions of the equation of motions are

$$x(t) = -E_0 e^{-i\omega t} \frac{e}{m} \frac{1}{(\omega_0^2 - \omega^2)}, \quad (4.20)$$

$$a(t) = E_0 e^{-i\omega t} \frac{e}{m} \frac{\omega^2}{(\omega_0^2 - \omega^2)}. \quad (4.21)$$

According to the general expression of radiation field, an accelerated electron will irradiate its own electromagnetic wave. The electric component at the position \vec{r} and for a given time t can be expressed as

$$\vec{E}(\vec{r}, t) = -\frac{e}{4\pi\epsilon_0 c^2 r^3} \vec{r} \times [\vec{r} \times \vec{a}(t - r/c)]. \quad (4.22)$$

Thus, the modulus for the electrical field at the detector's position is

$$E(\vec{r}, t) = E_0 e^{-i\omega t} \frac{e^2}{4\pi\epsilon_0 m c^2} \frac{\omega^2}{(\omega_0^2 - \omega^2)} \sin \alpha \frac{e^{ik_0 r}}{r}, \quad (4.23)$$

where α is an angle between the observation direction \vec{r} and the direction of acceleration x . Obviously, the scattered electric field depends on the transverse component of acceleration. Therefore the electric field at the direction of the observer is related to the transverse acceleration ($a_T = a \sin \alpha$), as seen in the angular component in Equation (4.23). The first factor $r_0 = e^2/4\pi\epsilon_0 mc^2$ is called classical radius of the electron, $r_0 = 2.8179 \times 10^{-15}$ m. The second term $\omega^2/(\omega_0^2 - \omega^2)$ is the frequency factor. Two cases can be distinguished. If the natural frequency of the electron is much higher than the electromagnetic field frequency ($\omega_0 \gg \omega$), as occurs for visible light, the blue-shift phenomenon for blue sky has been presented. On the other hand, when $\omega_0 \ll \omega$ (as occurs essentially for X-rays), the frequency factor is equal to -1. This is the case of Thompson scattering,

$$E(\vec{r}, t) = -E_0 e^{-i\omega t} \frac{e^{ik_0 r}}{r} r_0 \sin \alpha \quad (4.24)$$

4.6.1.2 Scattering vector

Because an atom contains many electrons, it is convenient to define the average position of the electron as the arbitrary position (\vec{r}_n) and the following Thompson scattering equation (4.24) transforms to

$$E_n(\vec{r}, t) = -E_0 e^{-i\omega t} \frac{e^{ik_0 |\vec{r} - \vec{r}_n|}}{|\vec{r} - \vec{r}_n|} e^{i\vec{k}_0 \cdot \vec{r}} r_0 \sin \alpha, \quad (4.25)$$

and, for unpolarized X-rays,

$$E_n(\vec{r}, t) = -E_0 e^{-i\omega t} \frac{e^{ik_0 |\vec{r} - \vec{r}_n|}}{|\vec{r} - \vec{r}_n|} e^{i\vec{k}_0 \cdot \vec{r}} b_x, \quad (4.26)$$

where \vec{r} represents the position of the detector with respect to the origin of the reference frame.

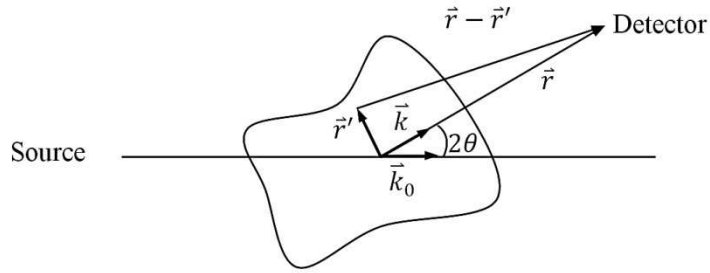


Figure 4.9 Scheme of the geometry for the calculation of the scattering at the detector in the direction of \vec{r} .

Suppose that the magnitude of the distance \vec{r}_n is lower than the distance \vec{r} , term $|\vec{r} - \vec{r}_n|$ is now simplified to be $|\vec{r} - \vec{r}_n| \approx r - \hat{r} \cdot \vec{r}_n$, \hat{r} being the unit vector of \vec{r} . The spherical wave in Equation (4.26) becomes

$$\frac{e^{ik_0|\vec{r}-\vec{r}_n|}}{|\vec{r}-\vec{r}_n|} \approx \frac{e^{ik_0r}}{r} e^{-i\vec{k}\cdot\vec{r}_n}, \quad (4.27)$$

where, $\vec{k} \equiv k_0\hat{r}$ as shown in Figure 4.9

The amplitude of electric field scattered by the electron in \vec{r}_n becomes

$$E_n(\vec{r}, t) \approx -E_0 e^{-i\omega t} \frac{e^{ik_0r}}{r} b_x e^{i\vec{q}\cdot\vec{r}_n} \equiv E(\vec{r}, t) e^{i\vec{q}\cdot\vec{r}_n}, \quad (4.28)$$

where $\vec{q} \equiv \vec{k}_0 - \vec{k}$ is the scattering vector.

For the elastic scattering, the magnitude of the incident wave number and scattered wave number is equal, $|\vec{k}_0| = |\vec{k}|$.

The magnitude of the scattering vector can be expressed in the angular dependent form.

$$\begin{aligned} q = |\vec{q}| &= (\vec{k}_0 - \vec{k})^2 = k_0^2 + k^2 - 2k_0k \cos 2\theta \\ &= 2k^2(1 - \cos 2\theta) = \frac{4\pi}{\lambda} \sin \theta. \end{aligned} \quad (4.29)$$

According to the Bragg's equation describing a scattering from a crystal lattice $\lambda = 2d \sin \theta$, where d is the spacing between the planes in the atomic lattice; the scattering vector can be expressed in term of the size of particle $q = 2\pi/d$. Note that the small q value results in a large particle size. Therefore, SAXS is the appropriate technique to study macromolecule structures such as molecular distribution, domain size and conformation of the polymer as well as ionic aggregation in Nafion.

4.6.1.3 Structural determination of Nafion by SAXS

There are several SAXS models for determining the Nafion structure. But the exact models still a controversial topic in the polymer science. Based on the most common structural model of Nafion named the cluster-network model (Gierke et al., 1981), modern computer calculations this day have been conducted to improve this model. Presently, the water-channel model reported by Klaus and Chen (Klaus et al., 2008) is the applicable simulation model for given a unified view of the structure of Nafion. The model naturally accounts for many of the outstanding properties of Nafion, in particular its high proton conductivity and water permeability. The details of this model will be discussed in Chapter V.

4.6.2 Experimental technique

The SAXS experiments in this thesis are carried out at the BL2 of the Synchrotron Light Research Institute (SLRI), shown in Figure 4.10. The main instrument in this beamline is double multilayer monochromator (DMM). This DMM has been constructed to monochromatizes, or filters, the incident polychromatic beams to have the energy of 8 keV.

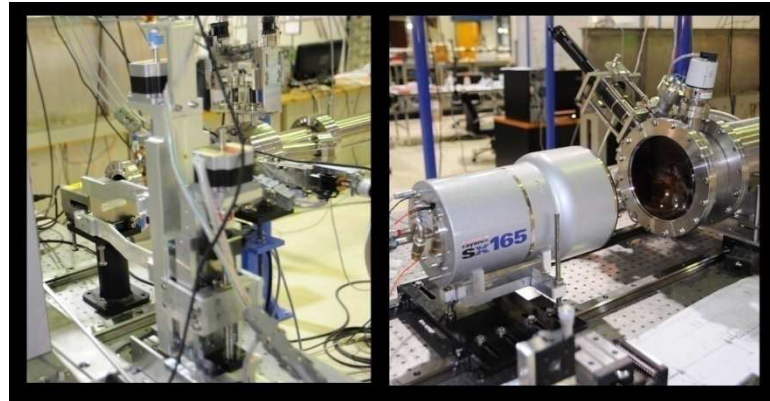


Figure 4.10 Set up instrumental component of SAXS beamline for SAXS measurement of SLRI. The left hand side illustrates the sample holder. The right hand side illustrates the SAXS detector.

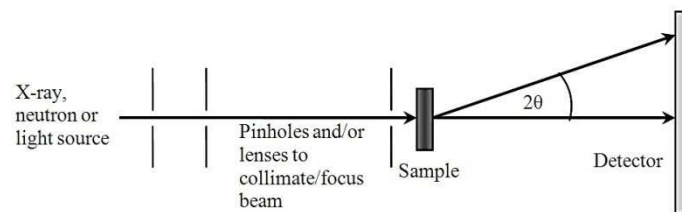


Figure 4.11 SAXS experimental setup

After monochromatization, the beam has been collimated by collimators and the beam size has been adjusted by slits. The monochromatized X-ray hits the sample and then scatters in the different directions. According to the scattering theory, the SAXS experiments generally follow the procedure as shown in Figure 4.11:

1. Irradiate a sample with a well-collimated beam of some type of radiation (X-rays, neutrons or light).
2. Measure the resulting intensity as a function of angle between the incoming beam and scattered beam.
3. Determine the structure from the observed scattering pattern.

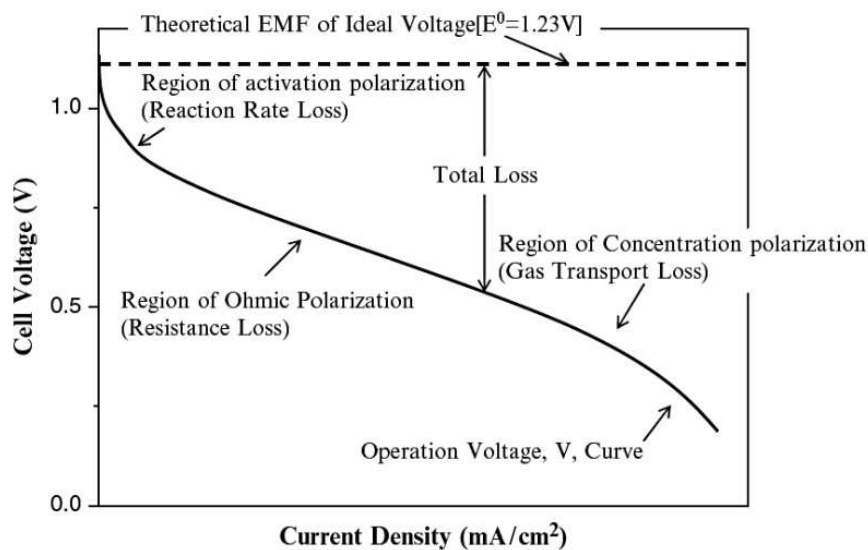


Figure 4.12 Example of a polarization curve showing the losses associated with irreversibility in a fuel cell (Yamaki, 2010).

Scattering pattern is appeared from the interference of the secondary waves that are emitted from various structures (electrons for X-rays and light, or nuclei for neutrons). For the case of the Nafion, the SAXS methods have been used to study the membrane structure and the morphological changes upon the membrane modifications by VUV irradiations. Recently, two phases separation of the membrane, described by the SAXS profile, have been reported (Klaus et al., 2008, Page et al., 2006, and Tsao, Chang, Jeng, Linc and Lin, 2005).

By using the SAXS experiment, it is expected that the structural change upon VUV treatment to the degraded Nafion membrane can be observed. Finally, by the combination method of the mass spectrometry, the effects of the VUV from the synchrotron radiation on the Nafion membrane have been verified.

4.7 Fuel Cell Performance Test

The performance of the PEMFC can be characterized by means of in situ or ex situ techniques. The most effective characterization techniques also indicate why a fuel cell performs well or poorly. One of these techniques is the current-voltage or the polarization measurement, as described in Chapter II. The electrochemical characterization technique provides an overall quantitative evaluation of fuel cell performance and fuel cell power density. The voltage output of the fuel cell for a given current density loading is obtained by connecting an electronic loader to the fuel cell during operation. The current-voltage curve from this measurement indicates the performance of the fuel cell. Figure 4.12 shows the standard J-V curve of the PEMFC. Explicitly, high-performance fuel cells will exhibit less loss and therefore a higher voltage for a given current load. The experimental of the fuel cell performance test will be discussed in Appendix C.

CHAPTER V

RESULTS AND DISCUSSION

The initiation of the measurements in this thesis is the method of searching a reliable quantity of photons that affect the membrane structure based on structural models of Nafion reported by Gierke et al. (1981) and Klaus et al. (2008). This quantity plays an important role for the vacuum ultraviolet (VUV) treatments and can be described in terms of the "photon fluence". Generally, the photon fluence is an incident photon flux integrated over exposed times. Because the effects of irradiation depend not only on the fluence but also on the structure of the irradiated materials, the morphology of the degraded Nafion membranes have essentially been elucidated before taking the VUV treatments. These VUV effects are then compared with the effects of the argon ion sputtering, the zero-order synchrotron on the Nafion surface radiation by means of mass spectrometry, in order to determine the appropriate method for the membrane modification. To examine the morphological change upon the VUV irradiations, small angle X-ray scattering (SAXS) technique has been conducted. Consequently, the improvements of the PEMFC using the degraded Nafion membranes after VUV irradiations have been investigated by using the fuel cell performance test system. Finally, the evolutions of the electronic structures of the degraded Nafion during irradiation are characterized by the photoemission spectroscopy (PES) and the computational (DFT) calculations.

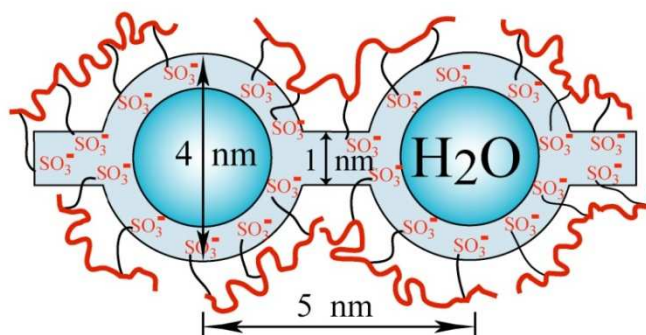


Figure 5.1 Cluster-network model for the hydrated polymer presented by Gierke et al. in 1981 and Kumar and Pineri in 1986.

5.1 Structural Model of Nafion

Over the last 30 years, numerous scattering and diffraction studies were performed and many researches on the Nafion morphology were reported. However, a universally accepted morphological model for the solid-state structure of Nafion has not been successfully discovered due to the low crystallinity and the complexity of co-organized crystalline and ionic domains in this polymer. The generally accepted picture is only an aggregation of the polar perfluoroether side chains containing sulfonic acid groups due to Coulombic interactions (called the ionic aggregation) which leads to a nanophase separated morphology. These ionic domains are distributed over the nonpolar PTFE matrix.

In addition, randomly distributed crystalline domains which have a crystal structure similar to PTFE are detected. Based on the SAXS studies of morphological model of Nafion named "the cluster-network model" reported by Gierke et al. (1981), the clusters of sulfonate terminated side chains are organized as inverted micelles in the swollen form. These micelles are interconnected by a network of short and narrow channels which allow water and ion transport, as shown in Figure 5.1.

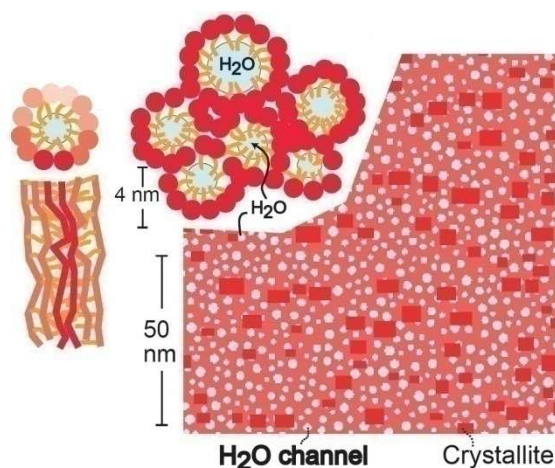


Figure 5.2 Parallel cylindrical water nanochannel model (Klaus et al., 2008).

These solvent-swollen clusters are closely related to the ionic conductivity of Nafion. The Gierke's model motivated numerous studies of the phase-segregated morphology of Nafion. However, this technique has difficulties in determining more than just the position of the Bragg or ionomer peak in the arrangement of the micelles. Thus, only information about the distance between the centers of the micelles is available, but not on the size of the micelles (Yang et al., 2008). Moreover, there are no morphological models in the past that can describe the fast diffusion of water and protons through Nafion and its persistence at low temperatures.

More recently, the structure of Nafion has been studied by using NMR and SAXS by Klaus et al. (2008). They have offered a new model providing the best explanation to date for the membrane's structure and how it functions, namely "the cylindrical water channel model". This model suggests that Nafion has a closely packed network of nanoscale cylindrical water channels running in parallel through the material. In contrast, hydrophobic (water-hating) backbone structures cluster together to form long rigid cylinders about 2.5 nanometers in diameter with the hydrophilic "hairs" to the inside of the water-filled tubes as shown in Figure 5.2.

From the water channel model, there are two phase separation in Nafion which is similar to the Gierke's cluster network model except the shape of the ionic clusters. This model described the shape of the ionic cluster as the cylindrical water channels, rather than other models such as the spheroidal (Roche, Pineri, Duplessix and Levelut, 1981; Ioselevich, Kornyshev and Steinke, 2004) or sheet-like network of water channels (Starkweather, 1982; Krivandin, Glagolev, Shatalova and Kotova, 2003). This water channel model also explain how conductivity continues even well below the freezing point of water, while other models in which the water clusters have the other shapes or connectivities did not match the measured scattering curves.

Therefore, the cylindrical water channel is expected to be the most promising morphological model of Nafion presently. For this reason, the structural parameters from this model are introduced to be the initial parameters for calculating the photon fluences on the membranes in the VUV treatments. The calculated VUV fluences can be obtained as shown in the following steps.

5.1.1 Nafion structural parameters of the cylindrical water channel model

1. The diameters of the water channels vary from 1.8 nm to 3.5 nm up to the degree of the membrane humidity. And the average diameter of the channel is 2.4 nm at 20%Rh.
2. The section of the channels is 0.8 nm. Therefore, the volume of each channel is $\pi r^2 h = \pi(1.2)^2(0.8) = 3.6 \text{ nm}^3$.
3. Because the density of water is equal to $1 \text{ g/mm}^3 = 33 \text{ m}_{\text{H}_2\text{O}}/\text{nm}^3$, the channel can gather amount of water = $33 \times 3.6 = 120 \text{ m}_{\text{H}_2\text{O}}$.

Table 5.1 Morphological quantities of Nafion modeled by the cylindrical water channel model.

	Ionic water channel			Crystallite structure		
	Dry	Hydrate	Average	Dry	Hydrate	Average
Diameter (nm)	1.8	3.5	2.4	3.0	8.0	5.5
Section (nm)	0.8	0.8	0.8	50	50	50
Area (nm ²)						
Transverse plane	2.54	10.18	4.52	7.07	50.27	23.76
Sagittal plane	1.44	2.80	1.92	150	400	275
Volume (nm ³)	2.03	8.14	3.62	353.50	2513.50	1188.00

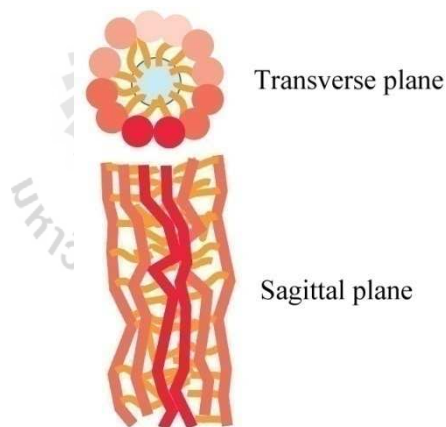


Figure 5.3 Transverse and sagittal planes of Nafion membrane.

- At high degrees of membrane humidity such as $\lambda = 7.5$, the number of the backbone chains containing in each channel is equal to $120 \text{ m}_{\text{H}_2\text{O}} / 7.5 \text{ m}_{\text{H}_2\text{O}} = 16$ chains per channel.
- At 16%Rh, the crystallites have a diameter of 3-8 nm with the length of 50 nm

From these reports, the essential parameters for the photon fluence are summarized in Table 5.1. It is important to note that the effect of VUV irradiations depend on the direction of incident photon on the membranes, which are defined by transverse and sagittal planes of incident photons as shown in Figure 5.3.

5.1.2 Threshold fluence

In polymer science and plasma physics, the effects of radiation depend on the total number of incident particles or ions per unit area over exposure times rather than only the number of incident particles or ions per unit area. For this reason, the definition of the radiation fluence has been applied because increasing in the fluence results in the increment of the irradiation effects on the materials. Furthermore, the VUV fluence for Nafion is directly related to the radiation dose of the membrane because the membrane absorbs all incident photons. Therefore, the radiation dose which defined as the radiation effect to the materials can be expressed in term of the photon fluence to the Nafion polymer.

In this thesis, the effects of VUV irradiations are examined with the assumption states that there is at least one photon impacting on the smallest units of the Nafion membrane during irradiations. Based on the cylindrical nano-channels model, the smallest molecular unit is assumed to be the dried ionic channel that has possibly been obstructed by the contaminants in the photo-degradation mechanism prior to the VUV irradiations such as the oxygen-intervene molecules as described in Section 3.4. By using the definition of fluence, the number of the employed photons for irradiation can be calculated from the photon fluences as shows in the following calculations.

From Table 5.1, the irradiated area is considered to be the area in the sagittal direction of the dried ionic channel because the irradiations have been performed in an ultrahigh vacuum chamber where the membrane is completely dried. Therefore, the effective area of irradiation is

$$A = 1.44 \text{ nm}^2 \quad (5.1)$$

If one photon is entered in this area over the time of irradiation, the structure of the membrane is initially changed. The corresponding "threshold" photon fluence can be expressed as

$$F_{\text{threshold}} = \frac{1 \text{ photon in time of irradiation}}{A} = 0.694 \text{ photons/nm}^2 \quad (5.2)$$

This threshold fluence is assigned to be the initial value for the VUV irradiations and the photoemission spectroscopy (PES) measurements. The first PES measurements, performed at the beamline 4 (BL4), have been considered as the preliminary results of the electronic structure of the membranes during irradiations; while the high performance PES measurements have been performed after relocate the PES systems to the new beamline 3.2a (BL3.2a).

To examine the evolutions of the electronic structure of Nafion during the VUV irradiations, moreover, the membranes have been irradiated by using several photon fluences, which cover the threshold fluence. The trial photon fluences and the corresponding number of incident photons for the effective irradiation areas are show in Table 5.2. These corresponding incident photons can easily be calculated by multiplying the fluence with the irradiated area as described in Equation (5.1).

Table 5.2 Irradiation data for VUV irradiations and PES measurements.

Trial photon fluences (photons/nm ²)	Trial photon fluences (photons/cm ²)	Number of incident photons per unit cell
0.0	0.0	0.00
0.4	4.0×10^{13}	0.58
0.8	8.0×10^{13}	1.15
1.2	1.2×10^{14}	1.73
2.4	2.4×10^{14}	3.46
3.2	3.2×10^{14}	4.61

It is important to note that the VUV fluences are similar to the fluences for the PES measurements. The insignificant difference between the trial photon fluences and the calculated fluence in Equation (5.2) arises from the difficulty to control these fluences during the PES measurements, which depends on the acquisition times of each PES scan. Nevertheless, these trial fluences cover the threshold fluence and can be used to modify the surface structure of the degraded Nafion. The calculations of the photon fluence are shown in the following section.

5.1.3 Photon fluences for the VUV irradiations

The preliminary PES measurements and the VUV irradiations are performed at the BL4 in order to calculate appropriated photon fluences. After moving the experimental system to the BL3.2a, further pragmatic PES measurements have been elucidated in order to clarify the effects of VUV irradiations to the membranes and spectra quantitatively analysis. Note that these PES measurements have been investigated after the fuel cell performance tests.

Table 5.3 The beam size for two experimental systems (PES measurement and VUV irradiation).

	Beam length at BL4 ⁽¹⁾ (cm)				Beam length at BL3.2a ⁽²⁾ (cm)			
	ARPES chamber		Irradiation chamber		ARPES chamber		Irradiation chamber	
	Ver- tical	Hori- zontal	Ver- tical	Hori- zontal	Ver- tical	Hori- zontal	Ver- tical	Hori- zontal
FWHM	0.024	0.060	0.080	0.105	0.010	0.030		
Full	0.056	0.141	0.188	0.247	0.024	0.071		
	Beam area at BL4 (cm ²)				Beam area at BL3.2a (cm ²)			
FWHM	1.44×10 ⁻³		8.40×10 ⁻³		3.00×10 ⁻⁴			
Full	7.952×10 ⁻³		4.64×10 ⁻²		1.66×10 ⁻³			
	Photons flux at BL4 (photons/s)				Photons flux at BL3.2a (photons/s)			
	ARPES chamber		Irradiation chamber		ARPES chamber		Irradiation chamber	
Slit=10 μm	3.17×10 ⁹		3.17×10 ⁹		4.15×10 ⁷		4.15×10 ⁷	
Slit=20 μm					1.38×10 ⁹		1.38×10 ⁹	
Slit=100 μm	5.14×10 ¹⁰		5.14×10 ¹⁰					
	Photon flux density at BL4 (D) (photons/s•cm ²)				Photon flux density at BL3.2a (D) (photons/s•cm ²)			
	ARPES chamber		Irradiation chamber		ARPES chamber		Irradiation chamber	
Slit=10 μm	3.99×10 ¹¹		3.99×10 ¹¹		2.51×10 ¹⁰		2.51×10 ¹⁰	
Slit=20 μm					8.36×10 ¹¹		8.36×10 ¹¹	
Slit=100 μm	1.11×10 ¹²		1.11×10 ¹²					

⁽¹⁾Calculated by the Shadow VUI ray tracing program

⁽²⁾From [http:// www.slri.or.th](http://www.slri.or.th)

Generally, the different experimental setup between the BL4 and the BL3.2a cause to the difference design for the size of the photon beam, resulting in the difference in the photon flux density. The corresponding fluences for these two stations have been collaborated separately. Each of which have two experimental segments The PES were performed in the angle resolved photoemission spectroscopy (ARPES) chamber and the VUV irradiation were performed in the irradiation chamber. Basically, the essential parameters for the fluence calculations are the beam size of the photon beam and the photon flux as shown in Table 5.3. The calculations of the photon fluences at the BL4 are shown in the following section.

5.2 VUV Irradiations of the Degraded Nafion at the BL4

The photon flux, P (the flow of photons impacting on the membranes) at the BL4 is obtained by measuring the current of the incident photon beam on the photodiodes. This electric current is related to the photon flux by means of the electron-hole pairs interaction. This quantity depends on the experimental setup of each beamline such as the slit width (10 μm) and the photon energy (100 eV). The slit width is assigned to have the minimum value in order to reduce the charging effect during the PES measurements. And the photon energy is set to the energy of 100 eV, which is in the range of VUV region. Thus, the measured photon flux at the BL4 is

$$P = 4.59 \times 10^9 \text{ photons/s} \quad (5.3)$$

Because the photon flux recorded from the photodiodes and the PES measurements are different, it must be normalized by the electron current in the storage ring (I_e).

Table 5.4 Electron currents (I_e) of the storage ring at the BL4, SLRI. The I_e is measured during the PES measurement ($I_{e,PES}$) and during the photodiodes measurement ($I_{e, diodes}$).

Electron current of the PES measurement at the BL4 ($I_{e,PES}$)	Electron current of photodiodes measurement at the BL4 ($I_{e, diodes}$)
88.30 mA	127.72 mA

Furthermore, in the SLRI synchrotron facility, the life-time of the beam results from the attenuation of the electron currents. The photon flux has been normalized to be the average photon flux at the standard electron current (100 mA). The electron currents recorded during the PES measurements and the photodiodes measurement are shown in Table 5.4. Although the average value is 108 mA due to the difficulty to take the experiment at the standard electron current, the average photon flux given by these parameters is acceptable.

Nevertheless, the average photon flux in this thesis is

$$\begin{aligned}
 P_{(PES,BL4)} &= P \times \left(\frac{I_{e,PES}}{I_{e,diodes}} \right) = 4.59 \times 10^9 \times \left(\frac{88.30}{127.72} \right) \\
 &= 3.17 \times 10^9 \text{ photons/s} \quad (5.4)
 \end{aligned}$$

To enlarge the irradiated areas of the membranes before the fuel cell performance tests, the VUV irradiations have been performed at the irradiation chamber (43 cm far away from the ARPES chamber). Table 5.2 shows that the beam size of this chamber is almost 6 times larger than the beam size of the ARPES. However, the beam has inadequate size for the requirement of the active area for the fuel cell performance tests (1 cm^2).

5.2.1 Slit factor

For this requirement, the VUV irradiations have been carried out by scanning the exposed membranes vertically within the length of 1 cm, and tilting the membranes horizontally to have the exposed length of 1 cm. The methods for the VUV irradiation at the BL4 have been demonstrated in Appendix A.

Moreover, the photon flux can be increased by increasing the slit width. It is feasible to adjust the slit width because the charging effect is realized to be an insignificant parameter for the VUV irradiations. For this reason, the slit width in the VUV irradiation is assigned to be 100 μm . However, there is no direct information of the photodiodes measurement that provides the photon flux at 100 μm . In fact, the slit width has only been assigned to be 10 μm and 20 μm . Nevertheless, assuming that the photon flux linearly relates to the slit width, the photon flux for the slit width of 100 μm can be obtained by multiplying the photon flux for 10 μm with the slit factor. Consequently, the slit width, the photon flux density (D) and the corresponding photon fluences (F) have also been calculated using this quantity as shown in the following procedure.

The slit factor for the VUV irradiations can be obtained by the photon flux which is measured at the slit width of 10 and 20 μm as shown in Table 5.5. Obviously, when the slit width increases by factor = 2 (from 10 to 20 μm), the resulting photon flux is increased by factor = 3.24. Therefore, the relatively slit factor for 100 μm is equal to $3.24 \times 5 = 16.2$. Consequently, the photons flux of VUV irradiation at the BL4 for the 100 μm slit width is

$$P = (3.7 \times 10^9) \times 16.2 = 5.14 \times 10^{10} \text{ photons/s} \quad (5.5)$$

Table 5.5 Relation between the electron currents and the normalized photon flux measured at $S = 10$ and $20 \mu\text{m}$. These quantities have been used for the slit factor calculations.

Slit width = $10 \mu\text{m}$				Slit width = $20 \mu\text{m}$			
Photon flux (photodiodes) (photons/s)	$I_{e,\text{diodes}}$ (mA)	$I_{e,\text{measure}}$ (mA)	Normalized photon flux (photons/s)	Photon flux (photodiodes) (photons/s)	$I_{e,\text{diodes}}$ (mA)	$I_{e,\text{measure}}$ (mA)	Normalized photon flux (photons/s)
4.59×10^9	127.72	88.30	3.17×10^9	1.51×10^{10}	123.50	84.12	1.03×10^{10}

5.2.2 Photon flux density

The photon flux expressed in Equation (5.5) is then used to calculate the photon flux density (D) defined as

$$D = P/A, \quad (5.6)$$

where A is the exposed area of the sample at the irradiation chamber at the BL4,

$$A = (0.188 \times 0.247) = 0.046 \text{ cm}^2 \quad (5.7)$$

Thus, the photon flux density is

$$D = (5.14 \times 10^{10}) / 0.046 = 1.11 \times 10^{12} \text{ photons/s} \cdot \text{cm}^2 \quad (5.8)$$

5.2.3 Photon fluences

Accordingly, the photon fluences can be calculated according to the definition of the fluence,

$$F = DT. \quad (5.9)$$

By setting exposed times (T), the corresponding photon fluences for the VUV irradiation at the BL4 can be calculated as shown in Table 5.6. Note that these results are similar to the total photon fluences shown in Table 5.3.

Table 5.6 The corresponding photon fluences for the VUV irradiations at the BL4.

Irradiation time (second)	Corresponding photon fluence (photons/cm ²)
0	0.0
36	4.0×10^{13}
72	8.0×10^{13}
108	1.2×10^{14}
216	2.4×10^{14}
288	3.2×10^{14}

5.3 Other Surface Modification Techniques

In order to compare the modification affects on the membrane surface with these VUV fluences (at 100eV), several surface modification techniques such as Ar⁺ sputtering, VUV irradiations with the variation of photon energies and the zero-order synchrotron radiation have been performed. The comparison of these results ascribes the usable techniques for the membrane modification. It is supposed that the best membrane modification technique shouldn't lower the chemical and mechanical properties of the membrane after modification.

5.3.1 Argon ions (Ar⁺) sputtering

According to the Ar⁺ sputtering of Nafion provided by Cho (Cho, Cho, Oh, Kim and Ha, 2006), the single fuel cell performance using the ion sputtered membranes was increased, with the maximum power density up to 0.62 W/cm² (which was 2 times higher than that of the fuel cell using the untreated membrane). The improvement of the fuel cell performance is due to the surface roughening after ion bombardments. The increase in the roughness results in the increase of the surface active area between electrolyte and catalyst.

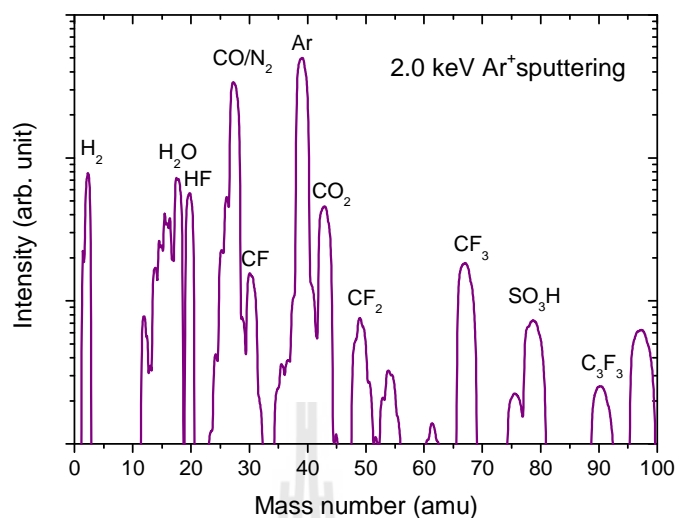


Figure 5.4 Mass spectra of the Nafion membrane excited by the 2.0 keV of Ar^+ . The major fragments are CF, CF_2 , CF_3 and SO_3H .

In this thesis, the low energies Ar^+ sputtering (0-3 keV) for the Nafion surface modification have been performed. During bombardment, the fragmentations of the molecular species of Nafion are characterized by mass spectrometry. This technique employs the residual gas analyzer (RGA) to analyze the molecular species of Nafion during Ar ions bombardment in vacuum chamber, with the base pressure of $\sim 10^{-6}$ mbar. The mass spectra indicate that the fragmentations of Nafion species compose of the CF, CF_2 , CF_3 and SO_3H fragments, which generate from the Nafion backbones and side chains during sputtering as well as the standard molecule (Ar, CO/N_2 , H_2O and H_2) in vacuum. The mass spectra of Nafion excited by the 2.0 keV Ar^+ , for example, are depicted in Figure 5.4.

Interestingly, the mass intensities of all molecular species are increased with increasing the ion energy. It is concluded that the surface modification of Ar^+ sputtering is extremely affects to the Nafion membranes.

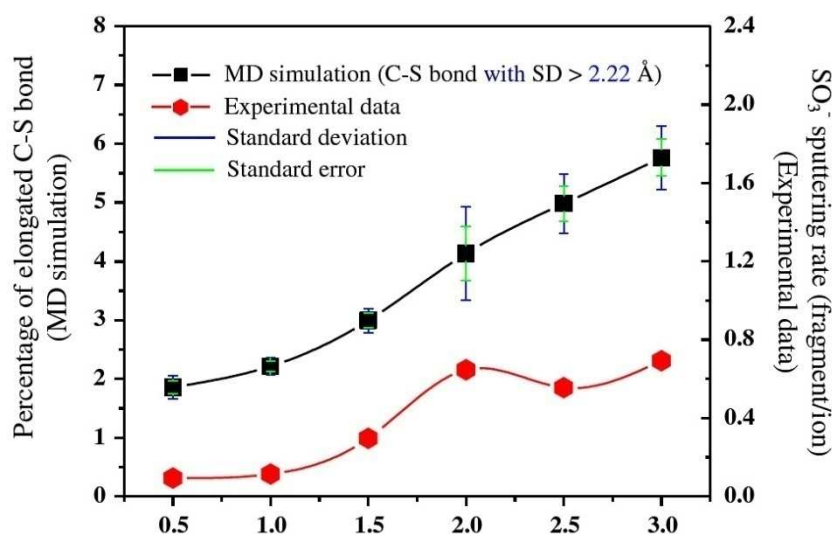


Figure 5.5 Intensity (in terms of area under curve) of the Nafion molecular species (CF_2CF_3 and SO_3H) is plotted as a function of ion energy. The percentage of elongated C-S bond in the simulation, which corresponds to the intensity of the molecular species in the sputtering measurements, is increased with increasing the energy of argon ions.

To verify the sputtering effects, The Ar^+ sputtering results are also compared with the computational study of the Ar^+ bombardment on Nafion by the molecular dynamic (MD) simulations (Yana et al., 2011). This research using the computational code named the assisted model building with energy refinement (AMBER) to simulate the structural changes upon various ions energies (0.5-3.0 keV). In contrast, the atomic level of the Nafion surface modification has been simulated using 1024 units of the Nafion side chains. The effect of the ion bombardment was described by the C-S bond stretching, which is directly related to the SO_3^- fragmentations of the experimental results. From this result, the MD calculation is in agreement with the Ar^+ sputtering results as shown in Figure 5.5.

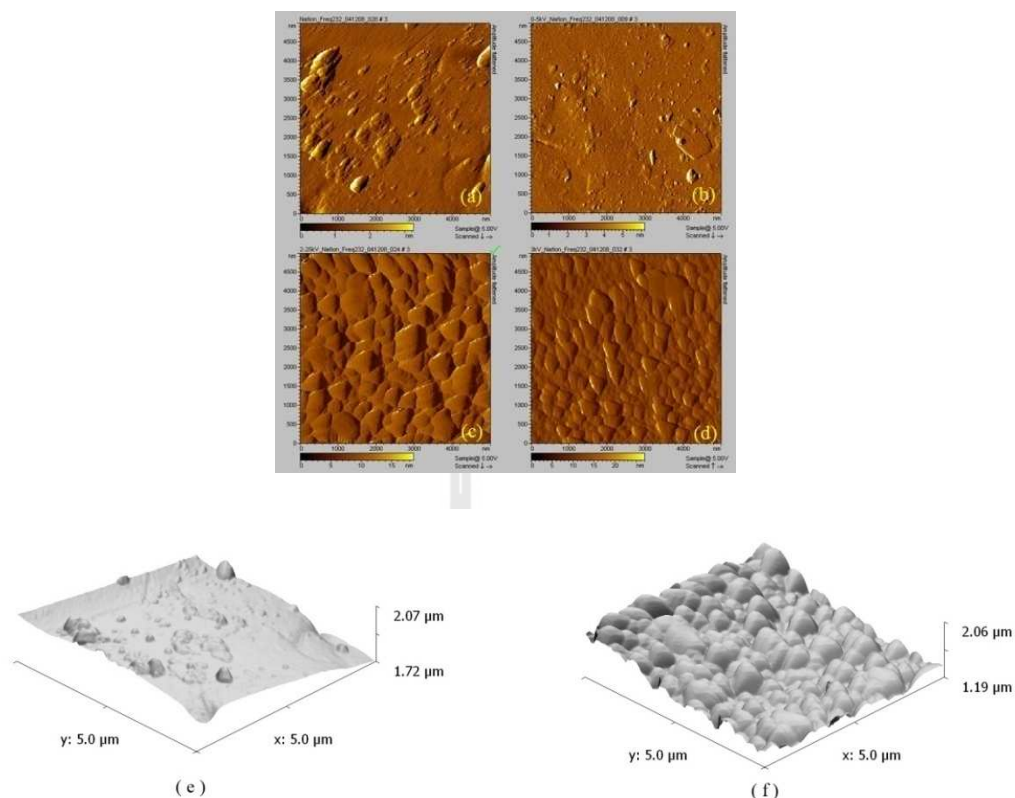


Figure 5.6 AFM images of the Nafion with no sputtering (a), after 0.50 keV (b), 2.25 keV (c) and 3.00 keV Ar^+ sputtering (d), respectively. These pictures were taken with the field of view of 5000 nm and also converted to the 3-Dimensional of no sputtering (e) and 2.25 keV sputtering (f), respectively.

To display the surface Nafion after bombardments, the microscopy technique has been considered. Particularly, atomic force microscopy (AFM) has been conducted. The tapping mode of the AFM measurements with 5000 nm field of view reveals the change in the surface roughness of the membrane after sputtering. The membrane roughness is increased with increasing the ion energy as shown in Figure 5.6. From these Ar^+ sputtering technique, it is expected that the surface roughening results in the increment of the surface active area of Nafion.

Therefore, their interfacial area connection between the electrolyte membrane and the catalyst has been increased. And the performance of PEMFC using this modified membrane should consequently be enhanced. However, the surface modification by sputtering technique has some issues such as pores interception at the surface and the reduction of the hydrophobicity of the membrane after ion bombardments. These effects are the affectation for the decrease in the membrane conductivity, as reported by Ramdutt and his co-workers (Ramdutt et al., 2007). From this issue, it is suggested that the Ar^+ sputtering technique is an inappropriate modification technique for the degraded Nafion.

5.3.2 Photon bombardments

Since the Ar^+ sputtering is suggested to be an inapplicable modification technique for the degraded Nafion, the surface treatment with mildly conditions such as the subtle source of photon has been considered. With the contribution of the synchrotron source at SLRI, the variation of photon energies have easily been adjusted by the grating monochromator. The photon beam with the energy range of UV from synchrotron radiation is expected to be a mildly surface modification of the polymer rather than the Ar^+ ion bombardments. Note that the UV synchrotron techniques are also largely used in the polymerization such as the radiation graft polymerization of styrene into PTFE film by UV (Asano et al., 2007).

For this modification, the zero-order synchrotron light (the polychromatic photon beam that contains various photon energies) has been used as an exciting source. During exposure the membranes to the zero-order light, the membrane fragmentations are also detected by the residual gas analyzer (RGA) similar to the fragmentation measurements of the Ar^+ sputtering.

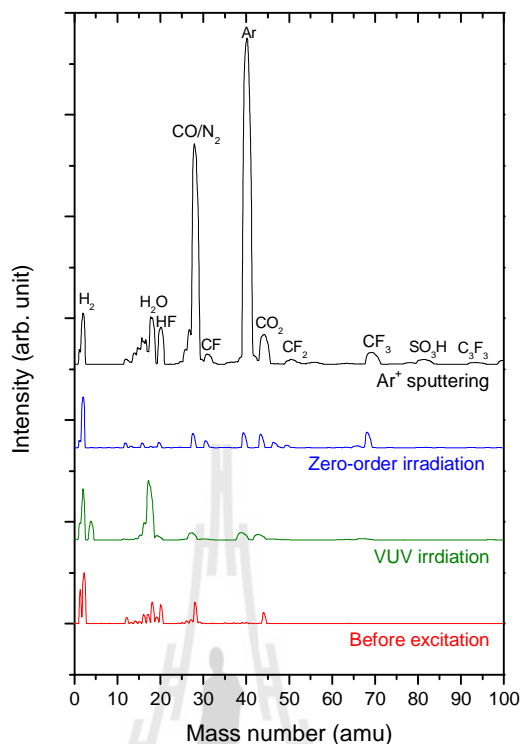


Figure 5.7 Mass spectra of Nafion membrane excited by 2.0 keV of Ar^+ sputtering, zero-order synchrotron light, 100 eV VUV radiation and without excitation.

Moreover, this mass spectrometry results have been compared with the photon bombardments exciting by the monochromatic beam at 100 eV, which is in the range of the VUV radiation. Figure 5.7 summarizes the comparison of the mass results excited by Ar^+ sputtering, zero-order irradiation and VUV irradiation with the energy of 100 eV. These results are also compared with the mass spectra of the unexcited membrane (before irradiation). Explicitly, the mass results show that the Ar^+ bombardment cause to an excessive fragmentation of the Nafion molecular species because of the highest mass intensity in comparison with other excitations.

The very large interaction with the Nafion implies that the ions bombardment may not be suitable for the membrane surface modification due to the reduction of the proton conductivity, though the surface roughness is even increased with ions energy.

On the same effect, the zero-order synchrotron irradiation generates small fragments compared with the ion sputtering. However, the main Nafion molecular species such as CF_3 have always been detected by this excitation. This can be ascribed that the zero-order irradiation also causes to excessively change the structure of the Nafion at the main chains similar to the Ar^+ bombardment, results in the decrease in the mechanical property of the membrane after surface modification.

On the other hand, while the Ar^+ sputtering and the zero-order synchrotron radiations have an excessive effect to the surface of Nafion, the VUV irradiation is the gentlest effect. Implicitly, the VUV irradiation is the preferential surface modification technique for this membrane.

Note that the electron electronic structures of the Nafion characterized by the photoemission spectroscopy of various photon energies (40-160 eV) are demonstrated in Appendix B. These results show that the electronic structure of the Nafion membrane have been changed after irradiations with various energies of VUV synchrotron radiations. However, due to the low signal to noise ratio spectra measurements at the BL4, the results have been compared only to examine the changes in the PES intensity, not for quantitatively calculations such as area under curves. As described in Section 5.1.2, the rigorous PES measurements have been performed at the BL3.2a because of the higher PES intensity and resolution. The analysis electronic structure using the PES measurements at the BL3.2a and using computational calculations will be discussed in Sections 5.6 and 5.7.

5.4 Small Angle X-ray Scattering

In order to study the morphological changes inside materials, small angle X-ray scattering (SAXS) technique has been conducted. It is well known that the complex structure can be characterized by scattering techniques where the variation of nano-scale size and configuration of materials have been monitored by the selected X-ray energy. For Nafion, there are many researches on the nanostructure of the membranes (Tsao et al., 2005), (Barbi, Funari, Gehrke, Scharnagl and Stribeck, 2003). However, the complete structural implementation of the Nafion and also the degraded Nafion membranes has not been attained.

According to the basis of SAXS analysis (Page et al., 2006), Nafion membrane has two different structures. The complex, phase-separated morphology of Nafion, consists of crystalline and ionic domains as described in Chapter III. Due to the electron density differences between the ionic domains and the PTFE matrix, a scattering maximum appears in small-angle X-ray scattering profiles at $q \sim 1-2 \text{ nm}^{-1}$, which has been termed the "ionomers peak". While a very low angle peak or shoulder is often observed at $q = 0.4 \text{ nm}^{-1}$, which has been attributed to scattering from the locally ordered crystalline composed of relatively long runs of PTFE segments between side chains (termed the "crystallites peak").

In this thesis, the SAXS study is performed in order to examine the irradiation effect to the surface of the degraded Nafion membrane. Although the surface morphology of the membrane provided by SAXS is very complicated, it is expected that the structural transfiguration of the degraded Nafion after VUV irradiations can be investigated. And the enhancement in the ionic domain after irradiation which results in the improvement of the PEMFC can be satisfied by this method.

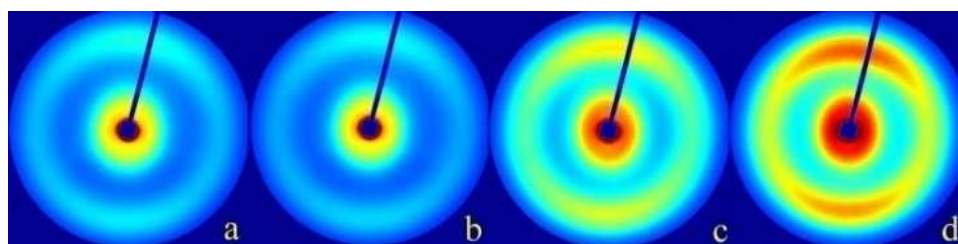


Figure 5.8 SAXS images of the unirradiated membrane in the dried state (a) the VUV irradiated membrane in the dried state (b), the unirradiated membrane in the hydrated state (c), and the VUV irradiated membrane in the hydrated state (d).

Figure 5.8 illustrates the SAXS patterns of the degraded membranes before and after VUV irradiations in dried and hydrated states. The hydrated membrane can be achieved by dipping the membrane in the de-ionized water for 60 minutes. The membranes are treated by VUV irradiation with the photon fluence of 1.2×10^{14} photons/cm². The scattering patterns appear anisotropic scattering due to the membrane photo-degradation prior to the VUV treatment. In particular, the two equatorial bands on the top and the bottom of the pattern are attributed to scattering arising from the oriented ionic domains at the sulfonic acid group side chain, while the small band near the center is attributed to the distribution of the crystalline domain at the polymer backbone. With the contribution of VUV treatment, the orientation of the ionic domain in the hydrated state is rearranged as depicted in the improvement of the ionic bands distribution (d) in comparison to the scattering patterns of the untreated membrane (c). At this point, the surface contaminants may be responsible for ionic channel alteration and they have possibly been eliminated by the VUV irradiations. However, the rearrangement of the ionic domain after VUV treatment is not clear and requires further studies.

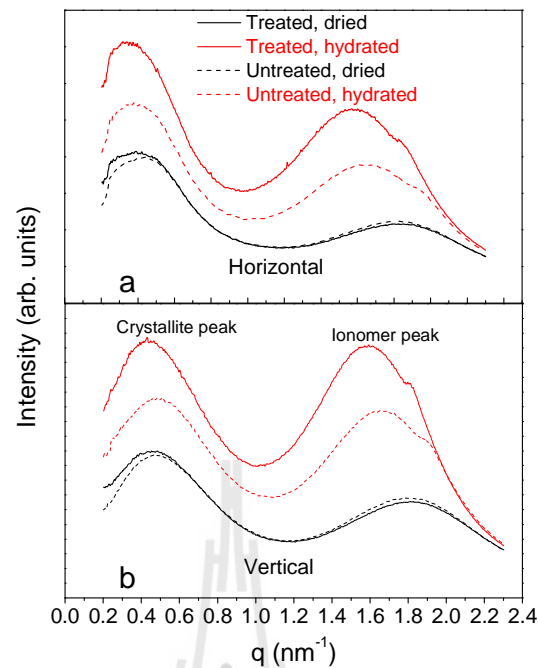


Figure 5.9 SAXS profiles of the untreated and the treated membranes in dry and hydrated states integrated in the horizontal direction (a) and the untreated and the treated membranes in dry and hydrated states integrated in the vertical direction (b).

The development of the ionic water nanochannels has also been demonstrated in the SAXS profiles in Figure 5.9 where the scattered intensity is plotted as a function of the scattering vector, $q = 4\pi \sin \theta / \lambda$. There are two characteristic peaks relates to the phase separation of the periodic morphology structures within the membrane. Eventually, the measuring peak around $q = 0.45 \text{ nm}^{-1}$ is the crystallite peak of the polymer main chains. And the small peak around $q = 1.6\text{-}1.8 \text{ nm}^{-1}$ is the ionomer peak. For the dry state, no different in the scattering vector has been detected. However, the different in the peaks between the irradiated and the unirradiated membranes has been detected. The scattering peak of the hydrated membrane move to lower scattering vector, compared to that of the dried membrane.

Because the decreasing in the scattering vector q is related to the increase in the domain size of the materials, these scattering results indicate the extension of in the hydrated ionic sites upon VUV irradiations. The extension is up to 6%, compared to the scattering vector of the unirradiated membrane. However, this phenomenon is still being unclear because the VUV modifications occur at the surface, while the SAXS measurement probes the bulk structure of the membrane. The change of the ionic domain size is possibly due to either the VUV effects or an inhomogeneous structure of the membrane prior to the VUV irradiation. At this point, only the change of the bulk structure of the membrane after VUV irradiation such as the polymer cross-linking has been examined by the SAXS measurements.

According to the SAXS results using gamma ray irradiations reported by Tsao (Tsao et al., 2005), the Nafion membrane has undergone polymer cross-linking after the irradiation. This formation caused to the reduction of the inter-lamellar distance between the crystalline domains and decreasing in the ionic cluster domain size.

In this thesis, however, no significant changes in the crystallite peaks from the intensity integration of both the horizontal and the vertical direction have been observed after irradiation. Obviously, the crystallinity of the degraded membrane with and without the VUV irradiation has not been changed. This result indicates that the Nafion membranes do not undergo the polymer cross-linking. On the other hand, the VUV irradiations have an effect only on the surface which is occupied by the membrane contaminations in the photo-degradation mechanism.

For this reason, with gentle VUV fluences performing in this thesis, the SAXS results confirm that the VUV irradiation is the appropriate method for the membrane. These results are also in agreement with the results from mass spectrometry.

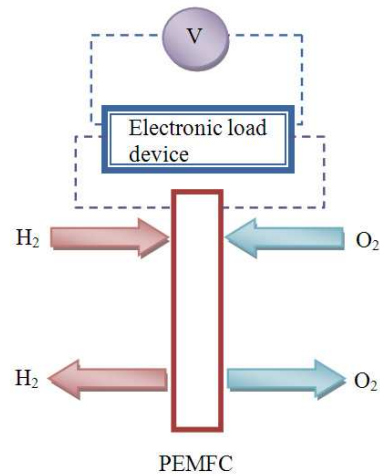


Figure 5.10 Schematic diagram of single PEMFC operation.

5.5 Fuel Cell Performance Test

To examine the PEMFC performance, the PEMFC testing system has been conducted. As illustrated in Figure 5.10, this system consists of H_2 and O_2 supplies, electronic load device, single PEM fuel cell and the computer controlling system. The operation of the fuel cell test system is similar to the PEM fuel cell operation. The system has been connected with a tunable electronic load device, where the voltage (V) has simultaneously been recorded with the fuel cell current density (J). The performance of the PEMFC is demonstrated by the graph of the fuel cell current density and the cell voltage (J-V or the polarization curve).

Before performance test, the membrane electrode assembly (MEA) using the irradiated Nafion has been constructed by hot-pressing as described in Section 2.4. In this PEMFC operation, the inlet gases have been humidified before entering to this fuel cell in order to optimize the electrochemical reactions and the proton transportation through the membrane.

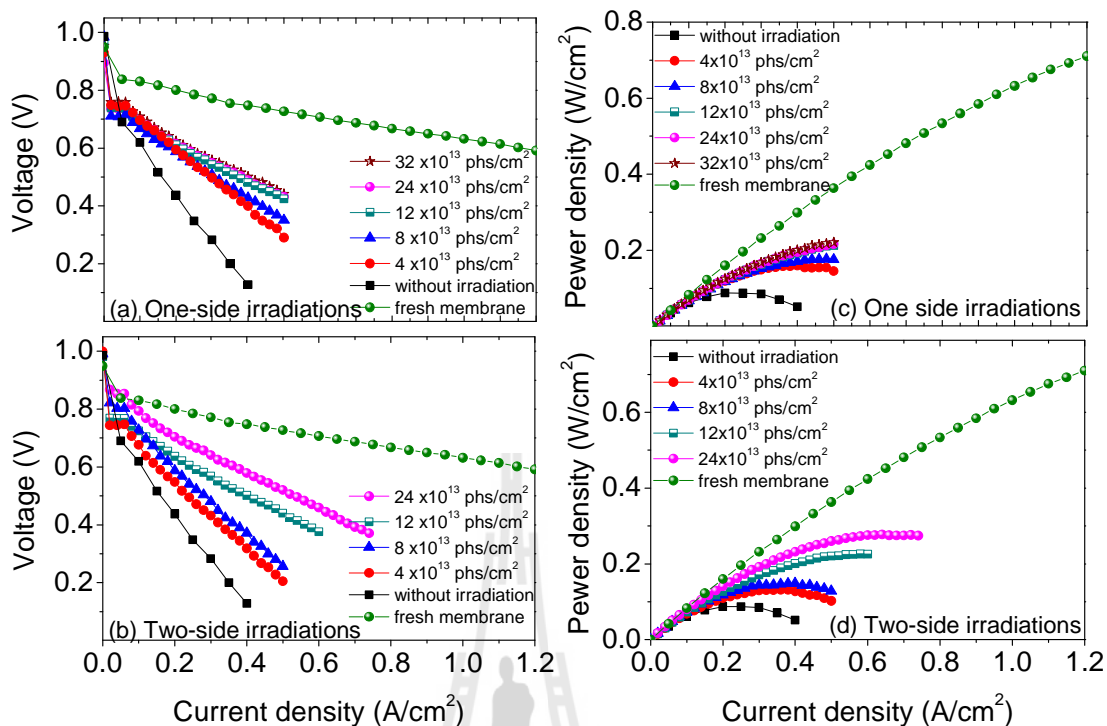


Figure 5.11 Polarization curves and the fuel cell power density of the single fuel cell using the irradiated Nafion membranes with one-side and two-side irradiations.

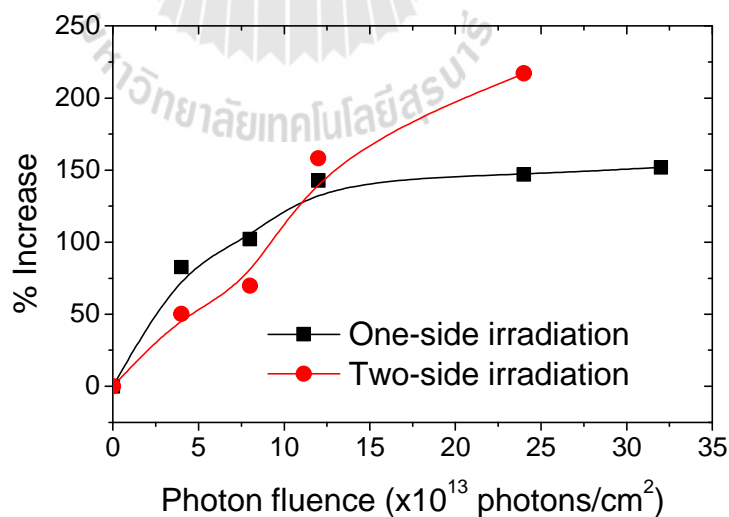


Figure 5.12 The improvement of the maximum power density of the PEMFC as a function of the photon fluences.

During PEM fuel cell operation, the single PEMFC is connected with an electronic load device to control the fuel cell current density. Figure 5.11 shows the polarization curves of the fuel cell using the VUV irradiated Nafion with the different fluences ($0-3.2 \times 10^{14}$ photons/cm²), which cover the threshold fluence (6.94×10^{13} photons/cm²) as described in Section 5.2 and also shows the corresponding fuel cell power density.

According to the relation between the fuel cell potential and efficiency given by Equation (2.60), the performance of the PEMFC using the irradiated Nafion membranes explicitly increases with increasing the photon fluences in the VUV irradiations. The maximum current density at 0.6 V is 0.4 A/cm². The maximum power density of a fuel cell is up to 0.28 W/cm² for the VUV irradiation with the fluences $\sim 2.4 \times 10^{14}$ photons/cm² (two-side irradiation at 0.6 A/cm²).

However, the maximum power density of the PEMFC using these modified membranes in one-side and two-side of VUV irradiations have been demonstrated in Figure 5.12. These quantities are obtained by multiplying the cell current density with the cell potential.

Although the performance of the PEMFC using the irradiated membranes are lower than that using the fresh membrane (Tian, Gao, Zhang, Luo and Shan, 2008), the VUV modification exhibits the improvement of the performance with increasing the photon fluences and even compared to the pristine degraded membrane. It is expected that this improvement is occurred on the surface of the irradiated membranes. The surface effects of VUV irradiations have been investigated as indicated in the comparison of the current density at 0.6V for one and two-side irradiations in Figure 5.13.

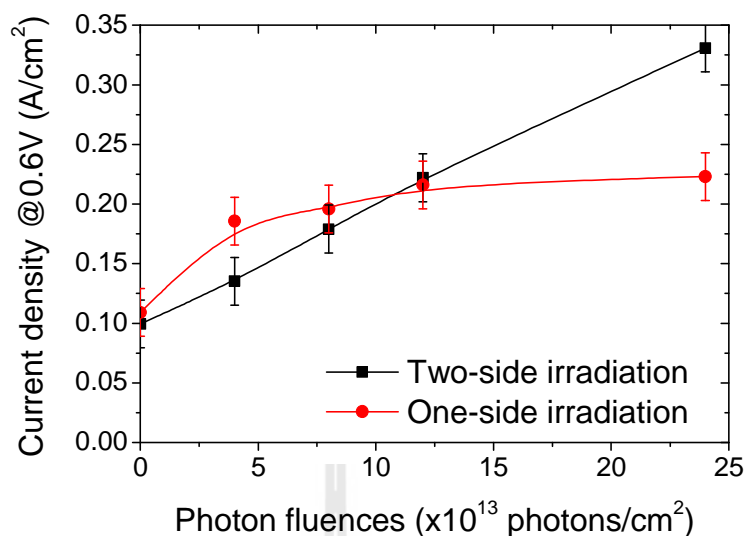


Figure 5.13 Current density at 0.6 V of the fuel cell using VUV irradiated membranes.

The higher performance of the two-side irradiation compared with the one-side irradiation certainly results from the surface modification effect by VUV irradiations. This result confirms the surface effect, which is already investigated by the PES and the SAXS measurements.

5.6 Photoemission Measurements

The rigorous PES measurements have been performed at the BL3.2a, where the PES system has been upgraded. Many powerful devices such as U60 undulator and the new grating monochromators have been upgraded to support the efficacious measurements. This combination serves the improvement of the signal-to-noise ratios, resulting in the better PES intensity. Specially, the PES measurement of the insulating materials such as the Nafion polymer electrolyte membrane requires higher intensity to specify the PES peaks.

5.6.1 The photon fluence calculation for the BL3.2a

Before PES measurements, it is important to notes that the photon flux in the BL3.2a can be obtained by the different manner from the calculation in Sections 5.2. In contrast, this quantity can be calculated from the photodiode's current (I_s). Furthermore, the gold mesh has been installed between the sample's position and the monochromator in order to recording the photon current (I_p) simultaneously with the measurement of the I_s for the photon fluence calculations and also recording the I_p during the PES measurements. While the I_s is used to calculate the photon fluences, the I_p is also used to normalize the PES intensities for each scan. Because the photon beams cannot pass through the photodiodes to the sample, it should be suitable to normalize the PES intensity by the photon current detected by the gold mesh rather than the photodiodes. The details of the normalization of the PES spectra will be described in the next section.

The photon flux is defined as the photoelectrons per unit time per the quantum efficiency of the photodiodes.

$$P = \frac{I_s}{eQ_s}, \quad (5.10)$$

where e is the electric charges (1.6×10^{-19} C) and Q_s is the quantum efficiency of the photodiodes at a given photon energy (100 eV). The average photodiodes current have been performed within 50 I_s records. The average photodiodes current and the average photon current at the measuring electron current are shown in Table 5.7.

The measured quantum efficiency of the photodiodes (Q_s) at the photon energy of 100 eV is

$$Q_s = 7.287 . \quad (5.11)$$

Table 5.7 The average photodiodes and gold mesh currents for number of photon calculation.

Average electron current at the BL3.2a	Average photodiodes current (I_s)	Average photon current (I_p)
122.08 mA	4.84×10^{-11} A	1.42×10^{-11} A

The following photon flux is expressed as

$$P = \frac{I_s}{eQ_s} = \frac{4.84 \times 10^{-11}}{(7.287 \times 1.6 \times 10^{-19})} = 4.15 \times 10^7 \text{ photons/s.} \quad (5.12)$$

Notes that this photodiodes's current in the PES system is lower than the expected value of the BL3.2a due to the problem of the cylindrical focusing mirror (M2Cy), which is placed before the PES chamber at that time. However, the photon current at the chamber that placed before this mirror can be measured. The photon current with the slit width of 50 μm is equal to 1.02×10^{-5} A. Explicitly, the current will be decreased when decreasing the slit width down to 10 μm . According to the linearly relation of the photon flux and the slit width in Table 5.4, the photon flux at that chamber should be equal to 4.4×10^{10} photons/s. This value is really higher than the photon flux at the BL4 (3.17×10^9 photons/s). It is guarantee that the photon flux at the BL3.2a is higher than the photon flux at the BL4. The problem in the lowering current is due to the alignment of the M2Cy. At the time of measurement, the photon flux at anywhere of the BL3.2a after the M2Cy was reduced. The resulting currents measured at the PES system were then reduced and the photon flux at the PES system had been decreased. Nevertheless, the PES measurements were performed at the PES system so the calculation demonstrated in Equation (5.12) is acceptable.

Thus this photon flux has been used to calculate the photon flux density and also the photon fluences for the PES measurements, which can subsequently be used to determine the measuring time of the PES and the corresponding PES spectra for a given photon fluence. Additionally, before analysis the PES spectra have been normalized to be the comparable spectra.

5.6.2 Normalization of the PES intensity

Because the number of photons attenuates simultaneously with the electron current in the storage synchrotron ring at SLRI after injection, the intensity of the photoelectron has also been reduced with the measuring times. For this reason, the PES spectra of Nafion should be normalized by the photon current (I_p) of each individual scan.

Because the photon currents have been recorded by the program that collect the data from the gold mesh (at the XPS chamber), which differs from the PES data acquisitions program (at the ARPES chamber), the recorded number of scan of I_p also differ from the number of scan of the PES measurements. Thus, the measured I_p that correspond to the number of the PES scans must be selected through the overall data. It should be noted that the PES measurements are related to the I_p measurements because the I_p and the PES measurement have the same measuring time as shown in Table 5.8. Thus, the relatively I_p for each PES scan can be obtained by the following calculations.

The scanning time interval in one complete scan for the I_p and the PES measurement can easily be calculated by dividing the PES measuring time with the corresponding number of scans. And the I_p for each the PES scan can be obtained by linear fit of I_p within entirely scans as shown in Figure 5.14.

Table 5.8 The correspondence between the time of the PES measurements at the ARPES chamber and the time of the I_p measurements at the XPS chamber.

Measuring times (min.)	PES measurements		I_p measurements	
	(at the ARPES chamber)		(at the XPS chamber)	
	Number of scans	Scanning time of each scan (min.)	Number of scans	Scanning time of each scan (min.)
164	200	0.82	9896	0.01657

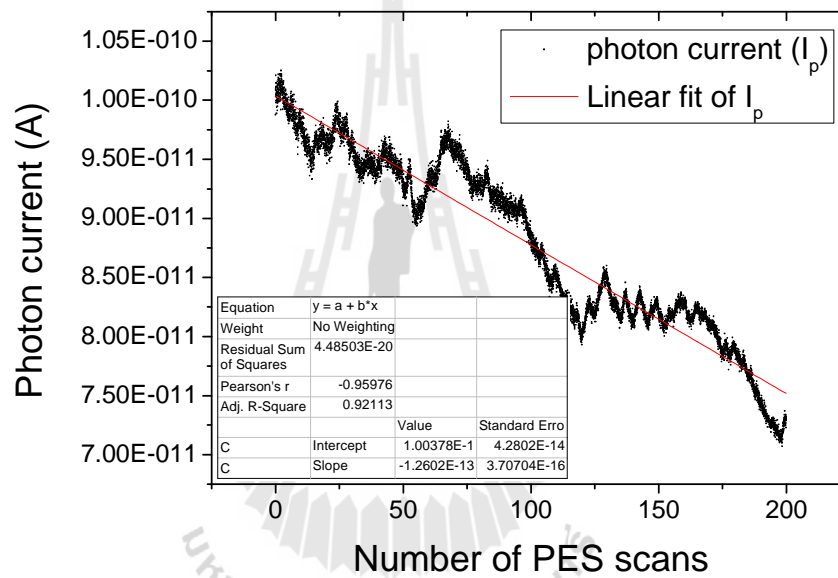


Figure 5.14 Linear fit of I_p with the number of PES scans. Slope as well as vertical intercept has been used to calculate the corresponding I_p for the PES normalization.

Consequently, the corresponding photon currents for each PES measurement can be obtained by this relation,

$$\text{calculated } I_p = \text{vertical intercept} + \frac{\text{slope}}{\text{time of PES measurement}} \quad (5.13)$$

Table 5.9 The corresponding photon currents for the PES intensity normalization.

Number of scan	Time interval in 1 scan	Photon current (A)
1	0.00	1.00×10^{-10}
2	0.82	1.00×10^{-10}
3	1.64	1.00×10^{-10}
4	2.46	1.00×10^{-10}
5	3.28	9.99×10^{-11}
6	4.10	9.98×10^{-11}
7	4.92	9.97×10^{-11}
8	5.74	9.96×10^{-11}
9	6.56	9.95×10^{-11}
10	7.83	9.94×10^{-11}

For example, the I_p for the first 10 PES scans are shown in Table 5.9. Obviously, the I_p for each scan is approximately closed to each others. These quantities are used as the normalization factor for each corresponding PES recorded.

5.6.3 PES spectra and binding energy adjustments

It is well known that binding energy of insulating materials tends to move toward higher binding energy during the PES measurement because of the sample charging effect. This uncontrollable phenomenon originates from the photoelectron accumulation on the surface of insulators and is ascribed to be one of major for the peak identification in the PES measurement.

The practicable method to reduce the charging effect, as described in Section 5.2, is to reduce the incident photon flux by narrowing the slit width that placed in front of the PES sample position. However, this adjustment causes to the decrease in the PES signal-to-noise ratio and also results in the difficulty to identify the PES peaks of the membranes. In addition to correct the charging, the peak positions have been adjusted with respected to the referent position. According to the ultraviolet photoelectron spectroscopy of polytetrafluoroethylene (PTFE) (Ono et al., 2005) and polyvinylidene fluoride (PVDF) (Morikawa et al., 2000), the binding energy of the fluorine 2p state (F_{2p}) appears around 10 eV. However, the binding of F_{2p} in the Nafion membrane can shift from this position. Additionally, the position of F_{2p} depends on the bonding types and the covalent atoms.

For the degraded Nafion, the PES valence band spectra of the membrane, including the F_{2p} and C-O/C-H contaminations, have not been reported. The standard binding energy of F_{2p} is obtained by referring any F_{2p} peaks of each the PES scans to the F_{2p} peaks position of the first PES scan. In this measurement, the resulting first PES scan indicates that the binding energy of the F_{2p} is equal to 10.4 eV. This peak position is in agreement with the results of F_{2p} calculations reported by Bittencourt, Lier, Ke and Suarez-Martinez (2009). After the binding energy adjustments, the corrected peak positions are shown in Figure 5.15.

Because the photon fluences for the VUV irradiations and the PES measurements are similar, the changes of the electronic structures of the degraded Nafion during irradiations can simultaneously be characterized by the PES measurements. As a matter of fact, these changes have been investigated by the PES method.

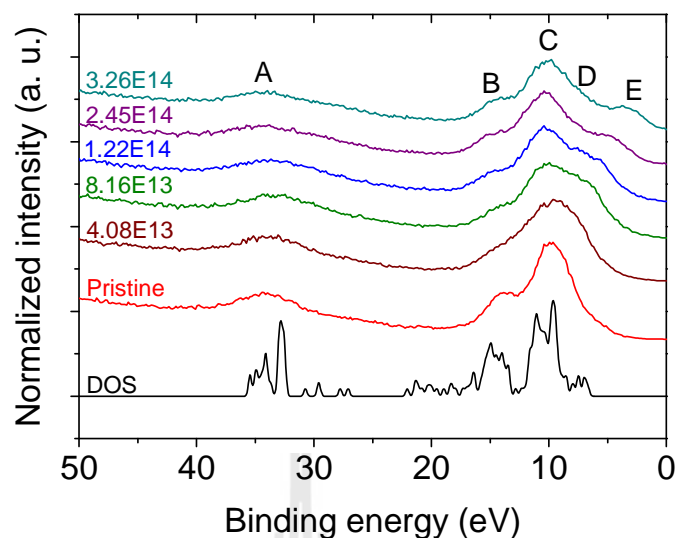


Figure 5.15 PES spectra of the degraded Nafion of the different fluences of VUV irradiations, compared to the DOS result from the DFT calculations. Peak A is assigned to the F_{2s} state, peak B is the C-F band, peak C is the mixing band of the F_{2p} , C-O and C-H, peak D is the C-C band of the Nafion main chain and peak E is the conjugated C=C bond.

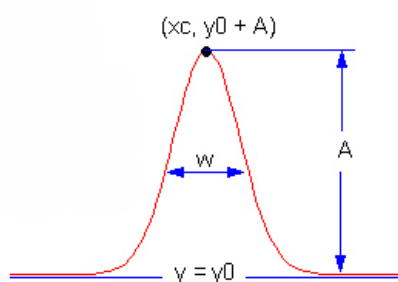


Figure 5.16 Schematic Gaussian fit formula in OriginLab8.5.

Figure 5.15 shows the evolution of the PES spectra of the degraded Nafion membrane. Explicitly, the PES spectra are dramatically changed with the VUV irradiation fluences. The details of the PES peak analysis and the electronic structure calculations of the membrane will be discussed in the next section.

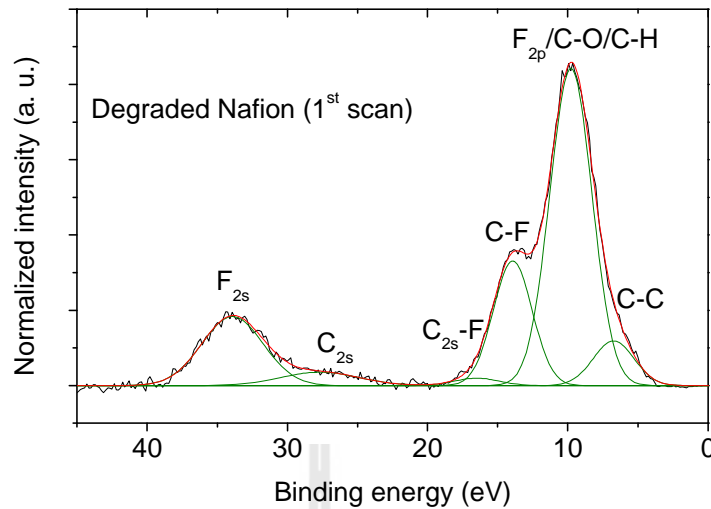


Figure 5.17 The 1st measurement PES spectra of the degraded Nafion.

5.6.4 PES peak analysis

By using the Gaussian fitting method from the peak analyzer module in the OriginLab8.5 computational software, the peaks position of the PES of Nafion can be identified by using the formula of Gaussian fitting is expressed as

$$y = y_0 + \frac{Ae^{-\frac{4 \ln(2)(x-x_c)^2}{w^2}}}{w \sqrt{\frac{\pi}{4 \ln 2}}}, \quad (5.14)$$

where A is the peak altitude, x_c is the peak center position, and w is the peak width as depicted in Figure 5.16.

Figure 5.17 shows the curve fitting of the 1st scan of the PES measurement, which is assigned to be the PES spectra of the pristine (unirradiated) membrane. There are six resonant peaks presented in the PES spectra. According to the valence band spectra of Nafion reported recently, (Ono et al., 2005), (Morikawa et al., 2000) and (Choi, Manohara, Morikawa and Sprunger, 2000), the peak appears at highest binding ($\sim 33\text{eV}$) is originated from F_{2s} .

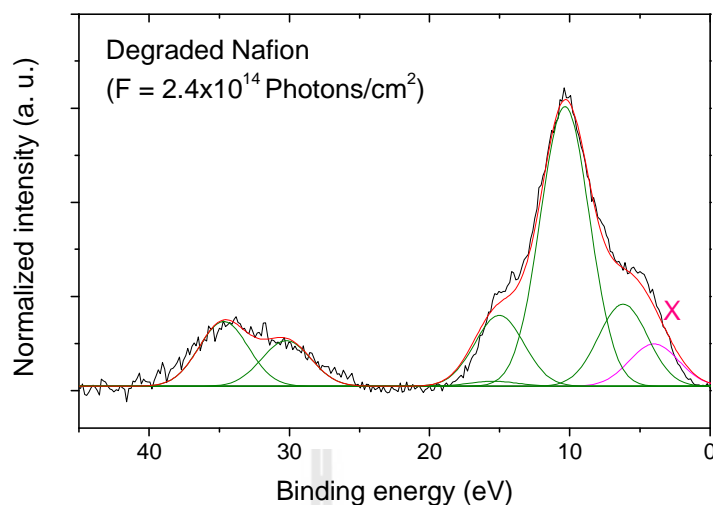


Figure 5.18 PES spectra of the degraded Nafion irradiated with the fluence of 2.4×10^{14} photons/cm². The new peak appears at the lowest occupied state (labeled "X").

The next peak around 28 eV is the C_{2s} orbital from the main chain. The peak at 17 eV is originated from the bonding orbital of C_{2s}-F. The following peak is the C-F bonding interaction. The peak appears at ~ 9-12 eV is the mixing bands of the F_{2p}, C-F, C-C and/or C-H bonds, with the contributions of S and O. It is expected that this mixing band is originated from the remaining surface contaminants by the photo-degradation. And the lone pair of fluorine atom (F_{2p}) and the peak appearing at the lowest binding energy is the bonding orbital of C-C bonds of the main chain and the antibonding orbitals of the C-F bonds.

Additionally, the PES measurements also reveal that upon a subsequent exposure the degraded Nafion membrane to the VUV radiation, a new feature near the Fermi level (labeled "X") is generated as shown in Figure 5.18.

The new peak appears at the lowest binding region of the PES spectra indicates that the chemical structure of Nafion has been changed during the VUV irradiations. This peak is assigned to be the carbon double bonds (C=C). More generally, it is well known in the polymer science that breaking of the C-F and/or C-H bonds may have the generation of carbon-carbon double bonds in polymers.

This structural change also indicates the increment of metallicity of the membrane surface as can be seen in the other photo-excited materials (Ohtomo, Muller, Grazul and Hwang, 2002; Yoshimatsu, Yasuhara, Kumigashira and Oshima, 2008 and Sing et al., 2009).

The generation of C=C bonds provides evidence of a π -bonding band formation in the polymer chain due to the fluorine and or hydrogen removal during the VUV irradiations in vacuum. It is also indicated that with increasing the irradiations fluences, the C=C bond peak exhibits shift to the lower binding energy region and consequently seemed to come across the Fermi level at higher fluences as shown in Figure 5.19.

The generation of the C=C double bonds during irradiations of the degraded Nafion is considered to have the different result from which of the irradiation results of the polytetrafluoroethylene (PTFE) (Ono et al., 2005). Although the backbone chains of Nafion compose of the PTFE chains, PES results shown that the C=C formation is an insignificant degradation mechanism in the PTFE films during the irradiation.

On the other hand, PES results of polyvinylidene fluoride (PVDF) excited with the 75 eV VUV irradiation, reported by E. Morikawa (Morikawa et al., 2000), demonstrated the presence of C=C bonds formation in this polymer.

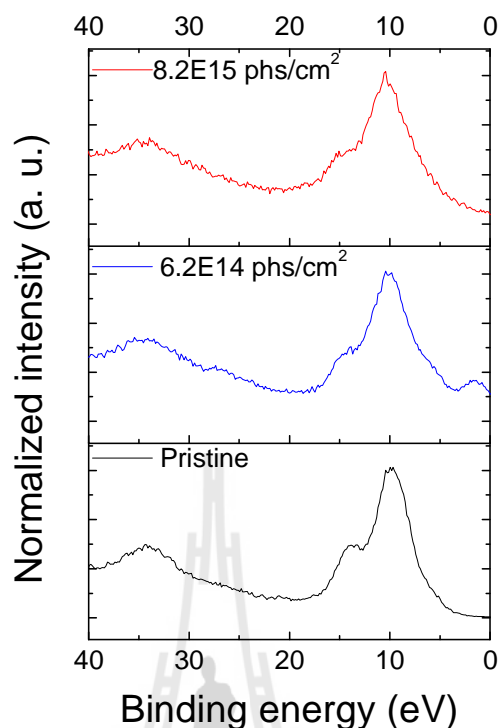


Figure 5.19 The PES spectra of the degraded Nafion induced by VUV irradiations of 0.0, 6.2×10^{14} and 8.2×10^{15} photons/cm². The C=C bonds (peak X) exhibits move toward lower binding energy region with increasing the fluences.

This double offered a way to introduce the formation of fully conjugated double bonds after loss of hydrogen and/or fluorine atoms. Consequently, the reduction of the unit-cell volume of the irradiated polymer was discovered.

In general, the degree of double bond conjugation strongly influences the position of the highest occupied molecular orbital (HOMO) in PES spectra. The higher the degree of conjugation has led to the shift of the HOMO band (thus the threshold energy in PES) toward a lower binding energy. Thus, the PVDF results are almost similar to the PES results in this thesis.

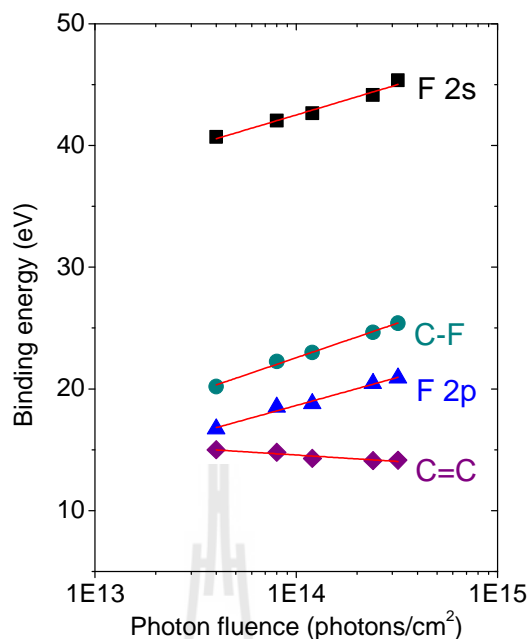


Figure 5.20 Plot the PES peak positions of F_{2s} , C-F, F_{2p} and C=C bonds with the irradiation fluences. The C=C bonds moves toward lower binding energy, while other peaks move toward higher binding energy due to sample charging..

To clarify the shift of the C=C bond upon the VUV fluences, the position of the binding energy of the different components of Nafion (F_{2p} , C-F, F_{2p} and C=C) are plotted as a function of photon fluences, shown in Figure 5.20. Obviously, all peaks except the peak of the C=C bond move toward higher binding energy regions because of the sample charging with increasing in the VUV fluences. On the other hand, the C=C peak moves with the different direction. This indicates that the C=C bond can be used as the indicator for the surface modification without any troubles of the charging effect. Therefore, the shift of the C=C bonds indicates the chemical changes of the Nafion surface during irradiations. This phenomenon is consistent with the other PES reports (Morikawa et al., 2000 and Choi et al., 2000).

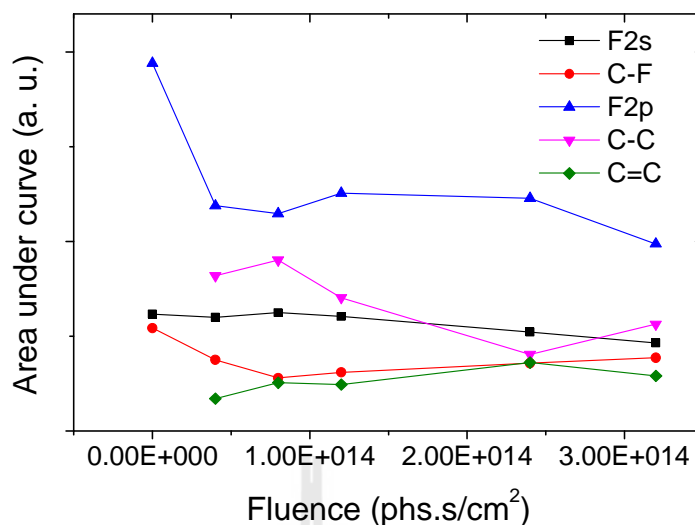


Figure 5.21 Area under curves of the PES measurements of the degraded Nafion. The dramatic decrease in the fluorine peaks indicates the fluorine removal during VUV irradiations.

Moreover, the quantitative analysis (in terms of area under curves) of the peaks can be obtained by using the integrate peak calculation in the OriginLab8.5 computer software. As shown in Figure 5.21, all PES intensities involving the fluorine atoms (F_{2s} , C-F and F_{2p} peaks) are decreased. This indicates the decrease in the fluorine atom with increasing the VUV fluences. Note that the fluorine removal is in agreement with the PES of the PVDF, (Morikawa et al., 2000 and Choi et al., 2000), and also the PES of PTFE (Wheeler et al., 1982). The combined effects of the fluorine and/or contaminants removal and the generation of C=C double bonds with an increasing in the photon fluences demonstrate the chemical changes of the membrane. Since the PES measurement is known to be the surface-sensitive technique, these membrane irradiations are therefore expected to have an effect especially on their surface.

In conclusion, the Nafion surface state evolution excited by the VUV irradiations has been characterized by the PES measurement. It is also suggested that the modifications take responsibility for the PEMFC improvement in terms of the increase in the metallicity, which may increase in the Pt catalyst on the surface, and of the eliminating of the surface contaminants. To observe these structural changes, the fluorine removals have been compared with the results from the theoretical calculations as described in the next section.

5.7 Theoretical Calculation of the Electronic Structure of Nafion

In order to verify the electronic structure of Nafion in the PES measurements, theoretical calculation of the electronic structure have been investigated. As described in Section 4.4, the calculation based on the DFT calculation, which is a quantum mechanical modeling method used in physics and chemistry to study the electronic structure (principally the ground state) of many body systems. For Nafion, the determination of the chemical structure plays an important role for the DFT calculation where the chemical bonds and chain structures serve as the input parameters for this calculation.

As described in Section 3.1, the molecular structure of Nafion consists of the Teflon backbone chains and the sulfonic group terminated at the side chain. The Nafion molecule is illustrated in Figure 2.3. The backbones of the Nafion membranes contain 5-13 groups of the CF_2 , which represent the different peak positions in the DFT calculations. On the other hand, the side chain of Nafion is fixed to have double ether perfluoro side chains as shown in Figure 5.22.

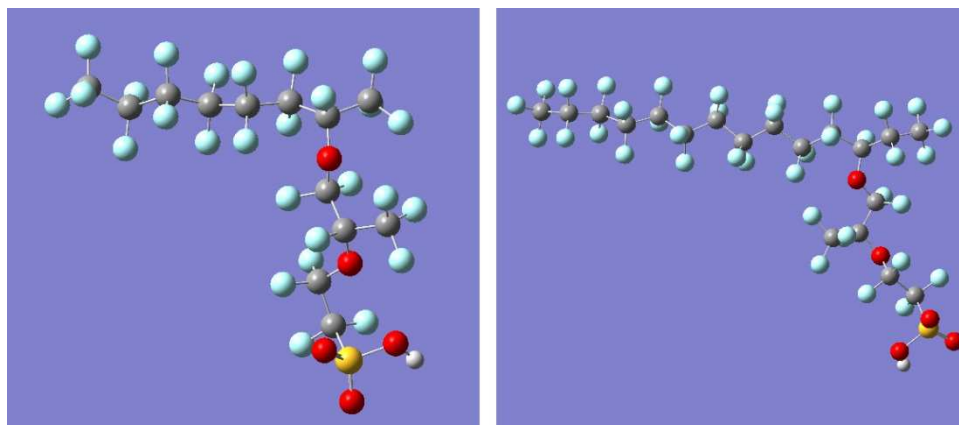


Figure 5.22 Nafion chemical structure for $m = 5$ (left) and $m = 10$ (right) after optimization.

In the DFT calculations, the Gaussian03W computational calculation employs the B3LYP exchange-correlation functional and 6-31G basis set. Two different Nafion backbones structure have been considered in order to examine the electron density of state (DOS) of each molecule. The membrane geometry optimization have been taken with the parameter $m = 5$ and 10. It is important to notes that the optimization is one of the jobs providing in the Gaussian. Optimization means that the calculation will be repeated for different locations of the atomic nuclei until no force acts on the atoms, that is the optimal, minimum energy configuration of the atoms is found. Once calculation, the nuclei are moved according to the forces acting on them. Such an optimization needs to be carried out to determine the optimal bond lengths (and angles in larger molecules).

After the DFT geometry optimization, the DOS of Nafion is extracted by using the Gausssum2.0 computer integration program. The results indicate the different in the DOS of these two different backbones of Nafion, as shown in Figure 5.23.

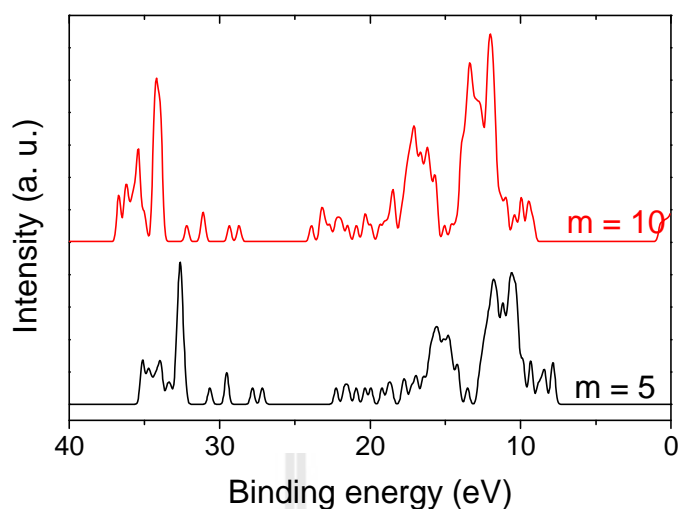


Figure 5.23 The electron density of state (DOS) of the two different chemical structure ($m = 5$ and 10).

Obviously, there are also two different peak positions between them. The binding energy of F_{2p} of the long chain appears at 10.58 eV which closes to the F_{2p} binding energy in the PES measurements, while the short chain appears at 12.0 eV. This calculation implies that the binding energy depends on the concentration of atoms in the membrane (or in term of the number of m).

Moreover, there is an additional difficulty for determining the reference peak position from the DFT calculation. Since the calculations have been accomplished within only one unit of the Nafion molecules due to the limitation of the memory requirement of the program, only one unit of molecular calculation in this thesis differs from the actual units of molecule of Nafion ($n \sim 1000$). It is also evident that the difficulty of finding the referent peak position arises from the discrepancies of the DFT calculations. In fact, the degraded Nafion membranes have the surface contamination. The remaining contaminants can adversely affect the valence band structure by altering the PES peak positions.

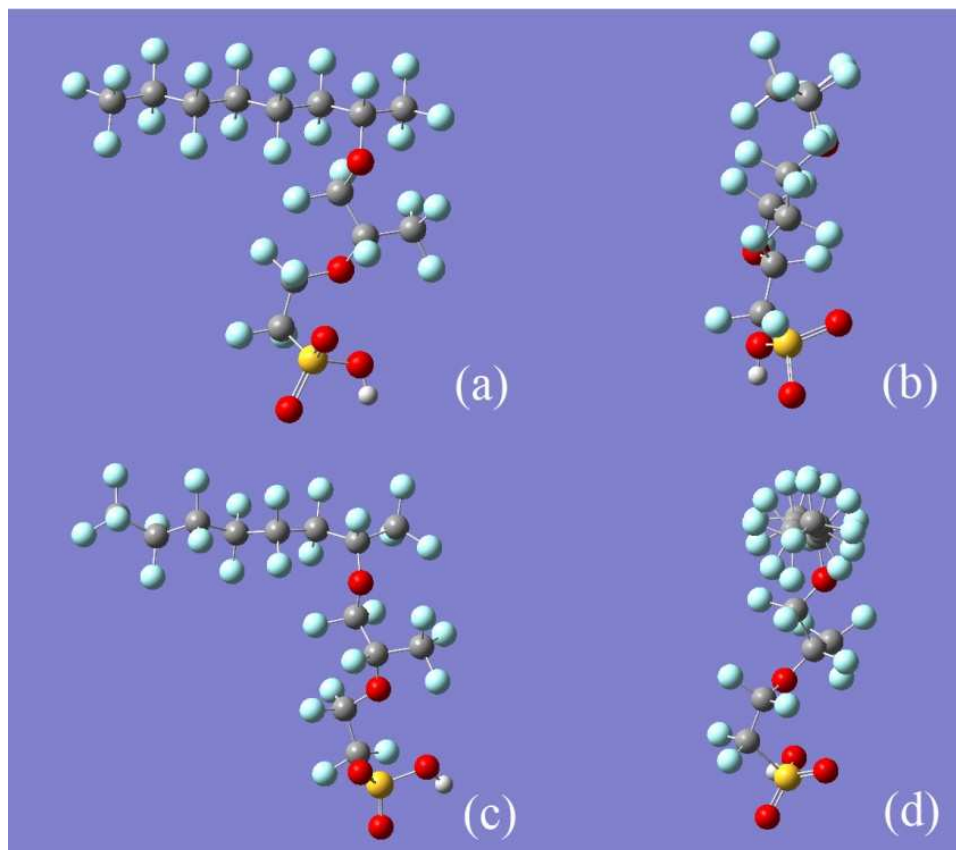


Figure 5.24 The chemical structure of Nafion ($m = 5$) provided by the DFT calculation with, (a) side-view and (b) front-view of Nafion before optimization, (c) side-view and (d) front-view of Nafion after optimization.

Thus, the right referent peak position should be obtained from the PES measurement at the first scan rather than using the DFT calculation because the exact number of atoms in the degraded Nafion molecules is still ambiguous. For this purpose, the DFT calculations have only been used to verify the changes in the chemical structure with the irradiation fluences in term of the density of state of the Nafion membranes.

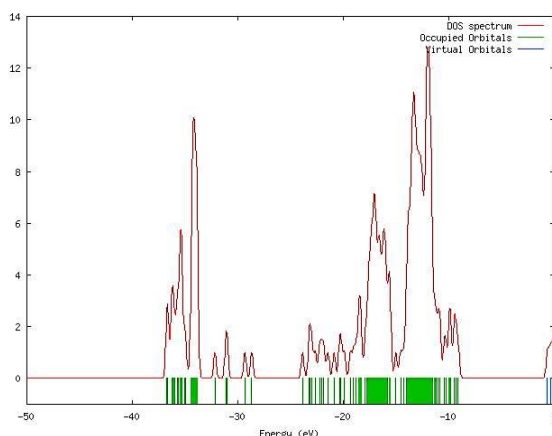


Figure 5.25 The DOS spectra extracted from the DFT calculation of the Nafion membrane. The DOS result is similar to that result shown in Figure 5.23.

5.7.1 DFT analysis

To investigate the electronic structure of Nafion during irradiation, the PES results have been compared with the results from the theoretical calculations. As described in the DFT calculation, the calculation has been accomplished by using modern computational software simulation named Gaussian03W. It provides the powerful tools for chemistry, engineering, physics and material science such as molecular geometry and electronic structure optimization. Figure 5.24 shows the molecular structures of Nafion before and after optimizations.

It is clearly that the Nafion structures have been changed after optimization. While the DOS result is shown in Figure 5.25. Furthermore, the changes of the electron density of state of Nafion after VUV irradiation can be examined by the DFT calculations. By removing the fluorine atoms from the Nafion membrane, the DOS spectra have been changed.

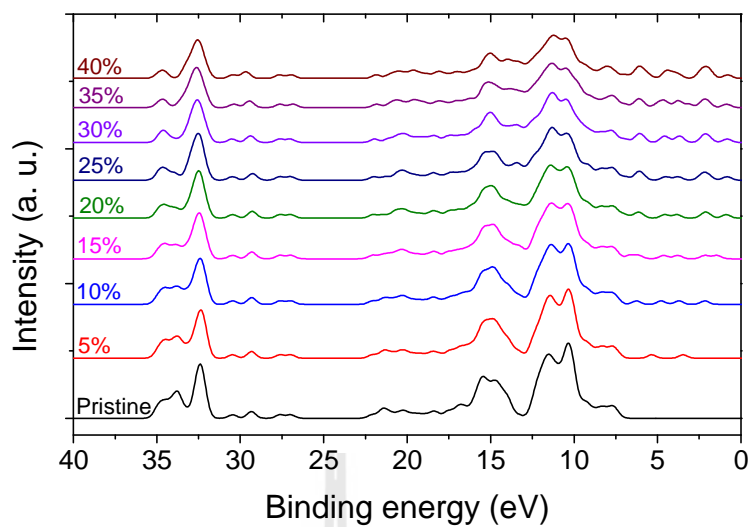


Figure 5.26 The DOS spectra of the Nafion membranes. The calculations are performed by removing the fluorine atoms from 0 to 40% of a single Nafion molecule.

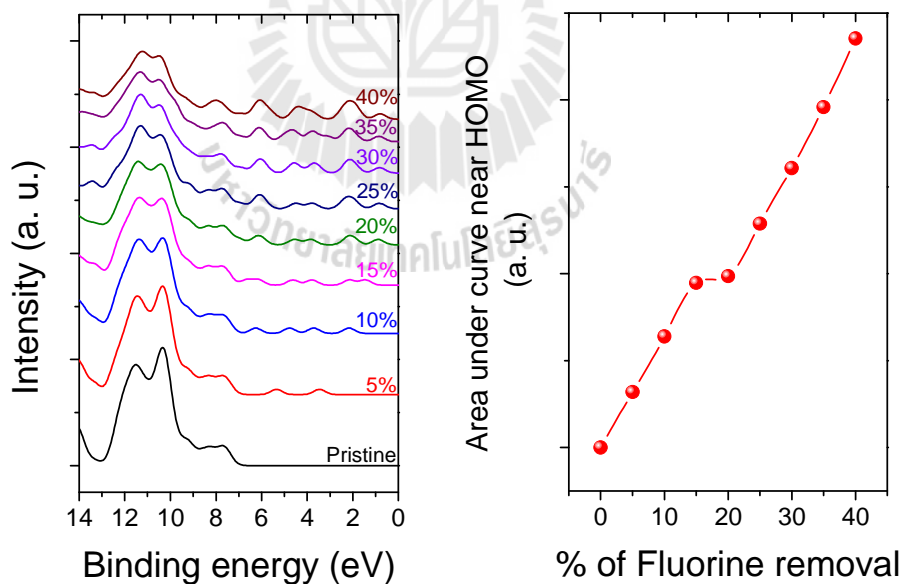


Figure 5.27 DOS spectra of Nafion near HOMO region and the integrated peak intensity near HOMO, which contained the C=C bands. The area under peak is linearly increased with the degree of the fluorine removal.

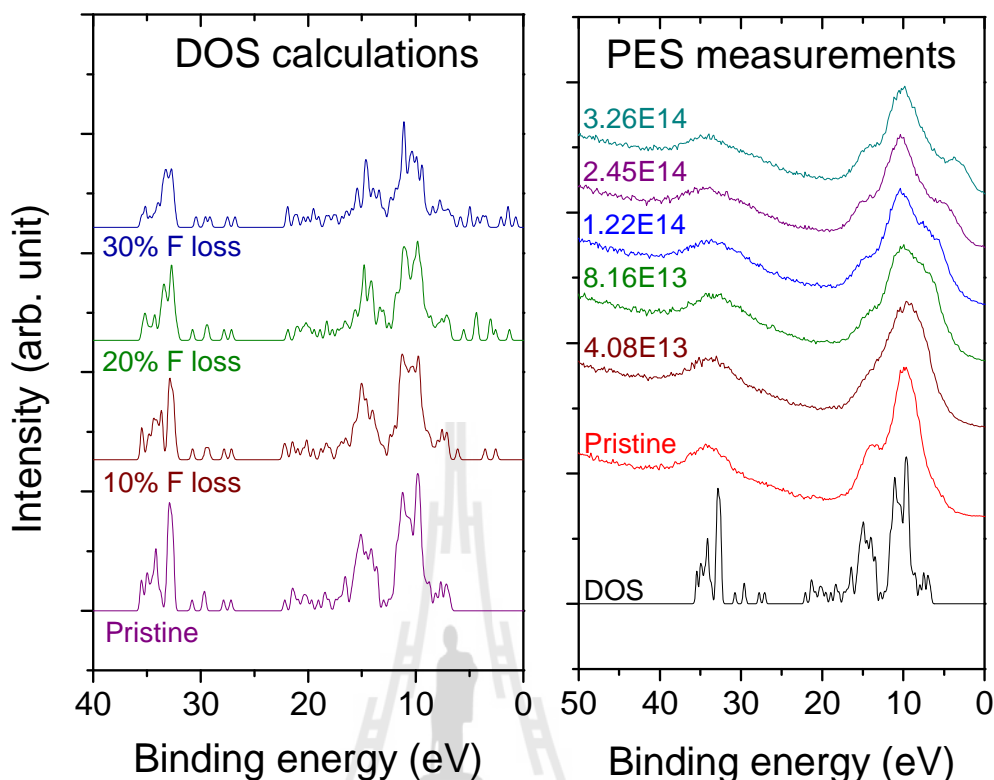


Figure 5.28 Comparisons between DOS spectra of the different degree of the fluorine removal (0-30%) and the PES spectra of Nafion during VUV irradiations.

More specifically, the intensity of the DOS of the C=C bands is increased with the degree of the fluorine removals. Figure 5.26 illustrates the DOS spectra of the Nafion membrane upon the degree of the fluorine removal from the backbone and the side chains using the ground state calculations. And the changes of the electronic structure near the HOMO region of Nafion have been summarized in terms of the peak intensity as shown in Figure 5.27. These calculations show that the C=C bands formation arises from the loss of the fluorine atoms without any reactions of the surrounding reactive species as occurred in the polymer photo-degradation.

It is suggested that the Nafion molecules have been rearranged to a new stable form containing the C=C bonds after the fluorine removal. Figure 5.28 shows the electronic structural changes of the calculated DOS of Nafion, in comparison with the PES spectra of the irradiated Nafion membranes. When the fluorine atoms have been removed from Nafion surface (10-30%), the calculated DOS spectra indicates the reliable decrease in the fluorine peaks (in both F_{2s} and F_{2p}). Interestingly, DOS spectra of the fluorine removal also show the generation of new peak near the HOMO. This new peak during irradiation is indeed the C=C double bonds formation.

In this comparison, because the VUV irradiations are performed in the UHV system where the reaction of the surrounding reactive species is inconsequential to the rearrangement of the irradiated membrane, the molecular system of Nafion are then reorganized to have the minimum energy when they loss the fluorine atoms. Therefore, the C=C band is arisen after the fluorine removal in the PES measurement and also the VUV irradiations.

Explicitly, the DOS calculations agree very well with the PES results and also correspond to the similar set of the photon fluences of the VUV irradiations as described in the previous section. Consequently, the surface of the degraded Nafion membranes has been modified by the VUV irradiations. The followed fuel cell performance test of the modified membrane is considered to exhibit better power density than the fuel cell using the degraded membrane.

CHAPTER VI

SUMMARY

This thesis focuses on the surface modification of the degraded Nafion membrane, which undergoes the photo-oxidation of air under UV and visible light activation. The reaction is known to be the major reaction in the photo-degradation of many polymer materials. For Nafion, the degradation causes to the reduction of the membrane conductivity and durability and subsequently lowering the PEMFCs performance. Although the degraded or contaminated parts of the membrane can generally be removed by the chemical cleaning methods, it is difficult to remove some permanent species such as the oxygen containing species. Furthermore, the disposal of the degraded membrane has an environmental issue because the main component of Nafion is the fluorine compound. Spreading this element without chemical managements has led to the environment impacts. For example, fluoride in drinking water is known for both beneficial and detrimental effects on health. Fluorosis - a disease caused by ingestion of fluoride in excess through water, food and air and is a serious health problem (Nagendra Rao, 2003). For these reasons, recovering of the degraded Nafion membrane plays an essential role for the membrane managements in order to solve the environment problems by reducing the replacement of the new membrane. Moreover, the modified membrane may improve the fuel cell performance, resulting in the reduction of the cost of the fuel cell materials.

Although UV radiation amounts to only 3% of the total radiations that reaching on earth, it's energetic enough to introduce chemical reactions and weathering of polymers (Massey, 2007). Therefore, the exposure of the degraded membrane to UV radiation in an ultrahigh vacuum without oxygen reaction is an interesting method for the membrane surface modification. This UV process is supposed to be the same process of the photo-degradation and being the suitable surface modification technique. More specifically, the degraded membranes are exposed to various photon fluences ($0.0-3.2 \times 10^{14}$ photons/cm²) (100 eV) of the vacuum ultraviolet (VUV) from the synchrotron radiation. The consequences of the VUV irradiations have also been satisfied by several characterization techniques (PES, SAXS, AFM and mass spectrometry) and the PEMFC performance has been verified by a single PEMFC performance test system. Moreover, the surface modification effects of VUV irradiations have been compared with the surface modification effects excited by various Ar⁺ energies (0.0-3.0 keV) and the zero-order synchrotron radiation.

The topic initiation is the establishment of the degraded Nafion membrane by the photo-oxidation reaction. More specifically, the membranes were degraded in different weather conditions for a long period of time (2 years). In essence, weathering is the natural tendency of materials to return (corrode, oxidize, chalk, permeate, delaminate, depolymerize, flex crack, discolor, etc.) to their elemental forms. Thus, the membranes have undergone photo-degradation, as observe in the yellowish discoloration and the membrane brittleness.

It is expected that this photo-degradation can occur on the membrane surface, which directly affects the interfacial area of the electrolyte membrane and the catalyst and subsequently the lowering in the PEMFC performance. The next step is the membrane treatments by chemical cleans and VUV irradiations. The photon fluences for the VUV irradiations are assigned to have a set of the fluences which cover the threshold fluence. The threshold fluence is calculated from the cylindrical water channels model of Nafion presented by Klaus et al. (2008).

In addition to verify the surface alteration after irradiations, mass spectrometry has been used to display the molecular fragmentation upon the VUV irradiation, zero-order synchrotron irradiation and Ar⁺ sputtering. The surface effect of Ar⁺ sputtering and VUV irradiation are compared with the mass spectrometry results. The mass spectra show that the Ar⁺ sputtering has an excessive effect on the membrane surface compared to each other. In contrast, the ions interaction with the membrane is very large. This means that the ion beam induces an extremely high-density excitation as shown in the AFM images and the mass spectrometry.

The molecular fragmentations induced by Ar⁺ sputtering contain the CF, CF₂ and CF₃ fragments, which are extracted from the main components of the Nafion backbones and also contain SO₃H from the Nafion side chains. Consequently, the membranes suffer from the chain scission and the reduction of the mechanical strength. Thus, using Ar⁺ bombardment is an inappropriate technique for the surface modification of the degraded Nafion. On the other hand, the mass spectra induced by the VUV irradiation show the different surface effect. Unlike the Ar⁺ sputtering, the VUV irradiation behaves a mildly surface modification for the Nafion.

Only minute Nafion fragments have been detected during the VUV irradiations, implying that the backbone chains of Nafion have not been cleaved after irradiations. For this reason, the mechanical structure of the membrane has not been reduced in this irradiation. Moreover, the surface of Nafion has only been modified by VUV irradiations without any chain scission in the polymer. The effective effect of the VUV irradiations is supposed to be the structural modification in the membrane surface. This effect involves the change of the electrochemical reaction rate at the interface between the electrolyte membrane and the catalyst. However, the bulk structure of Nafion should be verified before the surface characterization.

Interestingly, the shift of the ionomer peak of the hydrated membrane toward lower scattering vector indicates that the ionic aggregation of the irradiated membrane is expanded. The degree of expansion of the irradiated membrane eventually is higher than that of the non-irradiated membrane. The expansion offers the possibility to build up the interconnecting water channels. This phenomenon is a significant factor for understanding the PEMFC improvement because the ionic expansion strongly depends on the ability to swollen water and increase in the water channel connection in the membrane, resulting in the increase in the proton conductivity of the membrane.

Although the proton conductivity depends on the nanochannels ionic aggregation inside the membrane, the modification of the surface structure bears high PEMFC performance because the fuel cell electrochemical reactions take place at the surface boundary of the electrolyte membrane and the catalyst electrodes. Therefore this thesis focuses on the surface changes of the Nafion membranes after irradiations rather than the bulk membranes.

In order to examine the membranes ability after irradiations, the PEMFC performance test station has been conducted. The PEMFC performance, which is expressed in terms of the fuel cell polarization curve (J-V), shows that both one-side and two-side VUV irradiations exhibit high current density with the irradiation fluences. This result also shows the enhancement of the PEMFC performance when using the irradiated membranes.

By using the two-side irradiated membrane taken with the fluence of 2.4×10^{14} photons/cm², the PEMFC possesses the maximum power density (0.28 W/cm²). By comparing with the non-irradiated and the one-side irradiated membranes at the same current density (0.2 A/cm²), the power density of the two-side irradiated membrane increases ~ 47% compared to the power density of the non-irradiated membrane and 13% higher than that of the one-side irradiation. Therefore, the higher power density of the two-side irradiated membrane confirms that the surface of the degraded membrane has been modified by the VUV irradiations.

The possible effects in the surface modification are the fluorine removal and/or the elimination of the surface contaminants such as C=O and C-H bonds, which may deposit on the membrane in the photo-oxidation reaction. Eliminating the surface degraded components has led to the enhancement of the proton conductivity. This process is possibly called the VUV surface cleaning process. Although the UV irradiations have been largely applied in the radiation chemistry, the membrane surface modification by VUV irradiations in UHV systems is an unprecedented method. Alternatively, the mass spectrometry and SAXS studies have been confirmed the gently surface effects to the membrane after irradiations.

As of now, the surface electronic structures of the irradiated membrane have been characterized by means of the PES. From an adjustable synchrotron source, the evolution of the surface state in the valence band electronic structure of the degraded membranes during VUV irradiations can be characterized. The PES results show the dramatic decrease of the F_{2p} spectra and the generation of the new peak near the Fermi level with higher fluences irradiations.

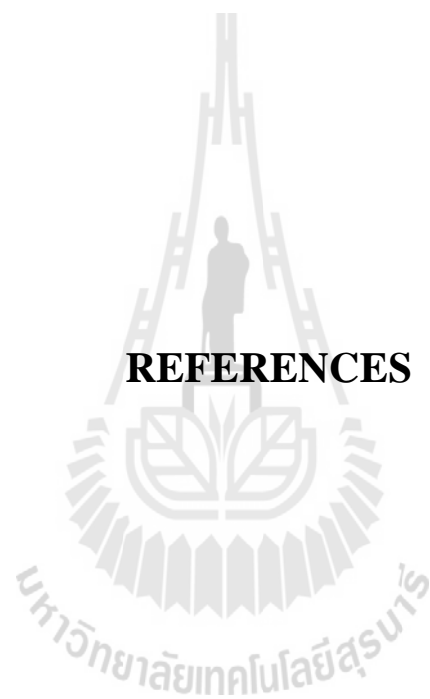
This peak is assigned to be the carbon double bond formation (C=C). The appearance of the C=C bond indicates the reduction of the fluorine concentration in the Nafion backbones during VUV irradiations. Additionally, it is suggested that the C-C bond in the membrane transforms to the C=C double bond without any chain scissions as occur in other severe modifications technique such as the ion bombardments, gamma and the zero-order synchrotron irradiations. In vacuum, on the other hand, no reactive atoms such as oxygen or hydrogen associate the fluorine vacancy sites after fluorine removal. Therefore, the main chains of the polymer have not been broken after the VUV irradiations. The main structural change in the irradiated membrane is indeed the fluorine removal, the elimination of the surface contaminants and the C=C double bonds. These results are compared with the DFT calculations.

Moreover, the subsequently modification is the side effect of the chain transformation from the C-C bonds to the C=C bonds, which is the stable bonds formation and the reactive species cannot activate to this stable form. This mean the polymer have the stable form after VUV irradiations and directly results in the improvement of the membrane mechanical stability.

Interestingly, the binding energy of the double bonds formation shifts toward lower binding energy region with the irradiation fluences. This structural change indicates the increment of the membrane metallicity (Diat and Gebel, 2008 and Choi et al., 2000). Due to the high surface metallicity of the modified membranes, it turns out that increasing in the metallicity results in the capability to contain more the Pt catalyst on the membrane surface. However, this phenomenon still not being clear and needs some further researches.

Consequently, the VUV irradiation of the degraded membranes is an appropriated method for the improvement of the surface of the membrane. Because the hydrogen oxidation reaction and the oxygen reduction reaction in the fuel cell operation take place at the interface between an electrode and an electrolyte, the improvement in the membrane-electrodes interface, via the membrane surface modifications, plays a crucial role for increasing the electrochemical reaction and also improves the performance in PEMFC.

For the degraded Nafion membrane, the VUV irradiations have an effect to the surface by changing the surface state and consequently result in the elimination of the membrane contaminants from the photo-degradation mechanisms. Finally, this thesis summarizes that the degraded Nafion surface can be modified by the VUV synchrotron irradiations in the UHV system. This synchrotron irradiation technique suggests an avenue for the improvement of the performance of the PEMFC and also for the future energy developments.



REFERENCES

REFERENCES

- Arico, A. S., Srinivasan, S. and Antonucci, V. (2001). DMFCs: From fundamental aspects to technology development. **Fuel Cells** 1(2): 133-161.
- Asano, M., Chen, J., Maekawa, Y., Sakamura, T., Kubota, H. and Yoshida, M. (2007). Novel UV-induced photografting process for preparing Poly(tetrafluoroethylene)-based proton-conducting membranes. **J. Polym. Sci. Pol. Chem.** 45: 2624-2637.
- Atkins, P. and Friedman, R. (2005). **Molecular Quantum Mechanics**. New York: Oxford University Press Inc.
- Atkins, R. W. (1998). **Physical Chemistry**. New York: Oxford University Press Inc.
- Barbi, V., Funari, S. S., Gehrke, R., Scharnagl, N. and Stribeck, N. (2003). Nanostructure of Nafion membrane material as a function of mechanical load studied by SAXS. **Polymer** 44: 4853-4861.
- Barbir, F. (2005). **PEM Fuel Cells: Theory and Practice**. California: Elsevier Academic Press.
- Barbir, F., Braun, J. and Neutzler, J. (1999). Properties of moded graphite bi-polar plates for PEM fuel cells. **Int. J. New Mater. Electrochem. Sys.** 197-200.
- Bard, A. and Faulkner, L. R. (1980). **Electrochemical Methods**. Chichester: John Wiley & Sons.
- Becke, A. D. (1998). Density-functional exchange-energy approximation with correct asymptotic behavior. **Phys. Rev. A.** 38: 3098-3100.

- Becke, A. D. (1993). Density-functional thermochemistry. III. The role of exact exchange. **J. Chem. Phys.** 98: 5648-5652.
- Biello, D. (2009). **How to Use Solar Energy at Night** [On-line]. Available: <http://www.scientificamerican.com/article.cfm?id=how-to-use-solar-energy-at-night>.
- Bittencourt, C., Lier, G. V., Ke, X. and Suarez-Martinez, I. (2009). Spectroscopy and defect identification for fluorinated carbon nanotubes. **Chem. Phys. Chem.** 10: 920-925.
- Bockris, J. O. and Srinivasan, S. (1969). **Fuel Cells: Their Electrochemistry**. New York: McGraw-Hill.
- BP P.L.C. (2011). **BP Statistical Review of World Energy June 2011** [On-line]. Available: <http://www.bp.com/statisticalreview>.
- CAPA Center for Activation (2011). **Airline Shares Down 12% in 2011; 1Q Net Losses Similar to 2010 on Rising Fuel** [On-line]. Available: <http://www.centreforaviation.com/analysis/airline-shares-down-12-in-2011-1q-net-losses-similar-to-2010-on-rising-fuel-54886>.
- Cave, C. (1998). **The Ecology of Dams** [On-line]. Available: <http://chamisa.freeshell.org/dam.htm>.
- Cho, S., Cho, E., Oh, I.-H., Kim, H.-J. and Ha, H. (2006). Surface modified Nafion[®] membrane by ion beam bombardment for fuel cell applications. **J. Power Sources** 155: 286-290.

- Choi, J., Manohara, H. M., Morikawa, E. and Sprunger, P. T. (2000). Thin crystalline functional group copolymer poly(vinylidene fluoride–trifluoroethylene) film patterning using synchrotron radiation. **Appl. Phys. Lett.** 76(3): 381-383.
- Czvikovszky, T. (2004). Radiation-assisted compatibilization of polymer. **Advances in radiation chemistry polymers** (pp. 61-74). Vienna: International Atomic Energy Agency.
- Daily Kos. (2011). Fukushima Nuclear Power Plant Maybe Getting Worse. [On-line]. Available: <http://www.dailykos.com/story/2011/03/14/955762/-Fukushima-Nuclear-Power-Plant-May-Be-Getting-Worse>.
- Danilczuk, M., Perkowski, A. J. and Schlick, S. (2010). Ranking the stability of perfluorinated membranes used in fuel cells to attack by hydroxyl radicals and the effect of Ce(III): A competitive kinetics approach based on spin trapping ESR. **Macromolecules** Article in press.
- Diat, O. and Gebel, G. (2008). Fuel cell proton channels. **Nat. Matter.** 7: 13-14.
- Dong, F. (2007). **Food Security and Biofuels Development: The Case of China** [On-line]. Available: <http://www.card.iastate.edu/publications/synopsis.aspx?id=1060>.
- Fadley, C. S. (1978). Basic Concepts of X-ray Photoelectron Spectroscopy. In C. R. Brundle, **Electron Spectroscopy: Theory, Techniques and Applications** (pp. 2-156). London: Academic Press.
- Francisco, A.-M., Cabot, P. L. and Brillas, E. (2007). Technical H₂ Electrodes for Low Temperature Fuel Cells. In L. O. Vasquez, **Fuel Cell Research Trends** (pp. 247-272). New York: Nova Science Publishers, Inc.

- Gierke, T. D., Munn, G. E. and Wilson, F. C. (1981). The morphology in Nafion perfluorinated membrane products, as determined by wide- and small-angle X-ray studies. **J. Polym. Sci. Polym. Phys. Edn.** 19: 1687-1704.
- Gold, J. (2011). Waste Heat Recovery: The Next Wave of Clean Tech [On-line]. Available: <http://www.tappi.org/content/eneletters/ahead/2011/issues/2011-08-24.html>.
- Grioni, M. (2006). Photoelectron Spectroscopy. In F. Hippert, **Neutron and X-ray Spectroscopy**. (pp. 189-237). Dordrecht: Springer.
- Hancock, P. and Skinner, B. J. (2000). **Chemistry of Geothermal Waters and Hydrothermal Alteration** [On-line]. Available: <http://www.encyclopedia.com/doc/1O112-chemistryofgeothermalwatersandhydrothermalalteration.html>.
- Hüfner, S. (2003). **Photoelectron Spectroscopy: Principles and Applications**. Berlin: Springer.
- International Atomic Energy Agency (2012). **Operational & Long-Term Shutdown Reactors** [On-line]. Available: <http://pris.iaea.org/Public/WorldStatistics/OperationalReactorsByCountry.aspx>.
- Ioselevich, A. S., Kornyshev, A. A. and Steinke, J. H. (2004). Fine morphology of proton-conducting ionomers. **J. Phys. Chem. B.** 108: 11953-11963.
- Ismail, A. F., Naim, R. and Zubir, N. A. (2009) Fuel Cell Technology Review. In Zaidi, S.M.J. and T. Matsuura, **Polymer Membranes for Fuel Cells** (p. 27). New York: Springer Science & Business Media.
- Kim, J., S-M., L., Srinivasan, S. and E., C. C. (1995). Modeling of proton exchange fuel cell performance with an empirical equation. **J. Electrochem. Soc.** 2670-2674.

- Klaus, S.-R. and Chen, Q. (2008). Parallel cylindrical water nanochannels in Nafion fuel-cell membranes. **Nat. Mater.** 7: 75-83.
- Kordesch, K. and Simader, G. (1996). **Fuel Cells and Their Applications**. New York: VCH Publishers.
- Koven, C. D., Ringeval, B., Friedlingstein, P., Ciais, P., Cadule, P., Khvorostyanov, D., Krinner, G. and Tarnocai, C. (2011). Permafrost carbon-climate feedbacks accelerate global warming. **Proc. Natl. Acad. Sci. U.S.A.** Article in press.
- Krivandin, A. V., Glagolev, N. N., Shatalova, O. V. and Kotova, S. L. (2003). Structure alterations of perfluorinated sulfocationic membranes under the action of ethylene glycol (SAXS and WAXS studies). **Polymer** 44: 5789-5796.
- Larminie, J. and Dick, A. (2003). **Fuel Cell Systems Explained**. John Wiley & Sons.
- Lee, C., Yang, W. and Parr, R. G. (1988). Development of the colle-salvetti correlation-energy formula into a functional of the electron density. **Phys. Rev. B.** 37: 785-789.
- Lee, K., Jockusch, S., Turro, N. J., French, R. H., Wheland, R. C., Lemon, M. F., Braun, A. M., Widerschpan, T., Dixon, D. A., Li, J., Ivan, M., and Zimmerman, P. (2005). 157 nm Pellicles (Thin Films) for photolithography: Mechanistic investigation of the VUV and UV-C photolysis of fluorocarbons. **J. Am. Chem. Soc.** 127: 8320-8327.
- Massey, L. K. (2007). **The Effects of UV Light and Weather on Plastics and Elastomers**. New York: William Andrew, Inc.

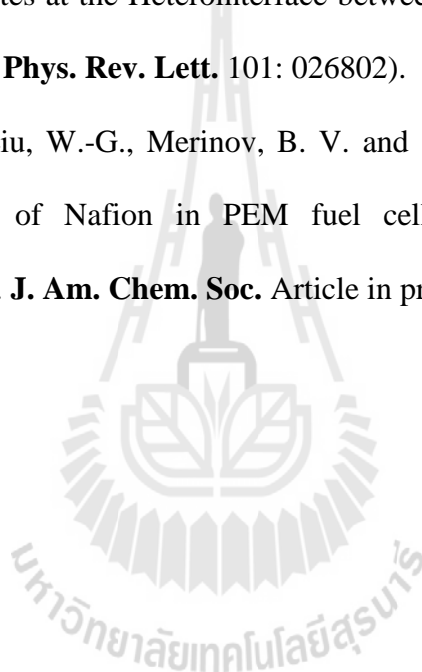
- Mauritz, K. A. and Moore, R. B. (2004). State of understanding of Nafion. **Chem. Rev.** 104: 4535-4585.
- Mecadi. **Permeation & Polymers** [On-line]. Available: http://www.mecadi.com/en/literature_tools/encyclopedia/categorial/Ionomer/Nafion_copolymer_made_from_PTFE_and_perflourinate.
- Meevasana, W., King, P. D., He, R. H., Mo, S.-K., Hashimoto, M., Tamai, A., Songsiriritthigul, P., Baumberger, F., and Shen, Z.-X. (2011). Creation and control of a two-dimensional electron liquid at the bare SrTiO₃ surface. **Nat. Matter.** 10: 114-118.
- Montaudo, G. and Lattimer, R. P. (2002). **Mass Spectrometry of Polymers**. Florida: CRC Press LLC.
- Morikawa, E., Choi, J., Manohara, H. M., Ishii, H., Seki, K., Okudaira, K. K. and Ueno, N. (2000). Photoemission study of direct photomicro machining in poly(vinylidene fluoride). **J. Appl. Phys.** 87(8): 4010-4016.
- Nagendra, R. C. (2003). Fluoride and Environment - A Review. In **Proceedings of the Third International Conference on Environment and Health**, (pp. 386-399.). Chennai.
- Odgaard, M. (2005). The use of Nafion[®] as electrolyte in fuel cells. In T. Nakajima and H. Groult, **Fluorinated Materials for Energy Conversion** (pp. 439-468). Amsterdam: Elsevier Ltd.
- O'Hagan, D. (2008). Understanding organofluorine chemistry: An introduction to the C-F bond. **Chem. Soc. Rev.** 37: 308-319.

- Ohtomo, A., Muller, D. A., Grazul, J. L. and Hwang, H. Y. (2002). Artificial charge-modulation in atomic-scale perovskite titanate superlattices. **Nature** 419: 378-380.
- Ono, M., Yamane, B., Fukagawa, H., Kera, S., Yoshimura, D., Okudaira, K. K., Morikawa, E., Seki, K. and Ueno, N. (2005). UPS study of VUV-photodegradation of polytetrafluoroethylene (PTFE) ultrathin film by using synchrotron radiation. **Nucl. Instrum. Meth. B.** 236: 377-382.
- Ono, M., Yamane, H., Fukagawa, H., Kera, S., Yoshimura, D., Morikawa, E., Seki, K. and Ueno, N. Possibility of the Fermi level control by VUV-induced doping of an organic thin film: Polytetrafluoroethylene. **IPAP Conf. Series** 6 (pp. 27-30).
- Page, K. A., Landis, F. A., Phillips, A. K. and Moore, R. B. (2006). SAXS analysis of the thermal relaxation of anisotropic morphologies in oriented Nafion membranes. **Macromolecules** 39: 3939-3946.
- Ramdutt, D., Charles, C., Hudspeth, D., Ladewig, B., Gengenbach, T., Boswell, R., Dicks, A. and Brault, P. (2007). Low energy plasma treatment of Nafion[®] membranes for PEM fuel cells. **J. Power Sources** 165: 41-48.
- Rasoul, F. A., Hill, D. J., George, G. J. and O'Donnell, J. H. (1998). A Study of a simulated low earth environment on the degradation of FEP polymer. **Polym. Advan. Technol.** 9: 24-30.
- Rikukawa, R. and Sanui, K. (2000). Proton-conducting polymer electrolyte membranes based on hydrocarbon polymers. **Prog. Polym. Sci.** 25: 1463-1502.

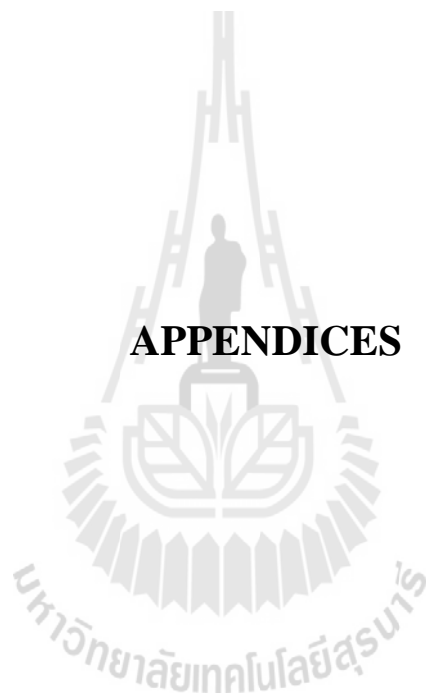
- Roche, E. J., Pineri, M., Duplessix, R. and Levelut, A. M. (1981). Small-angle scattering studies of Nafion membranes. **J. Polym. Sci. Polym. Phys. Edn.** 19: 1-11.
- Rogers, S. and Evans, L. (2011). **World Carbon Dioxide Emissions Data by Country: China Speeds Ahead of the Rest** [On-line]. Available: <http://www.guardian.co.uk/news/datablog/2011/jan/31/world-carbon-dioxide-emissions-country-data-co2>.
- Rubatat, L., Rollet, A.-L., Gebel, G. and Diat, O. (2002). Evidence of elongated polymeric aggregates in Nafion. **Macromolecules** 35: 4050-4055.
- Savadogo, O. (1998). Emerging membranes for electrochemical systems: (I) Solid polymer electrolyte membranes for fuel cell systems. **J. New Mater. Electrochem. Syst.** 1(1): 47-66.
- Schulze, M., Lorenz, M., Wagner, N. and Gülzow, E. (1999). XPS analysis of the degradation of Nafion. **Fresenius J. Anal. Chem.** 365: 106-113.
- Sing, M., Berner, G., Gob, K., Muller, A., Ruff, A., Wetscherek, A., Thiel, S., Mannhart, J., Pauli, S. A., Schneider, C. W., Willmott, P. R., Gorgoi, M., Schafers, F. and Claessen, R. (2009). Profiling the interface electron gas of LaAlO₃/SrTiO₃ heterostructures with hard X-ray photoelectron spectroscopy. **Phys. Rev. Lett.** 102: 176805-1.
- Starkweather, H. J. (1982). Crystallinity in perfluorosulfonic acid ionomers and related polymers. **Macromolecules** 15: 320-323.
- Steck, A. E. (1995). Membrane Materials in Fuel Cells. In **First International Symposium on New Materials for Electrochemical Systems**, (pp. 74-79). Montreal.

- Tian, J.-H., Gao, P.-F., Zhang, Z.-Y., Luo, W.-H. and Shan, Z.-Q. (2008). Preparation and performance evaluation of a Nafion-TiO₂ composite membrane for PEMFCs. **Int. J. Hydrogen Energ.** Article in press.
- Tsao, C.-S., Chang, H.-L., Jeng, U.-S., Linc, J.-M. and Lin, T.-L. (2005). SAXS characterization of the Nafion membrane nanostructure modified by radiation cross-linkage. **Polymer** 46: 8430-8437.
- U.S. Nuclear Regulatory Commission. (2011). **Radioactive Waste** [On-line]. Available: <http://www.nrc.gov/waste.html>.
- Wheeler, D. R. and Pepper, S. V. (1982). Effect of X-ray flux on polytetrafluoroethylene in X-ray photoelectron spectroscopy. **J. Vac. Sci. Technol.** 20(2): 226-232.
- World Wind Energy Association. (2011). World Wide Energy Report 2010. In **10th World Wind Energy Conference & Renewable Energy Exhibition** (pp. 1-23). Cairo, Egypt.
- Xie, T. (2010). Tunable polymer multi-shape memory effect. **Nature** 464: 267-270.
- Yamaki, T. (2010). Quantum-beam technology: A versatile tool for developing polymer electrolyte fuel-cell membranes. **J. Power Sources** 195: 5848-5855.
- Yana, J., Lee, V. S., Rattanachai, Y., Songsiriritthigul, P., Medhisuwakul, M., Vannarat, S., Dokmaisrijan, S., Vilaithong, T. and Nimmanpipug, P. (2012). Computational and Experimental Study of Low Energy Ar⁺ Bombardment on Nafion. **Surf. Coat. Tech.** 206: 3607-3613.

- Yang, Y., Sui, A., Peckham, T. J. and Holdcroft, S. (2008). Structural and morphological features of acid-bearing polymers for PEM fuel cells. **Adv. Polym. Sci.** 215: 55-126.
- Young, D. (2001). **Computational Chemistry: A Practical Guide for Applying Techniques to Real World Problems.** New York: John Wiley & Sons.
- Yoshimatsu, K., Yasuhara, R., Kumigashira, H. and Oshima, M. (2008). Origin of Metallic States at the Heterointerface between the Band Insulators LaAlO_3 and SrTiO_3 . **Phys. Rev. Lett.** 101: 026802).
- Yu, T. H., Sha, Y., Liu, W.-G., Merinov, B. V. and Shirvanian, P. Mechanism for degradation of Nafion in PEM fuel cells from quantum mechanics calculations. **J. Am. Chem. Soc.** Article in press.



APPENDICES



APPENDIX A
EXPERIMENTAL SETUP FOR VUV IRRADIATIONS AT
THE BEAMLINE 4

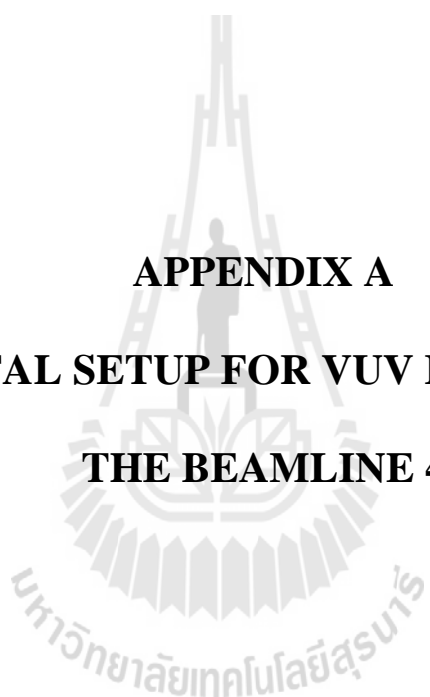


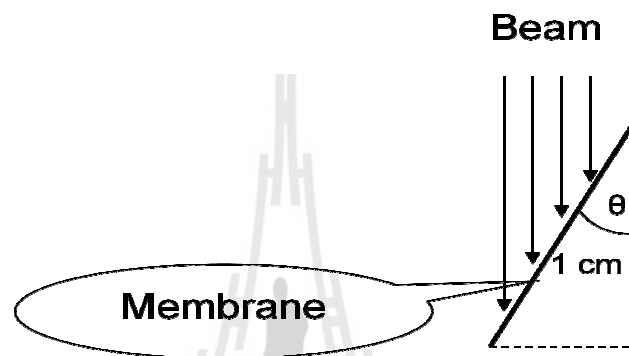


Figure A.1 VUV irradiation chamber (center): The system is constructed separately at 43 cm far from the main ARPES chamber (left hand side). Due to the water remaining in the Nafion membranes, loading the membrane into the irradiation chamber cause to increase in the pressure. Thus many vacuum pumps (two turbo molecular pumps, one ion pump and one scroll pump) are connected to the irradiation chamber in order to increase pumping speed. The base pressure of the chamber which contains one Nafion membrane is down to $\sim 10^{-7}$ mbar.

At the Beamline-4 (BL4), the VUV irradiations are performed at the irradiation chamber which placed at the distance 43 cm away from the center of the ARPES chamber as shown in Figure A.1. At this position, the synchrotron beam size is larger than the beam size at the ARPES chamber.

Table A.1. The beam sizes at the BL4.

	ARPES chamber		Irradiation chamber	
	Horizontal	Vertical	Horizontal	Vertical
FWHM	0.060	0.024	0.105	0.080
Full-size	0.141	0.056	0.247	0.188

**Figure A.2** The irradiated area expansion in horizontal direction at the irradiation chamber.

The beam sizes at these two chambers are calculated using the ray tracing program named ShadowVUI. The resulting beam sizes are summarized in Table A.1.

Because the active area of the MEAs is equal to $1 \times 1 \text{ cm}^2$, these irradiated area is not enough to cover the aspiring active area. However, the irradiated area can be expanded by tilting the sample horizontally as depicted in Figure A.2, and scanning the sample vertically all over the range of 1 cm.

From this Figure, the tilted angle can easily be obtain via the basic geometry,

$$\theta = \sin^{-1} \left(\frac{1.05 \times 2.35}{1} \right) = 14.4^\circ . \quad (\text{A.1})$$

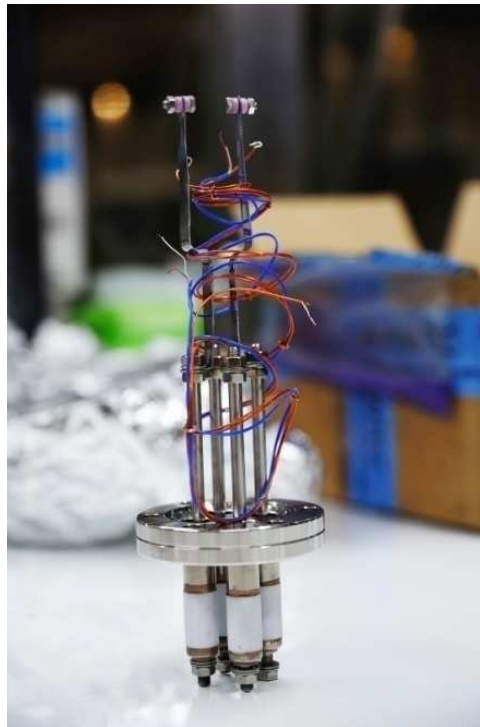


Figure A.2 Photon probe for the beam position specification: The top of this device connected with the tiny tungsten wire. By scanning the wire vertically (up and down), the current output intensity responds to the photoelectrons can be used to specify the initial beam position for the Nafion VUV irradiations.

Note that the multiplying quantity 2.35 is necessary to transform the beam size representation from the full width at half maximum (FWHM) to the full size of the beam. Additionally, because the irradiation is performed in the UV radiation, the beam exhibits invisible to observe by the human eyes. This problem results in the difficulty to trace the beam during irradiation for the vertical scan.

Therefore, the photon probe is constructed to specify the initial scanning position of the VUV irradiations. This device is shown in Figure A.2.

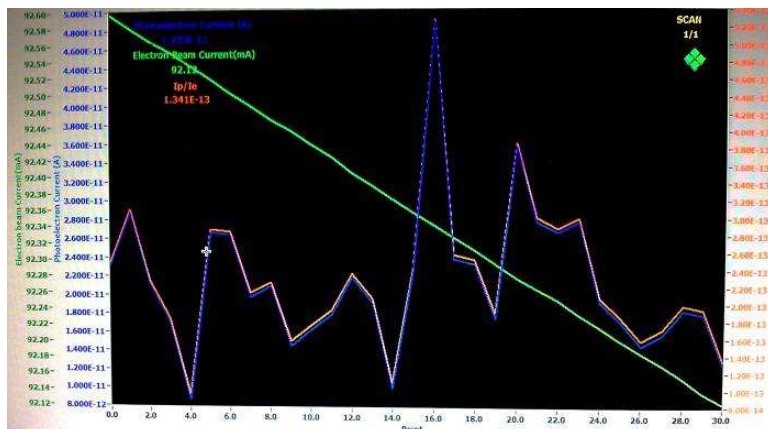


Figure A.3 The photoelectron current obtained by the photon probe within the irradiation chamber.

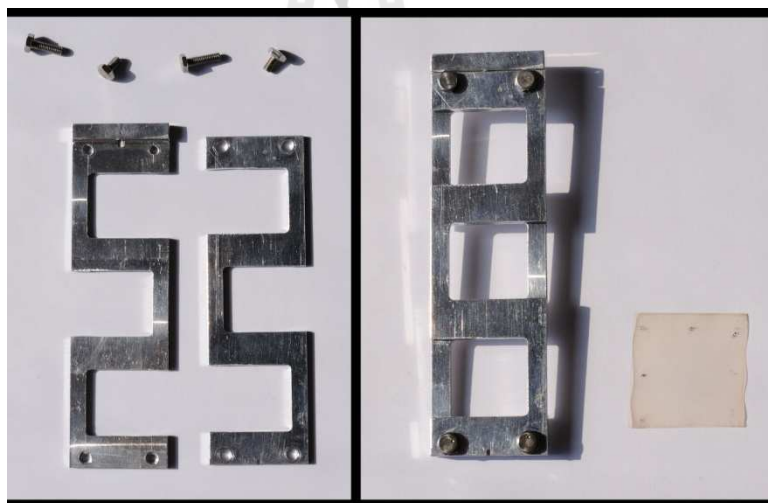


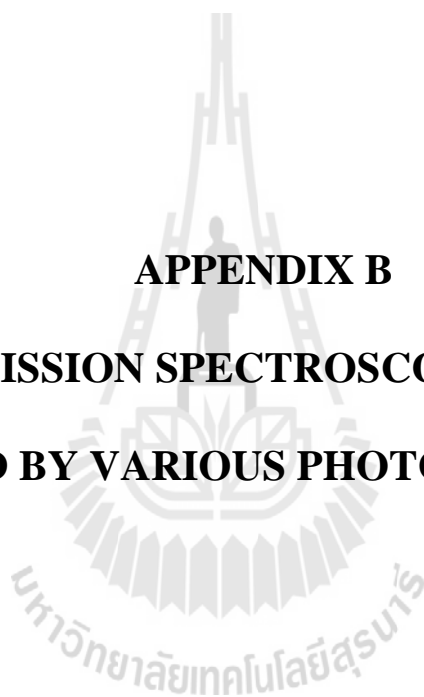
Figure A.4 VUV sample holder: To reduce the vacuum preparations, the holder is designed to be capable to holding three samples in once loading time. Moreover, the holder can rotate around its vertical axis to provide the two-side irradiations.

This initial position is obtained by checking the photoelectron current of the probe as shown in Figure A.3. The high photoelectron current causes to the high irradiation effect. And subsequently, the initial scanning position of the membrane can be specified.

After the initial irradiation position has been specified, the photon probe is moved down to the lower part of the chamber. And the sample holder (shown in Figure A.4) at the top of the chamber is moved down to the initial position. The holder made from two aluminum sheets that can rotate 360° around its vertical axis. The rotatable holder is design for two-side irradiations.



APPENDIX B
PHOTOEMISSION SPECTROSCOPY OF NAFION
EXCITED BY VARIOUS PHOTON ENERGIES



Due to the adjustable photon energy of the synchrotron light, the electronic structural changes of the Nafion with different photon energies can easily be examined. Although the PES experiments were taken in the BL4 which have low photoelectron intensity, these PES results have been used relatively to examine the relative surface chemical evolution of the degraded Nafion membranes with various photon energies. Since the grating #1 at the BL4 provides the energy range from 40 to 200 eV. However, due to low intensity at high photon energy of the monochromator system in the BL4 the PES spectra at the photon energy beyond 160 eV are unobtainable. Thus, the PES spectra of Nafion excited by the photon energies (at the 1st, 10th and 20th scans) of 40, 80, 120 and 160 eV are shown in Figures B.1a., B.1b., B.1c., B.1d., and B.1e., respectively. Note that the PES results are demonstrated after the sample charging correction.

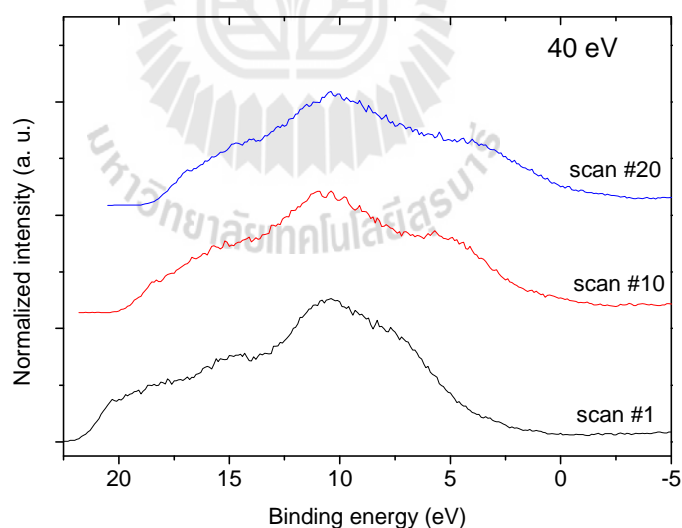


Figure B.1a PES spectra of Nafion excited by the photon energy of 40 eV: At higher fluences (in terms of the number of scan), the spectra is broadened due to the generation of the new C=C peak as observe in the PES spectra of 100 eV.

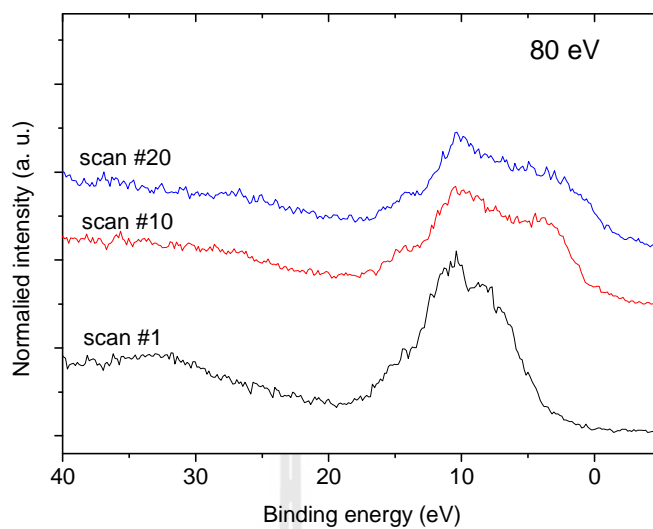


Figure B.1b PES spectra of Nafion excited by the photon energy of 80 eV: The major change of these spectra is the decrease of the fluorine-containing peaks.

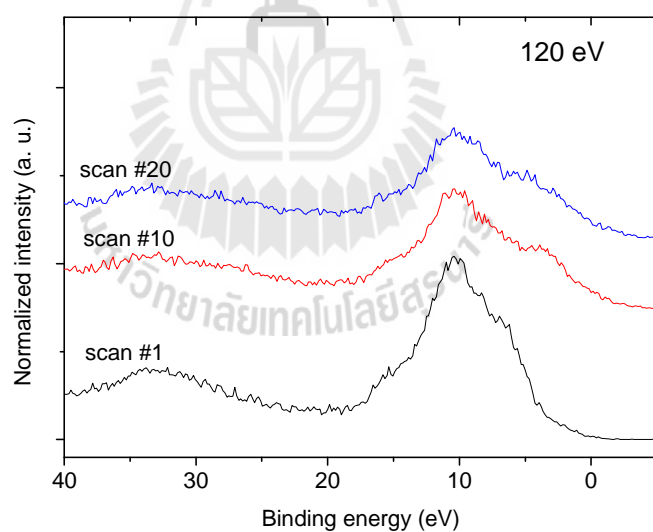


Figure B.1c PES spectra of Nafion excited by the photon energy of 120 eV: The peak intensity decreases faster than the PES peak of 80 eV.

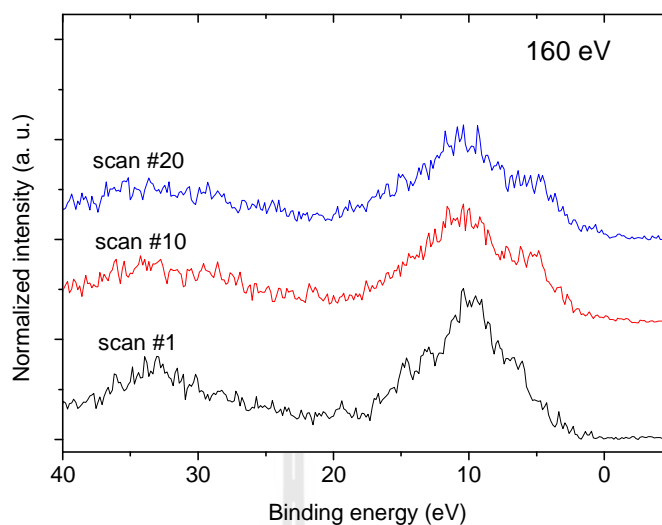


Figure B.1d PES spectra of Nafion excited by the photon energy of 160 eV: The signal to noise ratio is higher than the results observed in lower excitation energies.

These PES results conclude that the fluorine intensity decrease rapidly with increase the irradiation times (and also related to the photon fluence). Although the photon fluence depends on the photon flux (which implicitly depends on the photon energy), the PES spectra of all excited energies show the dramatic decrease in the fluorine and the contaminant species such as C-H and C-O, which have the binding energy near the F_{2p} , as shown in Figure B.2.

Consequently, whatever photon energy use in the PES measurement and the VUV irradiations, the surface state changes of the membrane have significantly been observed.

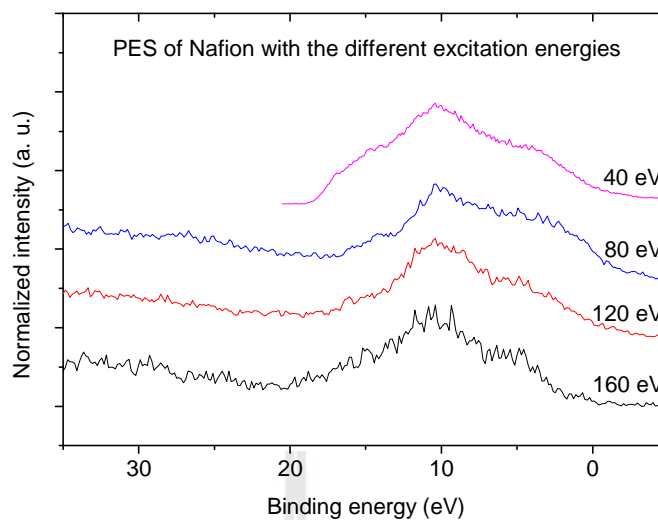
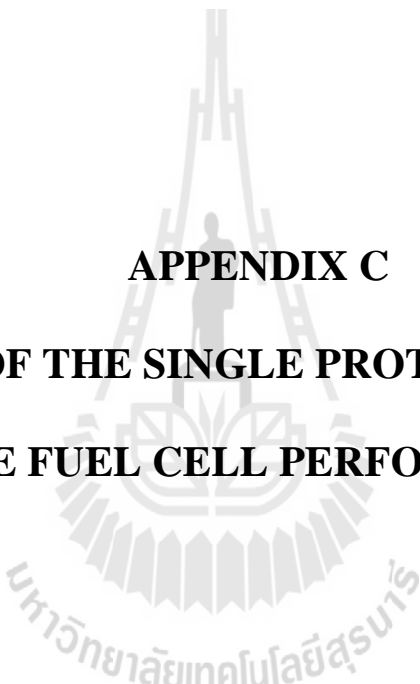


Figure B.2 Comparison of the PES spectra using 40, 80, 120 and 160 photon energy at the BL4: The spectra are taken at the 20th scan. Note that although the irradiation time of these spectra are similar, their photon fluences are different. These results indicate the decrease only in the intensity upon various photon energies in the range of VUV radiation. The structural evolution of the membrane should be described in term of the photon fluence as shown in the PES experiments in Chapter V.



APPENDIX C
METHOD OF THE SINGLE PROTON EXCHANGE
MEMBRANE FUEL CELL PERFORMANCE TESTS

After VUV irradiations, the membranes are then subjected to the single PEMFC performance test station. The methods of the performance test are shown in the following Figures

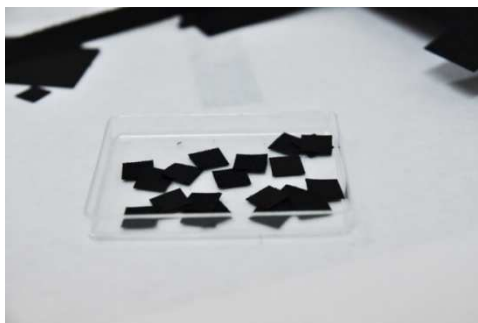


Figure C.1 Fuel cell gas diffusion electrodes (GDEs): The GDE composes of $0.4\text{mg}/\text{cm}^2$ of Pt catalyst depositing on the carbon cloth. The GDEs are cut to have the area of $1 \times 1 \text{ cm}^2$.



Figure C.2 Membrane electrode assembly preparations: (a) and (b) To increase the electrochemical reaction at the interface of the membrane and the electrodes, the GDEs have been coated with 5% wt of Nafion solution. (c) The coated GDEs are heated with 70°C for 1hr. within the oven. (d) The membranes and electrodes are then subjected into the membrane electrode assembly by hot-pressing apparatus.

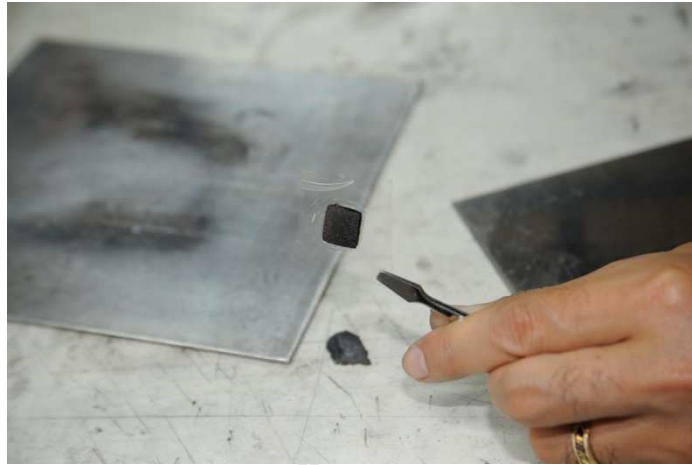


Figure C.3 Completed MEA after hot-pressing process with the temperature 130°C for 90 sec and the pressure of 1000 psig. This pressure is approximately in the range of the pressure in the natural gas pipelines (800-1000 psig.).

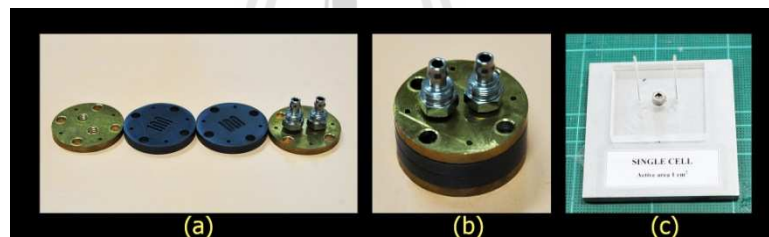


Figure C.4 The MEAs are then installed in the single PEM fuel cell system as shown. The MEA is placed at the middle of the fuel cell. (a) and (b). A single unit of the fuel cell consists of two graphite flow-field plates conducting plates which covered by the current collector plates. Moreover, the silicone gaskets have been placed between the MEA and the conducting plates in order to electrically separate the fuel cell cathode and anode. The H_2 and O_2 pass through the gases channel in the conducting plate to the carbon cloth of the MEA and build up the electrochemical reactions at the membrane-catalyst-gas interface.

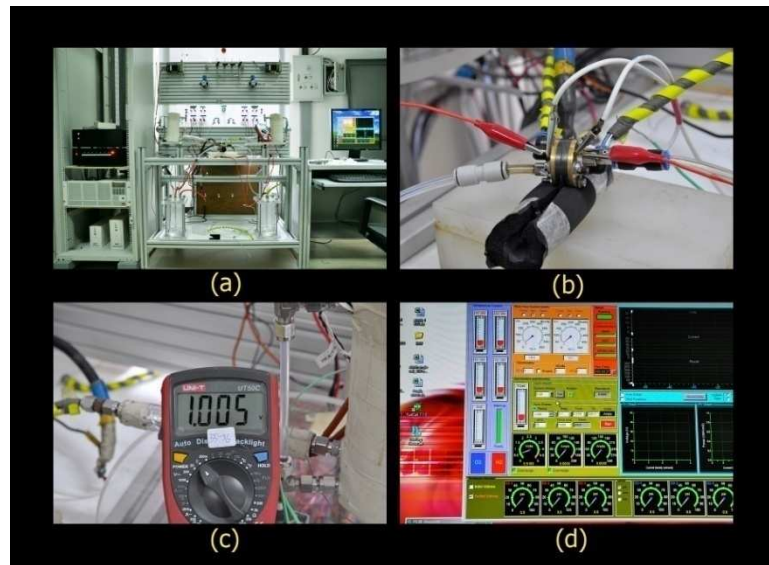


Figure C.5 (a) and (b) the single fuel cell has been brought into the test system. The system contains an electronic loader, gas flow controller, humidifier and computer control unit. The controls unit has function to control the gas flow-rate and also controls the fuel cell electric loader. (c) When connected, the first fuel cell exhibits the open circuit voltage (OCV) without any electric loads. (d) In-house computer software provided by Thailand Center of Excellence in Physics (ThEP) displays the PEM fuel cell during the bake-in operation at the current load of 0.06 A. This method is used for warm-up the fuel cell to reach to the steady state before measurement. For 1 cm^2 fuel cell active area, it requires the baking time 1-2 h. The steady state of the fuel cell is supposed to be the state that the voltage output of the fuel cell does not change significantly with the baking time.

APPENDIX D

CLASSIFICATION OF NAFION MEMBRANES

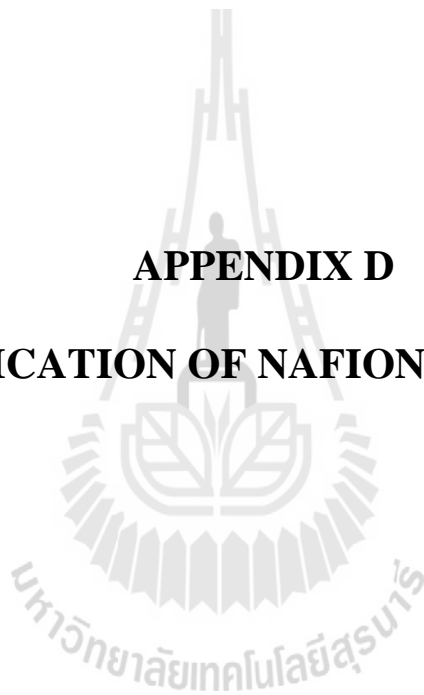


Table D.1 Nafion properties, all values taken with membrane conditioned at 23°C, 50% relative humidity (RH). (MD - machine direction; TD - transverse direction (Odgaard, 2007)).

Membrane types	Typical thickness (μm)
N-111	25
N-112	51
NE-1135	89
N-115	127
N-117	183
Other properties	
Conductivity (S/cm)	0.083
Acid Capacity (meq/g)	0.89
Specific Gravity	1.98
Tensile Strength, max. (Mpa)	43 in MD, 32 in TD
Tear Resistance - Initial (g/mm)	6000 in MD, TD

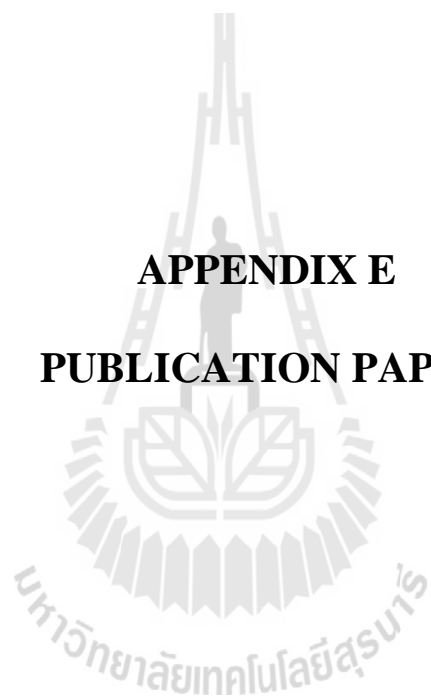
According to the classification of the perfluoropolymer membranes provided by DuPontTM, Nafion was prepared by an extrusion-cast membrane manufacturing process. Since then DuPont has been active in developing the membrane's performance by varying the equivalent weight (EW) and thickness. Note that the equivalent weight is a term which has been used in several contexts in chemistry. In polymer chemistry the EW of a reactive polymer is the mass of polymer which has one equivalent of reactivity (the mass of polymer which corresponds to one mole of reactive side-chain groups or grams polymer/mole sulfonic acid). The EW of the Nafion membrane is directly related to the ion-exchange capacity (IEC) and is defined as the molar mass of the polymer per sulfonic acid group.

$$EW = \frac{1}{IEC} \quad (D1)$$

To date, the Nafion membranes are manufactured and are available in different EW in the range between 1500 and 800, corresponding to ion-exchange capacities in the range 0.6-1.25 meq/g; the thickness is in the range 25-250 μm .

The coding in this type of polymers is determined by the first two digits, which give the equivalent weight divided by 100, and the last digit giving its thickness in mil (1 mil = 25.4 μm) in the dry state. Nafion 117 membrane, for example, employs the polymer with equivalent weight of 1100 and has a thickness of 7 mils (= 183 μm). Nafion membranes employing polymer with EW = 1100 are listed in Table D.1. 1100 equivalent weight Nafion is by far the most commonly used, and unless otherwise specified the use of the term Nafion will refer to 1100 equivalent weight Nafion. These membranes are widely used in PEMFCs due to their high proton conductivity and moderate swelling in water (Mauritz and Moore, 2004).

Table D.1 also show their physical properties. The most common membranes used today in H₂ PEMFC is the thinnest Nafion 112 and 111, and Nafion 117 is most preferred for membrane DMFC.



APPENDIX E
PUBLICATION PAPER



Computational and experimental study of low energy Ar⁺ bombardment on Nafion

Janchai Yana^{a,b}, Vannajan Sanghiran Lee^{a,b,c}, Yuttakarn Rattanachai^d, Prayoon Songsiriritthigul^{b,d,e},
Min Medhisuwakul^{b,f}, Sornthep Vannarat^g, Supaporn Dokmaisrijan^h,
Thiraphat Vilaithong^{b,e}, Piyarat Nimmanpipug^{a,b,*}

^a Computational Simulation and Modeling Laboratory (CSML), Department of Chemistry and Materials Science Research Center, Faculty of Science, Chiang Mai University, Chiang Mai 50200, Thailand

^b Thailand Center of Excellence in Physics, Commission on Higher Education, 328 Sri Ayuthaya Road, Bangkok 10400, Thailand

^c Department of Chemistry, Faculty of Science, University of Malaya, 50603, Kuala Lumpur, Malaysia

^d School of Physics, Suranaree University of Technology, NakhonRatchasima 30000, Thailand

^e Synchrotron Light Research Institute, Nakhon Ratchasima 30000, Thailand

^f Research Center in Particle Beam and Plasma Physics, Department of Physics, Faculty of Science, Chiang Mai University, Chiang Mai 50200, Thailand

^g Large Scale Simulation Research Laboratory, National Electronics and Computer Technology Center, 112 PhahonYothin Road, Klong 1, KlongLuang, Pathumthani 12120, Thailand

^h Division of Chemistry, School of Science, Walailak University, Nakhon Si Thammarat 80161, Thailand

ARTICLE INFO

Article history:

Received 30 September 2011

Accepted in revised form 27 February 2012

Available online 5 March 2012

Keywords:

Molecular dynamic simulations

Ion bombardment

Surface modification of Nafion

ABSTRACT

Nafion, a polymer electrolyte membrane of a fuel cell, can be modified by low energy Ar⁺ beam bombardment to increase its interfacial area with a catalyst. Recent experiments indicated that the sputtered sulfonate could lead to a decrease of hydrophilicity of Nafion when bombarded by a low energy Ar⁺ beam. To investigate the surface modification at the atomic level, molecular dynamic (MD) simulations and experiment were carried out. The effects of Ar⁺ at 0.5–3.0 keV, and doses in the range of 10¹⁴–10¹⁶ ions cm⁻² on the damage of the Nafion surface after bombardment were deduced from the simulations. This was assessed through both the chemical and physical changes of the Nafion side chain. The potential dissociation of the C–S bond after bombardment was analyzed in terms of the elongated bond population. The percentage of the extended C–S bond in the system was calculated to determine the possibility of sulfonate sputtering. Real-time determination of the amount of molecular species defragged under Ar⁺ ion bombardment by quadrupole mass spectroscopy (QMS) was used. The percentage of the amount of potentially broken C–S bonds after bombardment derived from MD simulations was found in a correlation with sputtering of SO₃ fragments obtained from the experiments. The calculated results confirm the thresholds at 2.0 keV as observed in experiment.

© 2012 Elsevier B.V. All rights reserved.

1. Introduction

Many of today's energy sources, including oil, natural gas, and coal, are extremely limited in supply. An alternative source of energy, from fuel cell energy, produces reliable power for commercial and industrial use with higher efficiency and virtually no pollution. The research into fuel cell developments has been focused on the efficiency of polymer electrolyte membranes (PEM) in increasing electricity production efficiency and reducing the cost of PEM fuel cells. The direction of research is not only on the development of alternative low-cost PEM [1–4], but also on the improvement of commercial PEM and Nafion, with the optimum chemical and physical properties.

The Nafion membrane has been modified by several approaches. The improvement of stabilized membranes at high temperatures

was introduced to improve fuel cell durability and reliability [5,6]. To reduce costs of PEM fuel cells with low platinum catalyst loading and alternative catalysts have been developed [7–10]. Furthermore, the modification of the Nafion membrane surface by experimental ion beam bombardment results in an increase in the interface of the catalyst and electrode area. Cho et al. [11] and Prasanna et al. [12] studied Ar⁺ ion beam bombardment on the surface of a Nafion membrane in order to increase the effective area of the catalyst/electrolyte interface [11] and to reduce the Pt loadings for the electrodes [12]. The roughness and hydrophobicity of the Nafion® 115 membrane surface were found to significantly increase while the proton conductivity of the membrane was not affected by bombardment with Ar⁺ ions (between 10¹⁵ and 10¹⁷ ions cm⁻² at 1 keV). The membrane bombarded with an ion density dose of 10¹⁶ ions cm⁻² at 1 keV exhibited the maximum ion energy density. Beyond the optimum ion energy and dose, the fuel cell performance decreased probably due to the loss of catalyst powders buried in the deep fissures on the membrane surface.

To simulate surface change from ion bombardment at a high energy range, Fekete et al. [13] modeled the effects of ion implantation

* Corresponding author at: Computational Simulation and Modeling Laboratory (CSML), Department of Chemistry and Center for Innovation in Chemistry, Faculty of Science, Chiang Mai University, Chiang Mai 50200, Thailand.
E-mail address: piyaratn@gmail.com (P. Nimmanpipug).

into Nafion, using TRIM module of the SRIM program [13]. In this visual study, a selected series of the positive ions with energies of 20–320 keV, was used to bombard the target polymer. They found that the ion energies of 100–200 keV can affect the outer 0.5–3 μm of the surface layer. The depth of the implanted ions in Nafion increases as the ion energies increased. Additionally, the collisions between ions and polymer moiety can alter the permeability of the Nafion membrane.

Atomistic simulation as molecular dynamic (MD) simulation offers another choice for investigating the molecular changes of this phenomenon since MD simulation involves with the numerical solutions of the classical equations of motion. This computational method can help in the understanding of the properties of molecules, in terms of structure and the microscopic interactions [14,15]. Thus, it is necessary to study of the interactions between impacted ions and target polymers. The MD simulation technique can apply for the studies of the modification of synthetic and natural polymers by atom/ion bombardment [16–18]. Végh et al. [16] reported that the MD results by repeated impact in order to mimic higher ion doses can exhibit a formation of a heavily cross-linked and dehydrogenated damaged layer of polystyrene model. Also, sputtering yield of carbon after bombardment analyzed in terms of the ratio of carbon per Ar^+ is consistent with the observed experiment. Sinnott et al. [17] studied of the MD simulations of modification of poly(methyl methacrylate) or PMMA surface by 1 keV Ar atom bombardment. They indicated that the deposition of Ar atoms on PMMA produces chemical changes within the PMMA substrate and etches the surface. In Ref. [18], the low energy ion bombardment on naked DNA was studied using MD simulations. They proposed a useful technique for analysis of bond-breaking occurring in nucleotides. Also, changes in bond lengths and visibly distorted structures of bombarded nucleotides were clearly observed from the MD results.

In this study an attempt has been made to clarify the effects of ion implantation into the Nafion membrane on properties of bombarded Nafion. To study the theoretical account of the ion bombardment on the Nafion surface, at correlated low ion energy and ion doses reported by Cho et al. [11] and Prasanna et al. [12], MD simulations of Ar^+ bombardment on Nafion were investigated in the present study. A concrete explanation of the ion bombardment on modified Nafion will be considered here. The chemical and physical changes on the Nafion surface, resulting from the bombardment, will be compared with the experimental data in order to increase understanding into the effects of this treatment. The understanding of this microscopic phenomenon will help with the design of the fuel cell membranes using a molecular level perception.

2. Methodology

2.1. Preparation of the Nafion model

The optimized structure of the Nafion side chain ($\text{CF}_3\text{OCF}_2\text{CF}(\text{CF}_3)\text{OCF}_2\text{CF}_2\text{SO}_3^-$; Fig. 1) was taken from previous works [19,20]. The

building unit was used to construct a Nafion model for MD simulation. The Nafion model consists of 1024 side chains confined in a monoclinic MD box (Fig. 1). The total number of atoms in the simulation cell is 5224 atoms. The position of the side chains in the MD box was introduced based on the X-ray crystallographic data for trifluoromethanesulfonic monohydrate [21].

The energy structure of the model was minimized until the gradients were lower than $0.005 \text{ kcal/mol}^{-1}$. The optimized Nafion model was used for subsequent MD simulations. The NPT ensemble which a number of particles, pressure and temperature were kept constant in the simulation was applied to the equilibration process of the system using Materials studio (MS) version 4.4 program package [22]. The COMPASS force field, a powerful force field that supports atomistic simulations of polymers, was used for all calculations [23,24]. The potential function of COMPASS force field was shown in Eq. 1 [24].

$$E_{\text{total}} = \sum_b \left[k_2(b-b_0)^2 + k_3(b-b_0)^3 + k_4(b-b_0)^4 \right] + \sum_\theta \left[k_2(\theta-\theta_0)^2 + k_3(\theta-\theta_0)^3 + k_4(\theta-\theta_0)^4 \right] + \sum_\phi \left[k_1(1-\cos\phi) + k_2(1-\cos 2\phi) + k_3(1-\cos 3\phi) \right] + \sum_x k_2 x^2 + \sum_{b,b'} k(b-b_0)(b'-b'_0) + \sum_{b,\theta} k(b-b_0)(\theta-\theta_0) + \sum_{b,\phi} (b-b_0) \left[k_1 \cos\phi + k_2 \cos 2\phi + k_3 \cos 3\phi \right] + \sum_{\theta,\phi} (\theta-\theta_0) \left[k_1 \cos\phi + k_2 \cos 2\phi + k_3 \cos 3\phi \right] + \sum_{b,\theta} k(\theta'-\theta_0)(\theta-\theta_0) + \sum_{\theta,\theta',\phi} k(\theta-\theta_0)(\theta'-\theta'_0) \cos\phi + \sum_{ij} \frac{q_i q_j}{r_{ij}} + \sum_{ij} \epsilon_{ij} \left[2 \left(\frac{r_{ij}^0}{r_{ij}} \right)^9 - 3 \left(\frac{r_{ij}^0}{r_{ij}} \right)^6 \right]. \quad 1$$

The functions are divided into two categories, bonded and nonbonded terms. Bond (b), angle (θ), torsion angle (ϕ), and the cross-coupling terms include combinations of two or three internal coordinates are represented for bonded term. The IJ-9-6 function used for the van der Waals (vdW) term and a Coulombic function used for an electrostatic interaction are represented for nonbonded interaction term.

The MD time step was set at 1.0 fs, the pressure was set at 1.0 bar, and the target temperature was set at 298 K. The temperature of the whole system was gradually increased to the target temperature, in the first 60 ps, using Berendsen algorithm [25]. This was further performed at 298 K for 440 ps, and the last structure was kept for ion bombardment simulations. The dimensions of equilibrated Nafion model were $80 \times 60 \times 75 \text{ \AA}^3$ with a density of 2.04 g cm^{-3} (Fig. 1), corresponding to the value observed for Nafion® 115 commercial data by the DuPont company.

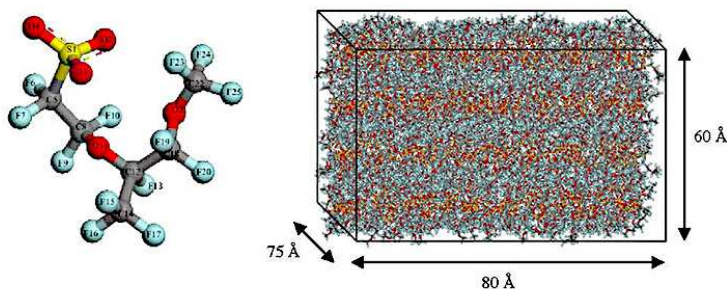


Fig. 1. Structure of Nafion side chain (left) and MD box of Nafion model (right).

2.2. MD simulations of ion bombardment on Nafion model

Two sets of MD simulations of the Ar^+ ion bombardment on the Nafion model were carried. These aimed to investigate the effect of the initial kinetic energy (KE) of the Ar^+ ions; and the effect of the Ar^+ ion dose on the bombarded Nafion. In the first set, six of MD simulations using canonical (NVT) ensemble with constant number of particles, volume, and temperature were performed at 353 K and each case study was repeated for three times to obtain a statistical average of the depths of implanted Ar^+ ions within the Nafion model. The initial KE of the Ar^+ ions was assigned at 0.5, 1.0, 1.5, 2.0, 2.5, and 3.0 keV, by varying the initial velocities of the Ar^+ ions, as computed from a typical kinetic energy function. The ion dose of 1×10^{14} ions cm^{-2} corresponded to 45 Ar^+ ions in the simulated system was used. These then generated Ar^+ ion beam were projected along the x-axis of the Nafion model, as shown in Fig. 2. All ion bombardments were performed at normal incidence but at random positions of the surface. In this study, non-periodic simulation was employed to investigate non-uniform ion bombardment scenario. In order to examine the effect of the ion dose in the bombardment on the Nafion, in correlation with experiments [11,12], the Ar^+ ions should be varied from 1×10^{14} to 1×10^{17} ions cm^{-2} with a KE of 1 keV. From the simulation, the bombardment using 45 Ar^+ shows strong inter-ion Ar ion–ion interaction during projection. In this study, Nafion model surface was generated with exposed area dimension of $60 \times 75 \text{ \AA}^2$. To avoid the edge effects of boundary potential and geometry in the simulation, the ion bombardment was limited to the central area away from the cell edge. The initial coordinates of Ar^+ in each simulation were randomly generated with their projection to the surface in a distance of 18–25 \AA from the center. To impose the doses of 10^{14} – 10^{17} ions cm^{-2} , 45–4500 ion impacts should be simulated. However, from the simulation, the bombardment using 45 Ar^+ shows strong Ar ion–ion interaction during projection. Consequently, successive simulations were conducted to mimic the experimental study. For examples, to study of ion dose of 5×10^{14} ions cm^{-2} , five successive simulations were conducted by using 45 Ar^+ in each simulation. In each dose of the Ar^+ ions, the NVT-MD simulations were performed at 353 K, which is the working condition of a fuel cell. Each simulation was repeated three times to eliminate bias in the calculations. All bombardment simulations were performed with 1 fs time step, and, the simulation time for one ion impact trajectory was 1 ps.

2.3. Experimental study of the Ar^+ ion bombardment on Nafion

The investigations of Ar^+ ion bombardment on Nafion membranes were carried out in a sample preparation chamber of a photo-emission experimental station of the beamline 3.2a at the Synchrotron Light Research Institute. Smaller pieces ($0.5 \times 0.5 \text{ cm}^2$) of Nafion® 115 membranes were used for this work. The samples were chemically treated in 2 wt.% H_2O_2 solution at 80 °C for 60 min to remove organic impurities, then rinsed with de-ionized water at 80 °C for 60 min, followed by sulfonation in 10 wt.% H_2SO_4 at 80 °C

for 60 min to remove metallic impurities and to increase the sulfonic acid group, and finally in de-ionized water at 80 °C for 60 min to remove the acid. The membranes were dried under vacuum at room temperature for over 2 days before introducing the samples into the sample preparation chamber, via the load-lock systems to prevent breaking UHV condition. It should be noted that the base pressure of the preparation chamber was 2×10^{-10} Torr, however due to the high out gassing rate of the membranes, the vacuum pressure rose up to about 1×10^{-9} Torr.

A cold cathode ion sputter gun was used to generate the ion bombardment. To produce Ar^+ ions, pure Ar gas was let in to the ion sputter gun, raising the vacuum pressure up to about 2×10^{-6} Torr. The energy of the ion was varied from 0.5 keV to 3.0 keV, and the flux of the bombarding ions was measured using a Faraday cup located adjacent to the membrane sample. Quadrupole mass spectrometry (QMS) was used for real-time determination of the amount of molecular species that were defragged by ion bombardment.

3. Results and discussions

3.1. Effects on energies/doses of Ar^+ ions on Nafion surface

From previous experiments [11,12], the effects of Ar^+ bombardment on Nafion membrane were analyzed by studying the morphology, roughness and hydrophobicity of the surface. To investigate material characteristics at the atomistic level, the Nafion model after bombardment simulations was characterized in terms of damage profile and the implanted Ar^+ ion depth. The long-range modification of molecular arrangement in Nafion models with six different values of initial KE of Ar^+ bombarded on Nafion was considered as shown in Fig. 3. The ion implantation depth varies with the ion's initial KE. The Ar^+ ions are randomly trapped in the Nafion structure.

Generally, the traditional force fields cannot describe the bond formation and dissociation of covalent bonds distinctly during the simulation since it does not explain the behavior of electrons in atom. Although, the reactive empirical function such as a AIREBO potential proposed in Ref. [17] can allow for that of hydrocarbon. However, the traditional force field has been proven that it can be used to describe the change of covalent bonds in simulation technique using the equilibrium bond distances [18]. Thus in this work, instead of using reactive empirical function, bond breaking criteria were proposed and statistical analysis was performed to correlate the analysis with experimental evident. The dynamics of bombarded chains are distinctly different from the bulk region. The collisions result in a change of the surface structure which increases surface roughness and area. Material surface damage occurring within the Nafion model has an irregular shape with different sizes and depths along the x-axis of the Nafion. Penetration depths of Ar^+ in the Nafion model, with respect to initial KE values, are shown in Fig. 4. The distances were measured from material surface to the maximum Ar^+ -trapped position.

It is clear that the size and depth of the surface damage, as well as implantation depth of Ar^+ in the Nafion model, are in proportion to

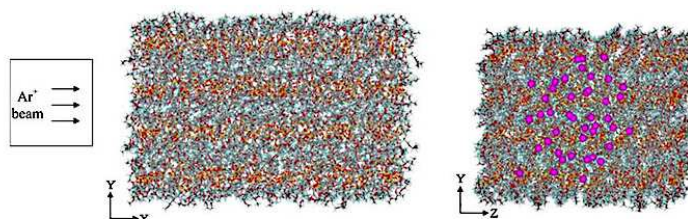


Fig. 2. Model of Ar^+ ion bombardment on Nafion model viewed along XY plane and YZ plane.

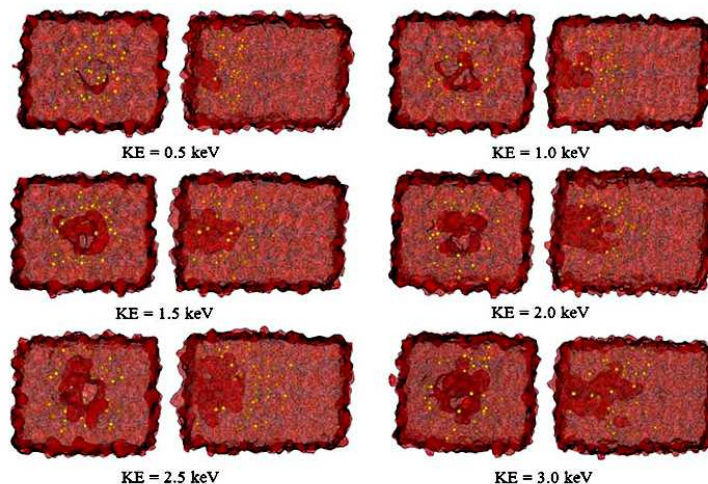


Fig. 3. The surface damage and Ar⁺ implantation within the Nafion model after Ar⁺ bombardment at different KEs in YZ plane (left) and XY plane (right) at 1×10^{14} ions cm⁻².

the initial KE value of the Ar⁺ ions. These MD results correspond with the MC results observed by Fekete et al. [13] in which increasing the KE of bombarded ions increased the damage depth on the Nafion and the depth of implanted Ar⁺ ions. This is reasonable since the collision of high KE particles on the target is more forceful than that of a low KE.

The morphology of the bombarded Nafion surface of each model, viewed along YZ plane, shows that surface area of the damage cavity was extended as the Ar⁺ ion dose increased (Fig. 5). The depth of damage cavity within the Nafion model, viewed along XY plane, shows that the damage cavity was also deeper into the Nafion model as of the Ar⁺ ion dose increased. The influence of ion dose on the surface modification is higher than the influence of ion energy. These results may have occurred as the Ar⁺ ion dose density was increased and the number of times the Ar⁺ ion beams directly struck the central area of Nafion model. This also increases the depth of the implanted Ar⁺ ions in the Nafion model. The results obtained from this study are consistent with the roughness profile of the bombarded Nafion determined from surface images [11].

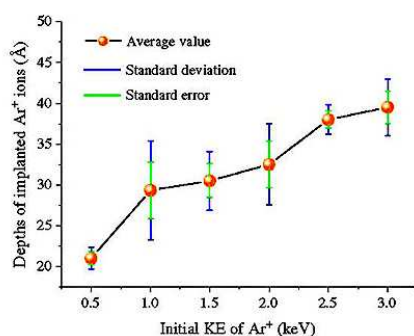


Fig. 4. Depths of Ar⁺ implantation within the Nafion model after Ar⁺ bombardment at different KEs at 1×10^{14} ions cm⁻². Standard error and deviation was obtained from three repetitions of dynamic simulations.

3.2. Effect of Ar⁺ ion bombardment on hydrophobicity of Nafion

Hydrophobicity of the bombarded Nafion was previously investigated by determining the water contact angle [11,12]. This is an important property of Nafion since a hydrophobic surface can reduce the water content absorbed in the modified Nafion, while the proton conductivity of all membrane was almost constant [11]. In this study,

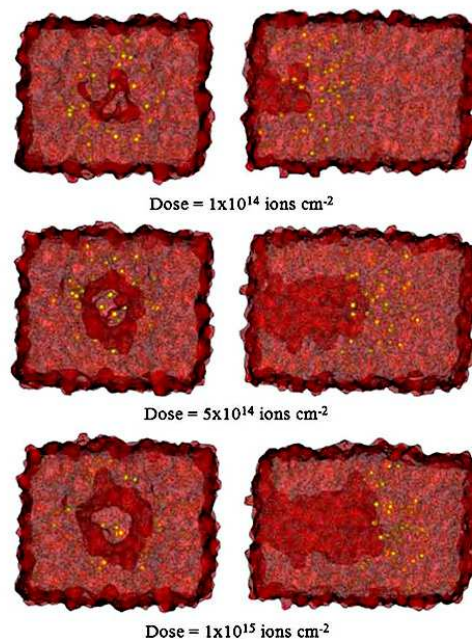


Fig. 5. The surface damage and Ar⁺ implantation within the Nafion model after Ar⁺ bombardment at three different doses at energy of 1 keV in YZ plane (left) and XY plane (right).

the hydrophobicity of the bombarded Nafion was examined using SO_3^- sputtering from the Nafion surface. Since the polar SO_3^- group of the Nafion side chain can strongly bind with water molecules, it therefore adsorbs the water molecules within the Nafion.

Basically, the bond-breaking of a covalent bond can occur if it is significantly elongate from the equilibrium distance [18]. Therefore, the potentially breakable C–S bond of the Nafion was used as a criterion for analysis of the SO_3^- sputtering. In this work, the sputtering rate of SO_3^- fragment was calculated from sampling 10 side chains in each of bombarded and unbombarded Nafion model to analyze the fluctuation of C–S bond distances. In simulation time of 1 ps, the motion of Ar^+ reaches a steady state which implies all ion energy deposition on the surface. Structural data of the bombarded side chain located in the damage cavity, and unbombarded side chains were collected every 0.05 ps until reach into 1.00 ps for analysis (Table 1). Ten Nafion side chains of sampling were chosen from exposed part (10 Å from the surface) of the model. In other words, 10 chains are sampling of totally 128 side chains which is equal to 7.81 percentage of surface. The mean values of the C–S bond distances of unbombarded and bombarded side chains are 1.82 and 1.92 Å, respectively.

The fluctuation of C–S bond distances was analyzed in terms of standard deviation (SD). The SD value of 0.12 Å was found in unbombarded side chains while a higher value of 0.30 Å was found in bombarded side chains. The potentially broken C–S bond in the model was numbered in two alternative ways to ensure and validate the results. One was in terms of the percentage of the amount of C–S bond with an average distance higher than 2.22 Å ($1.92 + 0.30 = 2.22$). The other is the percentage of the amount of C–S bonds that have an SD value higher than 0.30 Å. Additionally, the breaking of the C–S bond can observe from the relative C–S bond energies profile computed from the COMPASS force field as shown in Fig. 6(c). It is obvious that the relative C–S bond energies are very much higher than the minimum (ca. 27 kcal mol⁻¹) as the C–S bond distances are larger than 2.22 Å, leading to the dissociation of the C–S bond. The number

of C–S bond with distance longer than 2.25 Å was also analyzed in Fig. 6(d). The results of both criteria show similar tendency. In addition, interestingly, the use of C–S bond breaking criteria in our study; 2.22 and 2.25 Å, is essentially the same as C–S distance of its transition state calculated by density functional theory reported by Venuvanalingam et al. [26].

The results can imply that the Ar^+ ion bombardment on Nafion can cause increased hydrophobicity of Nafion as reported by Cho et al. [11] and Prasanna et al. [12]. The sputtering rate of SO_3^- fragments was examined from six MD simulations with a varied initial KE of Ar^+ ions ranging from 0.5 to 3.0 keV. These theoretical data were compared with experimental data derived from mass spectrometry. The sputtering rates of the SO_3^- fragment obtained from the experiment and computation are shown in Fig. 6. The percentage of the amount of potentially broken C–S bonds after bombardment was derived from MD simulations and sputtering of SO_3^- fragments obtained from experimental data showed the same trends. The sputtering rate increased as the initial KE of Ar^+ ions increased. In addition, the calculated results confirm the thresholds at 2.0 keV as observed in experiment. Although the sputtering rate calculated from each MD result is higher than that observed from the experiment, the sputtering rate of SO_3^- computed from this work can still be used to describe the effect of initial KE of Ar^+ ions on the sputtering rate of SO_3^- fragments of Nafion. The different values of sputtering rates derived from simulations and the experiment explain that the percentage of the amount of potentially broken C–S bonds is computed from damage side chains in the specific damage zone. On the other hand, the experimental sputtering rate was measured from the amount of damage fragments that were sputtered out of a sample in both the overall bombarded and unbombarded regions. Moreover, in the simulations, all Ar^+ ions were forced to directly strike the Nafion model with the same initial KE for all Ar^+ ions; while the experimental Ar^+ ions generated from an ion source can move in all possible directions, depending on the repulsion forces, before they hit the specimen.

Table 1

Fluctuation of the C–S bond distance in bombarded and unbombarded Nafion side chain analysis from trajectory of systems during simulation time of 1 ps at 1 keV, 1×10^{14} ions cm⁻², and number of chains.

Side chain no. time (ps)	C–S bond distance of unbombarded Nafion side chain (Å)										C–S bond distance of bombarded Nafion side chain (Å)									
	1	2	3	4	5	6	7	8	9	10	1	2	3	4	5	6	7	8	9	10
0.00	1.80	2.04	2.01	1.75	2.01	1.78	1.61	1.68	1.72	1.91	1.67	2.03	1.64	1.79	1.83	1.65	1.69	1.67	2.08	2.17
0.05	1.84	1.68	1.56	1.86	1.69	1.67	1.77	1.85	1.65	1.63	1.60	1.47	1.75	1.60	2.20	1.63	1.69	1.52	1.63	2.03
0.10	1.91	2.03	2.12	2.01	2.02	1.82	1.66	1.60	1.90	1.87	2.66	1.87	1.05	2.13	1.87	2.41	1.48	1.87	1.82	1.83
0.15	1.59	2.06	1.92	1.99	2.00	1.76	1.58	1.80	1.67	1.67	1.85	2.02	1.78	2.63	2.78	1.51	2.53	2.09	2.87	2.44
0.20	1.92	1.82	1.74	2.07	1.93	2.06	1.76	1.55	1.79	1.66	1.84	1.39	2.04	2.27	2.36	2.51	2.35	1.98	1.53	2.40
0.25	1.65	1.72	1.43	1.93	1.96	2.04	1.59	1.83	1.96	1.91	1.30	1.38	1.93	2.46	2.21	2.25	2.38	2.59	1.62	2.01
0.30	1.99	2.08	1.69	2.05	1.75	1.92	1.61	1.65	1.84	1.80	2.17	2.15	1.65	1.92	1.90	1.67	2.48	2.47	2.20	2.38
0.35	1.87	1.91	2.11	1.90	1.75	1.74	1.59	1.68	1.85	1.76	1.78	2.15	2.18	1.75	2.75	2.08	2.27	2.54	2.32	2.42
0.40	1.81	1.79	1.79	1.92	1.84	1.65	1.64	1.61	2.06	1.84	1.63	2.32	1.88	2.19	2.89	1.80	2.01	2.09	1.59	2.63
0.45	1.82	1.77	1.78	2.11	1.87	1.68	1.63	1.65	1.88	1.90	1.58	1.65	1.45	2.27	2.14	2.34	1.77	1.95	2.25	2.26
0.50	1.87	1.76	1.66	1.99	1.82	1.73	2.05	1.59	2.03	1.90	1.71	1.75	1.94	1.77	1.85	1.90	1.67	2.52	1.99	2.26
0.55	1.77	1.77	2.09	2.06	1.84	1.84	1.67	1.62	2.01	1.98	2.04	1.46	2.13	2.05	2.45	2.32	2.03	1.69	2.07	1.86
0.60	1.95	1.64	1.92	2.01	1.87	1.71	1.79	1.56	2.07	1.87	1.49	1.65	1.52	1.98	2.00	1.61	1.57	1.48	2.26	1.88
0.65	1.73	1.67	1.81	2.08	1.98	1.73	1.74	1.56	1.94	1.86	1.69	1.54	2.24	1.92	2.18	1.73	1.70	1.89	1.67	1.78
0.70	1.87	1.60	1.82	2.01	1.84	1.68	1.80	1.58	1.94	1.87	1.76	1.77	1.68	1.96	1.48	2.03	1.45	2.28	1.70	1.90
0.75	1.79	1.64	1.74	2.03	1.86	1.60	1.71	1.59	2.01	1.89	1.88	1.39	2.00	1.78	2.06	1.98	1.67	2.02	2.00	1.94
0.80	2.04	1.52	1.92	2.06	1.76	1.72	1.80	1.60	1.95	1.86	1.79	1.65	1.90	1.62	1.84	2.01	1.56	1.79	1.98	1.82
0.85	1.80	1.67	1.84	2.01	1.92	1.88	1.86	1.59	2.05	1.87	1.70	1.82	2.02	1.71	2.22	2.06	1.58	1.87	2.06	1.88
0.90	1.83	1.66	1.73	2.07	1.94	1.79	1.72	1.61	2.07	1.80	1.75	1.44	1.98	1.37	2.22	1.82	1.56	1.83	2.09	1.84
0.95	2.02	1.62	1.68	1.98	1.91	1.72	1.83	1.70	2.07	1.92	1.75	1.62	2.31	2.08	2.65	2.06	1.48	1.89	1.97	1.70
1.00	1.90	1.64	1.79	2.11	1.98	1.69	1.83	1.61	2.00	1.83	1.66	1.73	1.99	1.58	2.14	2.03	1.65	1.84	1.90	2.06
Mean	1.85	1.77	1.82	2.00	1.88	1.77	1.72	1.64	1.93	1.84	1.78	1.73	1.86	1.94	2.19	1.97	1.84	1.99	1.98	2.07
Average of mean	1.82																			
SD	0.11	0.17	0.18	0.09	0.09	0.12	0.12	0.09	0.13	0.09	0.27	0.28	0.29	0.31	0.36	0.28	0.36	0.32	0.31	0.27
Average of SD	0.12										0.30									
Maximum	2.04	2.08	2.12	2.11	2.02	2.06	2.05	1.85	2.07	1.98	2.66	2.32	2.31	2.63	2.89	2.51	2.53	2.59	2.87	2.63

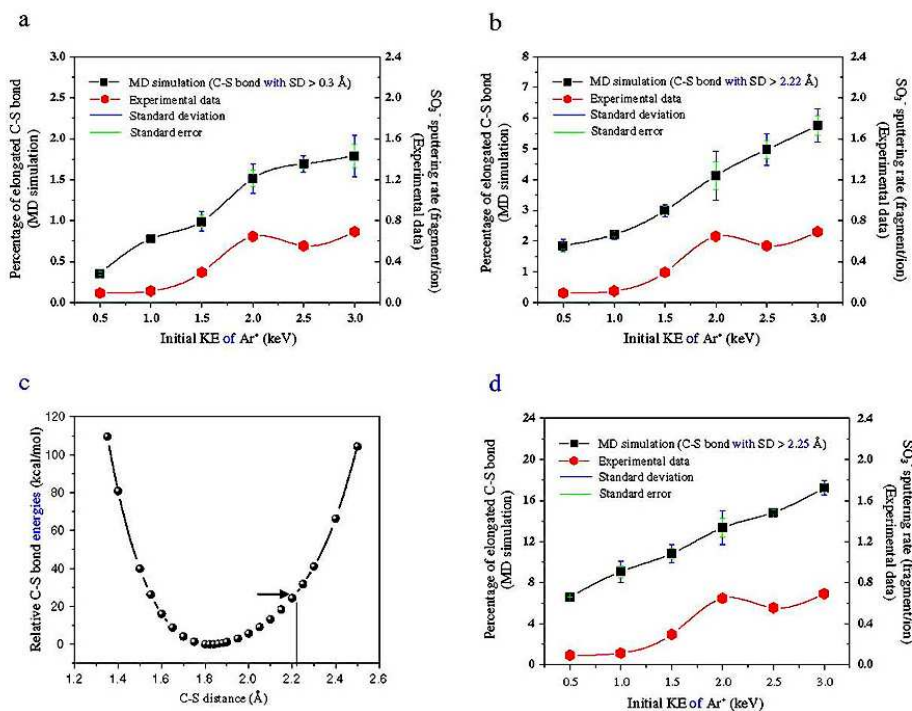


Fig. 6. Comparison of potentially broken C-S bonds after bombardment simulations and sulfonate fragment sputtering observed from experiment. Statistical analysis of potentially broken C-S bonds based on different criteria (a) SD value more than 0.30 Å and (b) distance average plus SD value more than 2.22 Å (c) relative C-S bond energies of C-S bond (d) potentially broken C-S bond based on C-S distance elongated more than relative C-S bond energies.

4. Conclusion

MD simulations and real-time determination of the amount of molecular species defragged under Ar⁺ ion bombardment by quadrupole mass spectroscopy (QMS) were carried out to understand microscopic properties and this information can reveal the chemical and physical changes of Ar⁺ initial energy and doses on Nafion modification. The variation of Ar⁺ kinetic energies of 0.5, 1.0, 1.5, 2.0, 2.5, and 3.0 eV, at a dose of 1×10^{14} ions cm⁻², was applied to the MD

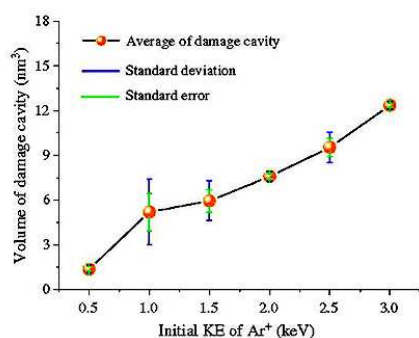


Fig. 7. Damaged cavity volume of Ar⁺ implantation within the Nafion model after Ar⁺ bombardment at different KEs at 1×10^{14} ions cm⁻². Standard error and deviation was obtained from three repetitions of dynamic simulations.

simulation to study the initial energy effect. While the variation of Ar⁺ doses of 1×10^{14} , 5×10^{14} , and 1×10^{15} ions cm⁻² at 1.0 keV was designed to study the ion dose effect. From the MD simulation of low energy Ar⁺ beam bombardment on the Nafion side chain cluster model, the Ar⁺ bombardment on the Nafion surface can increase the surface area determined in term of three dimensional volume as shown in Fig. 7. The energy and dose of Ar⁺ affect the surface roughness of the Nafion, and the Ar⁺ energy potentially breaks the C-S bond, leading to SO₃⁻ sputtering decreasing the hydrophilicity of the bombarded Nafion. The percentage of potentially C-S bonds broken in the system for all Ar⁺ energies are in agreement with the experimental SO₃⁻ sputtering measured by in-situ mass spectroscopy. As the higher initial kinetic energy from of Ar⁺ was applied, percentage of elongated C-S bond analysed from MD trajectories increase but reach a local peak at 2.0 keV, then slightly decline down afterward confirming the thresholds at 2.0 keV as observed in experiment.

Acknowledgments

The authors would like to express grateful acknowledgment to the Computational Nanoscience Consortium (CNC) Nanotechnology (NANOTEC), Thailand for the access to Accelrys Materials Studio version 4.4 and Accelrys Discovery Studio version 2.5 program packages. The authors acknowledge financial support from the Thailand Graduate Institute of Science and Technology (TGIST), the Center for Innovation in Chemistry (PERCH-CIC), the National Research University Project under Thailand's Office of the Higher Education Commission, and the National Metal and Materials Technology Center (MTEC). The authors are also grateful to Prof. Kohji Tashiro from the

Department of Future Industry-oriented Basic Science and Materials, Graduate School of Engineering, Toyota Technological Institute, Japan, for his kind suggestions.

References

- [1] B. Smitha, S. Sridhar, A.A. Khan, *J. Membr. Sci.* 459 (2005) 10.
- [2] Y. Wang, K.S. Chen, J. Mishler, S.C. Cho, X.C. Adroher, *Appl. Energy* 88 (2011) 981.
- [3] K.D. Kreuer, A. Fuchs, M. Ise, M. Spaeth, J. Maier, *Electrochim. Acta* 43 (1998) 1281.
- [4] H.G. Herz, K.D. Kreuer, J. Maier, G. Scharfenberger, M.F.H. Schuster, W.H. Meyer, *Electrochim. Acta* 48 (2003) 2165.
- [5] H.W. Starkweather Jr., *Macromolecules* 15 (1982) 320.
- [6] H.R. Corti, F. Nores-Pondal, M.P. Buera, *J. Power Sources* 161 (2006) 799.
- [7] C.W.B. Bezerra, L. Zhang, K. Lee, H. Liu, A.L.B. Marques, E. Marques, H. Wang, J. Zhang, *Electrochim. Acta* 53 (2008) 4937.
- [8] L. Zhang, J. Zhang, D.P. Wilkinson, H. Wang, *J. Power Sources* 156 (2006) 171.
- [9] F. Charreteur, F. Jaouen, S. Ruggeri, J.-P. Dodelet, *Electrochim. Acta* 53 (2008) 2925.
- [10] F. Charreteur, F. Jaouen, S. Ruggeri, J.-P. Dodelet, *Electrochim. Acta* 53 (2008) 6881.
- [11] S.A. Cho, E.A. Cho, I.H. Oh, H.J. Kim, H.Y. Ha, S.A. Hong, J.B. Ju, *J. Power Sources* 155 (2006) 286.
- [12] M. Prasanna, E.A. Cho, H.J. Kim, T.H. Lim, I.H. Oh, S.-A. Hong, *J. Power Sources* 160 (2006) 90.
- [13] Z.A. Fekete, E. Wilusz, F.E. Karasz, *J. Polym. Sci., Part B: Polym. Phys.* 42 (2004) 1343.
- [14] M.P. Allen, D.J. Tildesley, *Computer Simulation of Liquids*, Oxford University Press, New York, 1989.
- [15] A.R. Leach, *Molecular Modelling: Principles and Applications*, Prentice Hall, 2001.
- [16] J.J. Végh, D. Nest, D.B. Graves, R. Bruce, S. Engelmann, T. Kwon, R.J. Phaneuf, G.S. Oehrlein, B.K. Long, C.G. Willson, *Appl. Phys. Lett.* 91 (2007) 233113-1-3.
- [17] Y.-T. Su, T.-R. Shan, S.B. Sinnott, *Nucl. Instrum. Methods B* 267 (2009) 2525.
- [18] C. Ngaojampa, P. Nimmanpipug, L. Yu, S. Anuntalabhochai, V.S. Lee, *J. Mol. Graph.* 28 (2010) 533.
- [19] J. Yana, V.S. Lee, P. Nimmanpipug, S. Dokmaisrijan, S. Aukkaravittayapun, T. Vilaithong, *JMME* 1 (2007) 556.
- [20] J. Yana, P. Nimmanpipug, S. Chirachanchai, R. Gosalawit, S. Dokmaisrijan, S. Vannarat, T. Vilaithong, V.S. Lee, *Polymer* 51 (2010) 4632.
- [21] J.B. Spencer, J.O. Lundgren, *Acta Cryst.* B29 (1973) 1923.
- [22] Materials Studio, Accelrys Software Inc., San Diego, CA, 4.4 edn., 2007.
- [23] M.G. Martin, *Fluid Phase Equilib.* 248 (2006) 50.
- [24] H. Sun, *J. Phys. Chem. B* 102 (1998) 7338.
- [25] H.J.C. Berendsen, J.P.M. Postma, W.F. Van Gunsteren, A. DiNola, J.R. Haak, *J. Chem. Phys.* 81 (1984) 3684.
- [26] A. Kalaiselvan, P. Venuvanalingam, *763* (2006) 1-5.

CURRICULUM VITAE

Name: Mr. Yuttakarn Rattanachai

Education Background:

1994-1997 B.Sc. (Physics) Srinakharinwirot University, Bangkok, Thailand.

1998-2001 M.Sc. (Physics) Chulalongkorn University, Bangkok, Thailand.

Work Experience:

2002 Rajamangala University of Technology Suwanaphumi, Suphanburi,
Thailand.

2003 Huachiew Chalermprakiet University, Samut Prakarn, Thailand.